Enhanced Ultra-Thin Film Nanocrystalline Silicon Photovoltaic Device Architectures

by

Mohsen Mahmoudysepehr

A thesis
presented to the University of Waterloo
in fulfillment of the
thesis requirement for the degree of
Doctoral of Philosophy
in
Electrical and Computer Engineering (Nanotechnology)

Waterloo, Ontario, Canada, 2017

Examining Committee Membership

The following served on the Examining Committee for this thesis. The decision of the Examining Committee is by majority vote.

External Examiner	NAME: Nazir Kherani Title: Professor
Supervisor	NAME: Siva Sivoththaman Title: Professor
Internal Member	NAME: Dayan Ban Title: Professor
Internal Member	NAME: William Wong Title: Professor
Internal-external Member	NAME: Tong Leung Title: Professor

AUTHOR'S DECLARATION

I hereby declare that I am the sole author of this thesis. This is a true copy of the thesis, including any required final revisions, as accepted by my examiners.

I understand that my thesis may be made electronically available to the public.

ABSTRACT

Semi-transparent photovoltaics (STPV) is an important component in building integrated PV (BIPV), which is a rapidly growing PV sector. Thin film based transparent solar panels have the strongest potential for window and skylight applications, and the main challenge is to incorporate good transparency with acceptable conversion efficiency.

This PhD thesis presents the intended research on nanoplasmonic architecture for enhanced ultra-thin film solar cells for application in BIPV and mobile devices. The first chapter briefly explains the recent status of solar thin-film. The second chapter concisely introduces the role of nanoplasmonics in solar cells and discusses theoretical treatment to incorporate them in photovoltaic energy conversion. With this background information and by taking into account the application of these architectures for enhanced photovoltaic energy conversion, the main aspect of experimental works of this doctoral thesis are stated in chapter three. In this chapter development process for the fabrication of aluminium doped zinc oxide (AZO) as a transparent conductive oxide (TCO) layer with enhanced transparency and conductivity explained. The influence of chamber pressure, RF power, and deposition temperature has been systematically studied and the electrical parameters such as film resistivity, carrier concentration, carrier mobility as well as optical transmission have been analyzed. Film deposition at 250°C and a low chamber pressure of 0.5mT resulted in a very low resistivity of 2.94×10^{-4} ohm-cm.

In developing ultra-thin film solar cells, doped layers with high conductivity, highly efficient yet thin absorber layers, and high conductive transparent conductive oxides are key issues in developing large area, transparent devices. Ultra-thin nanocrystalline silicon (nc-Si), due to its higher electron mobility and acceptable levels of transparency and optical absorption, is a potential candidate for transparent PV devices. Additionally, incorporating nc-Si material as the absorber layer in single or tandem thin film PV cells greatly enhances the spectral efficiency and device stability.

In chapter four, a new transparent nc-Si solar cell with p-i-n configuration is developed on glass substrates incorporating highly conductive AZO films, developed in chapter 3, as top and bottom electrodes. The main experimental processes involved, (i) development of a high deposition rate process in a modified PECVD system, (ii) optimization of doped and undoped micro and

nanocrystalline Si layers at temperature 300°C, (iii) process development for AZO films by sputter deposition at low pressure and moderate power with enhanced conductivity and transparency, and (iv) process integration for single junction p-i-n device process on glass substrate. Additionally, highly conductive (17S/cm) n-type μc-Si:H (SiH_4, PH_3, 98% H_2 dilution) and p type μc-Si:H (SiH_4, B_2H_6 , 98.5% H_2 dilution) films have been developed at 300°C.

The optimum photovoltaic performance is achieved with an absorber layer right at the transition from amorphous to nanocrystalline silicon. Conversion efficiencies exceeding 5% have been obtained.

The novel contribution of this research: nanoplasmonic architectures for ultra-thin film solar cells, is presented further more in chapter five by investigating the key design criteria and analyzing device optical performance accordingly. In addition, re-establishment of certain design parameters for nanoplasmonics in ultra-thin film solar cells is further investigated. The main focus is to evaluate design criteria for enhanced absorption in a-Si thin and ultra-thin film through designing a proper nanoplasmonic metallic structure. For this approach, the shape effect (size and type), type of dielectric, and type of metal are optimized to achieve maximum optical absorption.

In chapter 6 different fabrication method for nanoplasmonic structures further elaborated and experimental work for random Ag nanoisland formation through NSTS method explained. Different process parameters such as thin film thickness, annealing temperature are investigated to reach to the optimized deposition condition based on chapter 5 simulation results. At the end, 2 nanoplasmonic device architectures (superstrate and substrate) developed by incorporating Ag nanoisland in front and back of fabricated ultra-thin film devices. Comparing the performance of the fabricated cells shows that in general using nanoplasmonic structure on the back of the device has better overall performance. In substrate configuration 9.8% enhancement in efficiency was observed. Strong light scattering of Ag nano-island and near-field enhancement of incoming light are the main driving force of the performance improvement in the nanoplasmonic thin film solar cells. However, for the superstrate device configuration the performance enhancement is offset by introducing metallic recombination sites and also increasing the metallic backward scattering. In conclusion, using nanoplasmonic architects has better effect when they are used in the back of the device to surpass the effect of reflection and parasitic absorption of final devices.

ACKNOWLEDGEMENT

This chapter came to an end, though the story remains …

… Hundred tomes will not divulge the love

Now that I am writing these lines as the last words of my PhD thesis I have a strange feeling of reaching to the end of my graduate journey. A journey filled with ups and downs, with very hard moments that I said to myself, man, am I going to make it? Thanks god for not leaving me alone and gave me the experience of finding and feeling love in this journey. With her accompany, I examined and felt the moment of changing impossible to possible and not giving up.

In my journey, first and foremost I offer my sincerest gratitude to my supervisor, Prof. Siva Sivoththaman, who has supported me throughout my thesis with his patience and knowledge. I attribute the achievement of my PhD degree to his encouragement and assistance. Without his advice, this thesis would not have been written or completed. One simply could not wish for a better or friendlier supervisor.

I would like to especially thank my committee members, Prof. Tong Leung, Prof. William Wong, and Prof. Dayan Ban for all their support and constructive opinions; it was a great honour for me to have such opportunity to have their guidance through my project.

Heartfelt thanks to my dear friends and lab mates Ehsan, Navid, Maziar, Lin, Bahareh, Bita, Roohen, Chris, Shadi, and Nasim, who blessed my everyday work brain storming and having a good time together as well.

I am deeply lucky to have friends who helped me maintain the courage to write and to move forward. I would like to thank all of them, near or far, for their support and encouragement.

I would like to thank especially my mother and father for all their love and support they gave me in my life, and also my sister and brother for their love and support.

Finally, I would like to thank my gorgeous wife, Saina, for all her unforgettable support and encouragement during my PhD Journey.

DEDICATION

To my one and only … my end and beginning … my all … Saina

&

To my Mom and Dad … Ghodsi and Mohammad

&

To my siblings … Mehdi & Malihe

Table of Contents

List of Figures

List of Tables

Chapter 1

Thin Film Solar Cells: Status and Challenges

Photovoltaic, simply the direct conversion of sunlight to electricity, represent the most plentiful renewable energy for future global needs and is now the fastest growing technology for electricity generation. In this chapter, thin film solar cells and its importance is briefly introduced.

1-1. Introduction

Energy and its efficient management is one of the most significant strategic issues facing humanity in the third millennium. Fossil fuels, such as oil, coal, and gas, are the primary sources of energy in the world today. They support a wide range of machines, everything from automobiles to power plants that generate electricity for our homes, schools and businesses.

The limited resource of fossil fuels, along with global population growth, economic development, and resource availability taken in the context of climate change underscore the urgency of developing a new clean, reliable source of energy. Additionally, in the wake of BP's oil spill within the Gulf of Mexico and Fokoshima nuclear disaster in 2014, the environmental impact of fossil fuels and nuclear fuel has become increasingly more important. Reliable new technologies must thus be investigated for future energy sources, in order to satisfy the growing global demand, and overcome the current environmental issues of fossil fuels.

Up to now, different alternative energy sources, such as wind, nuclear power, biomass, hydro, and solar energy have been proposed by energy resource experts. To retain viability, these recommendations must meet minimum criteria for both environmental and economic

sustainability and full accessibility at any time or place. Unfortunately, not all of these alternative sources are suitable for the future. As an example, wind energy is not producible everywhere and requires specific environmental conditions. Nuclear energy is environmentally harmful due to its generation of of excess radioactive waste. Solar radiation, however, bears no obstacle in either respect, nor in any other of significance. Conversely, among recommendations, it is the most unique alternative; the cleanest source of energy available to mankind.

Sunlight offers, by far, the most abundant source of renewable and carbon-neutral energy. One day of sunshine could supply the entire world's energy for 4 to 5 years. Maintenance requirements are low, and it provides cost-effective, non-polluting, sustainable, and silent power supplies. In fact, the impact of global demand for energy, predicted by scientists, shows that by the 22nd century almost 75% of the world's energy will be supplied by the sun. This is not surprising given solar energy's integral, serviceability in scientific advancement, such as those pertaining to nanostructural technology. Its viability enables innovation through efficient energy conversion mechanisms, making it a distinctive and reliable energy source for the future.

Photovoltaics, defined as the direct conversion of sunlight to electricity, is now the fastest growing technology for electricity generation. It is based on a device known as a solar cell, which uses the photovoltaic effect, the production of electrons inside conducting materials by means of solar radiation, to produce electricity [1].

The photoelectric effect is the basic physical process by which a PV cell converts sunlight into electricity. It describes the emergence of an electric voltage between two electrodes attached to a solid or liquid system upon shining light onto this system. When light shines on a PV cell, it may be reflected, absorbed, or passed right through, but only the absorbed light generates electricity. The absorbed light transfer its energy to electrons enables them to gain excess energy to change their energy level and jump from their normal energy position to the electrical conductive energy bands and contribute in the generation of current. A "built-in electric field", generated as a result of charge transfer at the junction of 2 different semiconductor, provides the required mechanism for charge collection by providing voltage driving force [1].

1-2. Thin Film Solar Cells: definition and importance

Based on the definition given by Chopra et al. thin film is a thin material created ab initio by an atom/molecule/ion/cluster of species-by-atom/molecules/ions/clusters of species condensation process [3]. Depending on how the atoms/molecules/ions/clusters of the species are created for the condensation process, the methods for depositing thin films are termed physical vapour deposition (PVD), chemical vapour deposition (CVD), electrochemical deposition (ECD), or a mixture of PVD and CVD (hybrid).

Normally, a thin film solar cell, or a thin film photovoltaic cell, is a cell that is produced by depositing one or more thin layers (films) of photovoltaic materials on a substrate. The thicknesses of those layers vary from a few nanometers to tens of micrometer.

The following features of thin-film processes have been shown to be of interest for solar cell technologies [4]:

1. Availability of different physical, chemical, electrochemical, plasma based and hybrid techniques for thin-film deposition of the same material.

2. The microstructure of the films for most materials can be varied from one extreme of amorphous/nanocrystalline to highly oriented and/or epitaxial growth, depending on the technique, deposition parameters and substrate.

3. A wide selection of substrates, shapes, sizes, and areas are available.

4. Doping with different materials (compatible and even incompatible) is possible due to the relaxed solubility condition.

5. Passivation of surface and grain boundaries with different appropriate materials.

6. Different multi-junction architects with hybrid structure capability are feasible.

7. Bandgap engineering by creating graded bandgap, composition, and lattice constants, etc.

8. In the case of multicomponent materials, composition, and accordingly bandgap and other optoelectronic properties, can be graded in the desired manner.

9. Creation of different interlayer diffusion barrier and surface electric field by surfaces and interfaces modification.

10. Surfaces modification to control optical reflectance/transmission characteristics, haze and optical trapping effects.

11. Manufacturability for unit process integration from solr cell fabrication to module assembly line.

12. Thin-film manufacturing processes are generally eco-friendly.

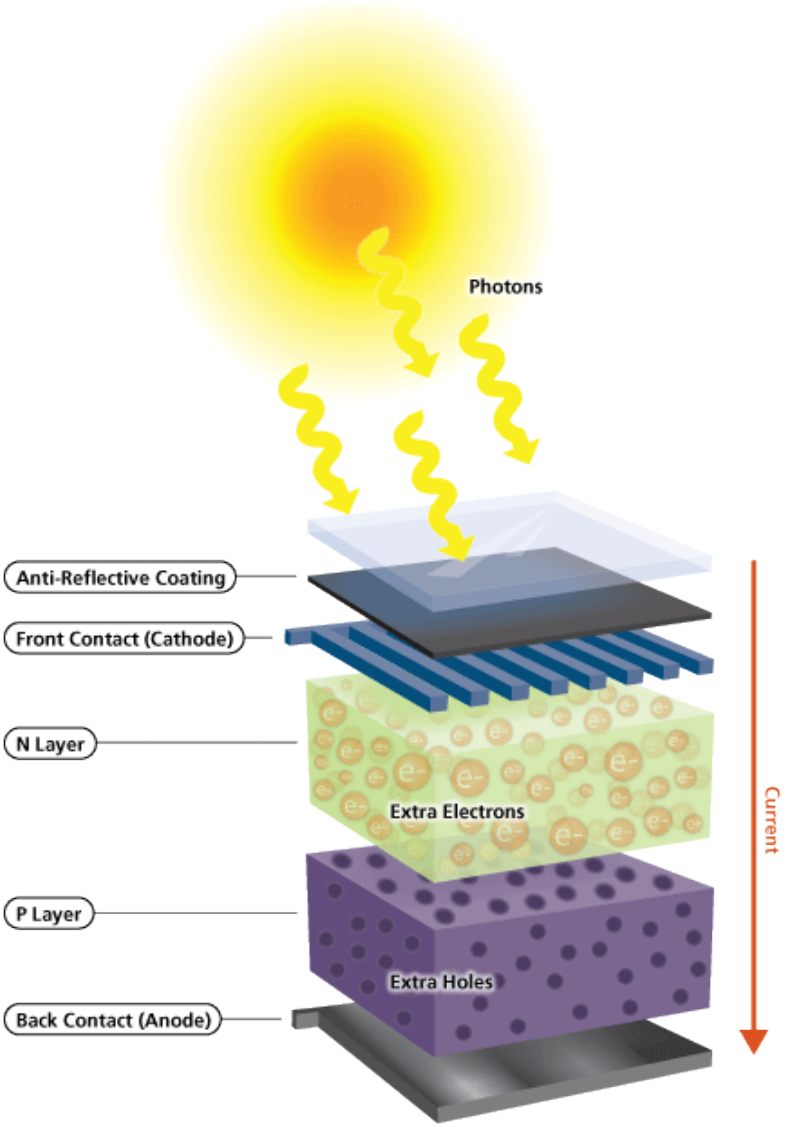

Figure 1-1. Schematic structure of a solar cell [2].

1-1-1. Building Integrated Photovoltaic (BIPV) and the Role of Thin Film Solar Cell

Building integrated photovoltaics (BIPV) are photovoltaic products and materials that function as part of building envelopes, replacing conventional construction materials such as roofs, skylights, canopies, facades, glazing and shades [5]. As functional components of building envelopes, BIPV have dual requirements, considerations, and challenges associated with being products that straddle both the construction and solar industries. BIPV is one of the fastest growing segments of the photovoltaic industry. Among current technologies, ultra-thin film solar cells have promising potentials as a transparent cell to be replaced conventional glass or placed over the glass. Monolithically manufacturing allows large area fabrication and continuous processing. By considering large installation area, good power generation, lighting and temperature control are potential achievements in BIVP [6][11].

Since the early 1980's thin film PV technology has shown steady advancement in manufacturing technology, generating new materials and lowering cost production. The necessity to produce cost-effective electricity continues to drive major corporations and investors towards the thin film PV industry.

The industry witnessed more than 100 companies entering the market between 2001 and 2009 [6]. Thin Film PV technology has progressed significantly from a little strip of PV cells powering calculators to the sophisticated building integrated photovoltaics (BIPV) applied in solar chargers for mobile devices.

According to estimates by McKinsey & Co on behalf of Natural Resources Canada, the global solar PV market will be valued at $325 billion worldwide by 2020 and $962 billon by 2030 [11]. As of 2014 , Canada is estimated to constitute only 2% of the global market, with China (27%), Japan (24%), and the US (16%) constituting the majority of the market [8].

The installed capacity of PV systems in Canada reached more than 1.9 GW, out of 511 TWh consumed overall as of 2014, representing 0.4% penetration of the electrical consumption of the country [8]. The majority of PV installations are concentrated in Ontario, driven by Ontario's FIT Program. As of 2013, solar PV represented 1% of Ontario's electricity

generation [9]. An identified driver of the solar PV market is the decreasing cost of module pricing that has dropped to $0.85 CA in 2014 from $5.53 CA in 2004. The cost of solar PV power is estimated to reach grid parity in most places in Canada by 2022 [10]. BIPV remains a small part of the overall solar PV market. An estimate of the global market size for BIPV is $3 billion in 2015, but is believed to be growing, to over $9 billion in 2019 [11][12].

BIPV products can be classified in five main categories [13]:

- Standard in-roof/full roof systems
- Semitransparent systems (glass/glass modules)
- Cladding systems
- Solar tiles and shingles
- Flexible laminates

BIPV applications can be broadly classified into [14]:

- Pitched roofs
- Flat and curved roofs
- Facades (cold and hot)
- Skylights
- Curtain walls
- Shading systems

As described in Figure 1-2, thin film module production shows more than 2000% growth from 2001 to 2009. Beginning with mere 14 MW production in 2001, the market expanded to 2141 MW in 2009, at a compound annual growth rate (CAGR) of 58%. Market analysis reveals promising outlook for the coming decade appears promising as the major thin film producing countries, Japan, China, and the US, announce aggressive support for renewable energy expansion through incentives and regulations. Finally, it is predicted that thin film module production is projected to grow at a rate of 24% from 2009 to reach 22,214 MW production by 2020 [6].

Over time, thin film technology has also been successful in gaining a growing share of the PV market as illustrated in Figure 1-3. Thin film production market share in the global solar PV market grew from a mere 2.8% in 2001 to 25% in 2009, indicating a growing share for the imminent future. Thin film solar PV, as per estimation, is set to increase its share to ~38% by 2020. Expectations are that thin film solar PV technology, in the long-term will surpass

dominating conventional solar PV technology, thus enabling the long sought-after grid parity objective [6].

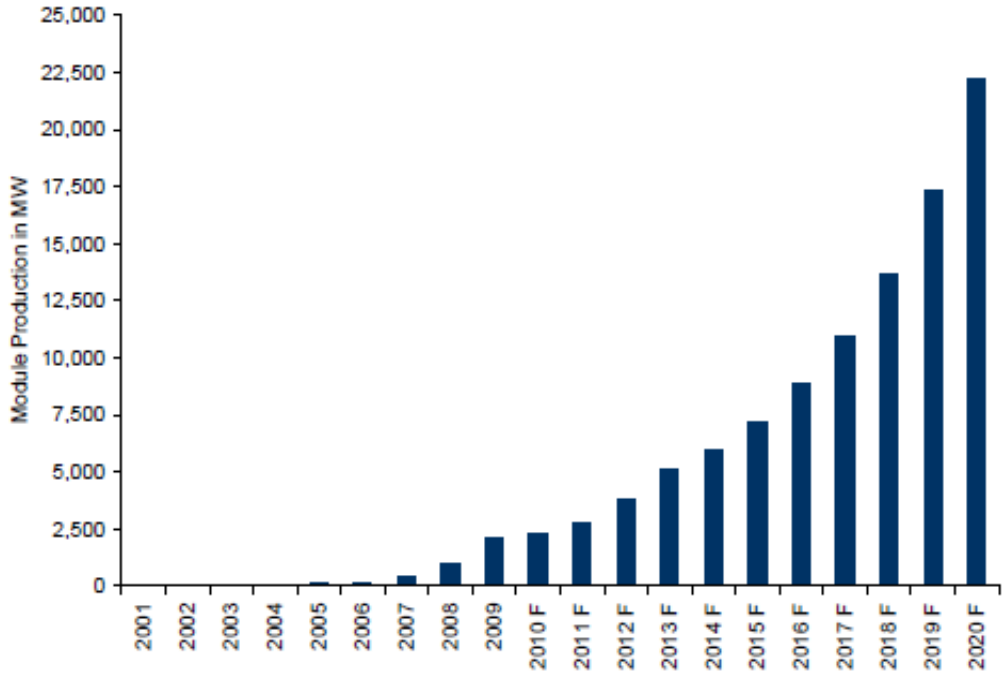

Figure 1-2. Global Thin Film Module Production in MW, 2001-2020 [6].

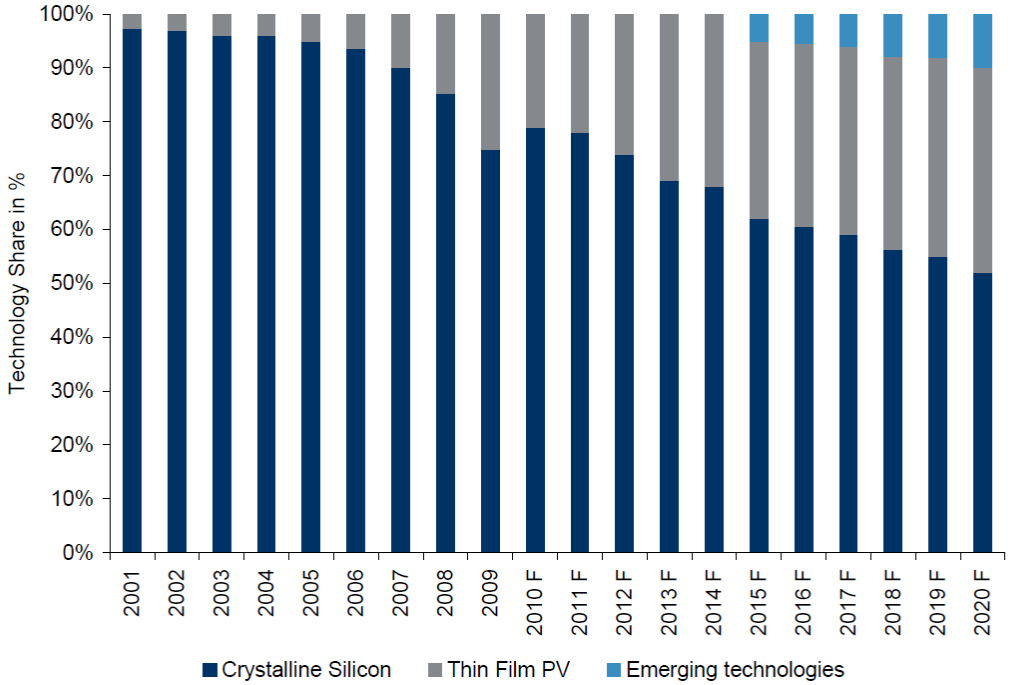

Figure 1-3. Thin Film Market Share in % (in terms of module production), 2001-2020 [6].

1-1-2. Thin Film Solar Cell Devices

Different approaches can be utilized to categorize thin film solar cell devices. One way is to classify them based on their junction technology, as follows:

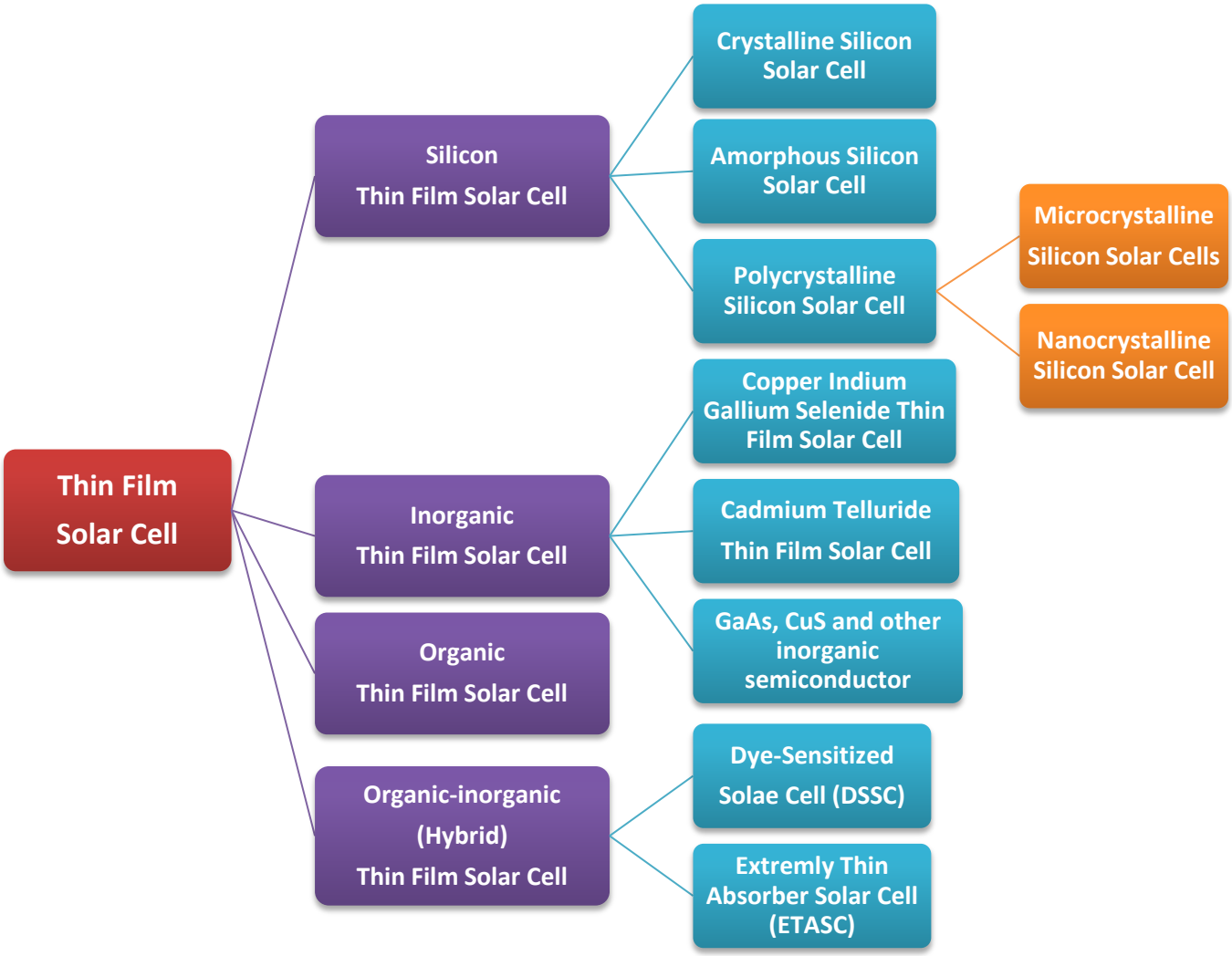

In Table 1-1 discusses general advantages and disadvantages of different silicon and inorganic thin film solar cells in details.

Table 1-1. Comparison of different silicon and inorganic thin film technologies

Technology	Pros	Cons
aSi:H	• Cost-effective material compared to crystalline silicon • No limitation in resource, since silicon is the most common material on earth • Bandgap engineering through changing deposition conditions facilitates capturing a wider spectrum of sunlight • Enhanced output at low light level • Adaptable on different type of substrate, from flexible to rigid • Both superstrate and substrate deposition configuration are possible • Verifiably reliable for use, due to its thoroughly developed TFT manufacturing process. • Very good R&D support	• Low efficiency compared to other thin films. • Efficiency degradation overtime • Need multi-junction structures for higher efficiency (above 15%). • Flexible substrate have a shorter lifetime • Multi-junction structure manufacturing is expensive due to complexity of process.
CIGS	• Highest efficiency at sunlight conversion among thin film technologies • CIGS compound is robust and defect tolerant • No degradation overtime • Both rigid and flexible substrate possible • Well-known manufacturing process developed and proven in other industries • Potential to have the lowest cost manufacturing for roll-to-roll capability • Potential to offer the lowest $/Watt	• Supply problem due to the use of Indium, a rare-earth element • Trace amount of rare and toxic material is used. • Superstrate configuration is not possible • Not durable on flexible substrate • Large-scale manufacturing has not been advanced. • Complex manufacturing process due to the deposition of many thin film layers.
CdTe	• Considering bandgap, is one of the best semiconductors for PV application • Low Cd usage • Manufacturing infrastructure available for large scale production. • Can be produced in high volume. • Bears the lowest cost in the large-scale manufacturing process ($1.4/Watt)	• Use of health risk element, Cd • Use of telluride (Te), a rare-earth material that could cause a supply issue • High safety practices required for manufacturing facilities • Recycling of modules • Only glass can be used for deposition • Not usable on flexible substrate • Waste deposal of manufacturing well developed. • Only adapted for the batch process, as opposed to the roll-to-roll process.

1-3. Thin Film Photovoltaics and Advanced Photon Management

A typical approach for improving efficiency in thin-film photovoltaics is to incorporate an externally structured material on top or bottom of active device layer. This will decouple the performance enhancement strategy and its possible effect on highly optimized cell structure. There have been different approaches developed which uses advance photonic management mechanism. In the following these mechanisms are explained in the order of their complexity:

1) **Anti-Reflection Coatings (ARCs).** By decreasing the light reflection at the top layer of thin-film cells through using multilayers or nanostructured coating layers, light absorption can be improved at the whole spectrum, or specific wavelength at even different incident angle beyond nominal condition [15] [16].

2) **Light trapping through internal reflection for light path length increase.** By incorporating advance surface treatment through texturing or incorporating nanoplasmonics architects the incident light can be propagated at a wider angle inside of the active region of thin film which generate more internal reflection on the interfaces and increasing the path lengths of light through the absorber and, accordingly, the probability of absorption [15][16].

3) **Optical Field Enhancement.** Using nanoplasmonic architecture such as metallic nanoparticles assembly to activate localized surface plasmons (LSPs) to increase the optical field intensity in the vicinity of nanoplasmonic structure. Increasing light intensity leads to higher optical absorption [15][16].

4) **Down-Shifting.** As the name shows in this mechanism high-energy portion of light spectrum which has lower quantum efficiencies in thin-films down-converting their photon energy to the region of spectrum with maximum quantum efficiency [15][16].

5) **Down-Conversion.** In this mechanism energy hot-carriers, photons with very high energies, transformed from one high-energy photon into two photons with the energy level matching with the bandgap of active thin-film layer. In this mechanism the energy which is normally wasted as heat will contribute in carrier generation [15][16].

6) **Up-Conversion.** The solution to accommodate low energy part of solar spectrum in carrier generation is to convert the low energy photon with low absorption ratio to higher-energy photons which has higher absorption ratio through up-conversion [15][16].

The down-conversion and up-conversion demonstrate the best solution to overcome to the Shockley–Queisse (SQ) limit by utilizing part of solar spectrum in carrier generation which is normally due to the limit single junction characteristic is not possible.

1-4. Light Trapping and Limitation of Thin Film Solar Cells

Two critical parameters in designing thin-film solar cells are optical absorption thickness and carrier collection length. By calculating the absorption spectrum of crystalline silicon at different thickness and comparing it with the standard AM1.5 solar spectrum (Figure 1-4), it is revealed that the photovoltaic absorber must be 'optically thick' to enable full absorption of generated photons. As shown in Figure 1-4 , most part of the solar spectrum, mainly above the visible spectrum and in the IR region, is poorly absorbed. As a result, conventional wafer-based crystalline silicon solar cells have a general thickness of 180-300μm. However, the collection of all generated photocarriers requires minority carrier diffusion lengths to be several times larger than the material thickness; for if the light is not absorbed within a diffusion length of the junction; the light-generated carriers are lost to recombination. This condition is most easily met for thin cells.

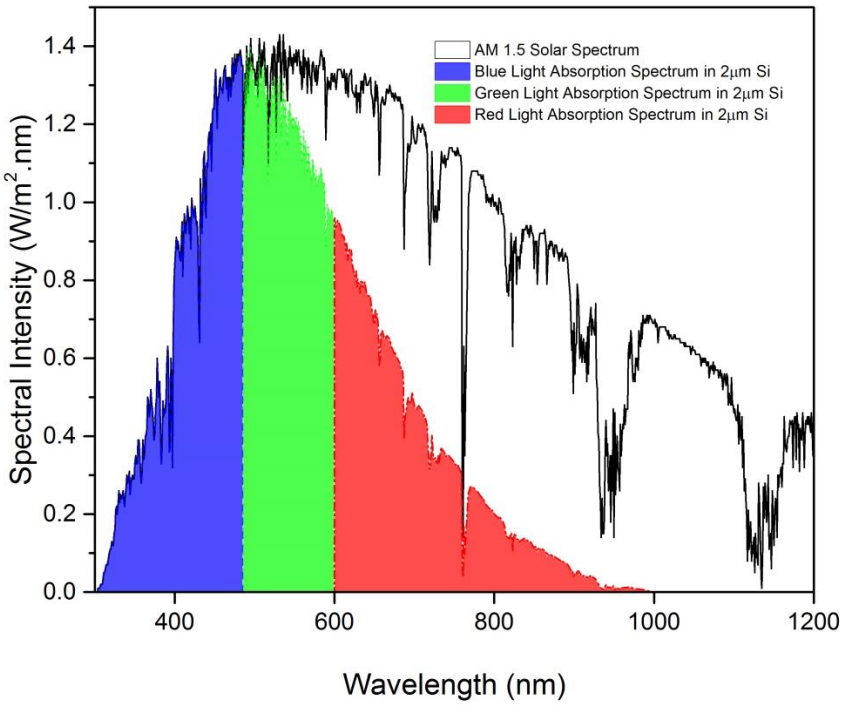

Figure 1-4. AM1.5 solar spectrum with a simulated graph that shows the solar energy absorbed in a 2μm thick crystalline Si film (assuming single-pass absorption and no reflection).

One limitation factor for thin-film solar cells with indirect-bandgap semiconductor is the low absorption ratio for near-bandgap spectrum. This limited light trapping, which allows light to

bounce around inside the absorber, is an essential objective in designing the thin-film solar cell structure (Figure 1-5).

In conventional wafer based Si solar cells, the standard light trapping method is to apply front or back surface texturing by creating a pyramidal surface texture enabling forwrad scattering of light into the solar cell at multiple angles, thereby increasing the effective path length in the cell (Figure 1-5 (a)). Yablonovitch established that path length enhancement by random surface texturing has the $4n^2$ limitation factor in the Lambertian limit, where n is the index of refraction for absorption. However, due to the size of absorber layer in thin films which is in the range of 100-500nm, using micrometer-sized texturing are not applicable in thin-film cells since the surface roughness would exceed the film thickness and the greater surface area increases minority carrier recombination in the surface and junction regions [17]. One way to increase the optical absorption in thin film devices is to reduce the reflectivity of incoming light by applying an Anti-Reflection Coating (ARC) on the top layer. However, ARC could not improve optical path length inside the absorber layer and especially for ultra-thin film structures does not effectively improve the photon absorption [18].

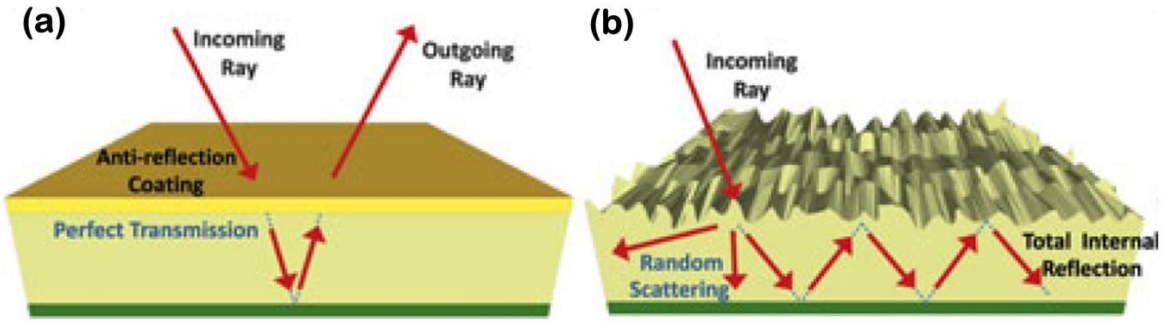

Figure 1-5. Schematic pictures shows increased light absorption of a material slab due to (a) An anti-reflection coating (ARC), and (b) Geometric scattering which uses random scattering of a Lambertian surface to increase the light path length inside the absorber layer. This Figure is reproduced with permission –See Letters of Copyright Permission (Courtesy of MRS Bulletin) [18].

To improve the light absorption in thin-film solar cells one effective way is to utilize light harvesting techniques based on photon management approach relies on wave optics. These techniques works in instances where light must be treated as a wave phenomenon and can be made to interfere, in order to reinforce the electric field in certain regions.

Different approaches to apply coherent light trapping inside of thin film can be divided into 2 different categories:

1- Photonic Crystals (PC): Applying a periodic dielectric medium, called Photonic Crystals, as a back-reflector or inside of absorbing media could improve optical absorption. Figure 1-6 provides a brief description of enhancement mechanism by which PC assists in light trapping.

2- Nanoplasmonic (Metal Nanostructures): Metallic nanostructures exhibit spectacular properties when interacting with light, which cause them to attract a lot of attention as a means to trap light in photovoltaic devices. In this regard, nanoplasmonics, which deals with the behavior of metallic structures at nanoscale, shows promising approaches to overcome the optical absorption problem in thin and ultra-thin film PV cells.

In the next chapter, the importance and mechanisms for nanoplasmonics in photovoltaics will be discussed.

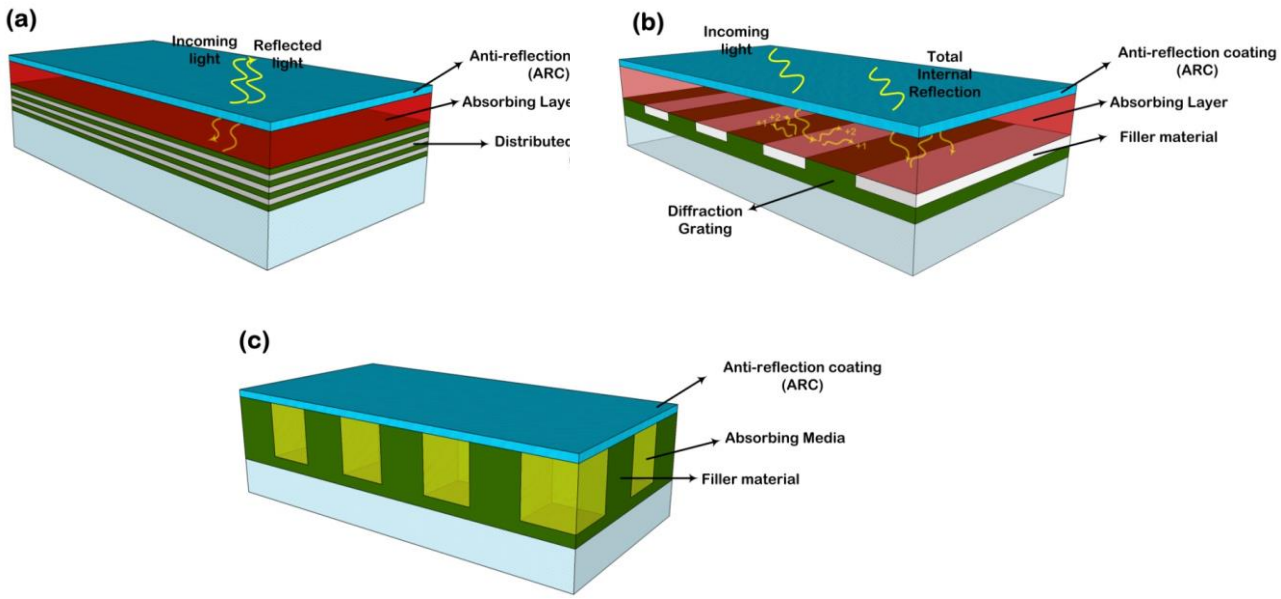

Figure 1-6.Three main wave-optic based light-trapping mechanisms. (a) A Photonic Crystal (PC) Distributed Bragg Reflector (DBR) used as a high-quality omnidirectional back reflector with very low to no losses. (b) Using PC attached to the back side of active layer of device to act as as a diffractive/scattering element that scatters incident light into quasi-guided modes supported by absorber layer that can be thin or thick. (c) Patterning the absorbing region into a PC to couple incident light into quasi-guided modes. This Figure is reproduced with permission –See Letters of Copyright Permission (Courtesy of MRS Bulletin) [18].

Chapter

2

Theoretical Treatment for Nanoplasmonics in Photovoltaics: State of the Art

Nanoplasmonic architectures are witnessing a dramatic growth of interest and utilization in photovoltaic energy conversion. In this chapter, a brief introduction on nanoplasmonics and its application in photovoltaics will be presented.

2-1. Introduction: a brief history

Nanoplasmonics, a rapidly evolving subfield of nanophotonics, deals with optical phenomena on the nanoscale in nanostructured metal systems. Specifically, this system requires the optical energy be kept concentrated on the nanoscale, on account of modes called surface plasmons (SPs).

In general, materials are polarized by electromagnetic waves through the displacement of bond charges (both ions and electrons), electronic transitions between occupied and unoccupied electronic states, and free electron displacement (if free electron exists). Surface plasmons are longitudinal charge-density fluctuation or simply electromagnetic oscillations of free electrons at the interface between a metal and a dielectric where the real part of the dielectric function changes sign across the interface. They resemble photons, but are nonradiative in nature and normally exhibit a much shorter wavelength than photons in free space. They demonstrate strong spatial field confinement and enhancement, and prove extremely sensitive to the geometry of the supporting structure, thus allowing an extensive engineering of both their spectral properties and their associate electromagnetic field distribution by appropriate structural design [19].

Surface plasmons essentially exist in two forms—Localized Surface Plasmons (LSPs) and Propagating Surface Plasmon Polaritons (SPPs).

2-1-1. Surface Plasmon Polaritons (SPPs)

When light incidents on a metal surface at a right incident angle and energy, the energy of photons will be converted and stored through density fluctuations in conduction electrons; known as surface plasmons (SPs). In SPPS, surface plasmons propagate as a longitudinal charge-compression electromagnetic wave at the interface of a metal and dielectric. Figure 2-1 shows the layered structure, the simplest geometry for which SPPs exist. As portrayed the field penetrates more significantly into the dielectric half-space than the metal, although both may be deemed subwavelength in distance [20].

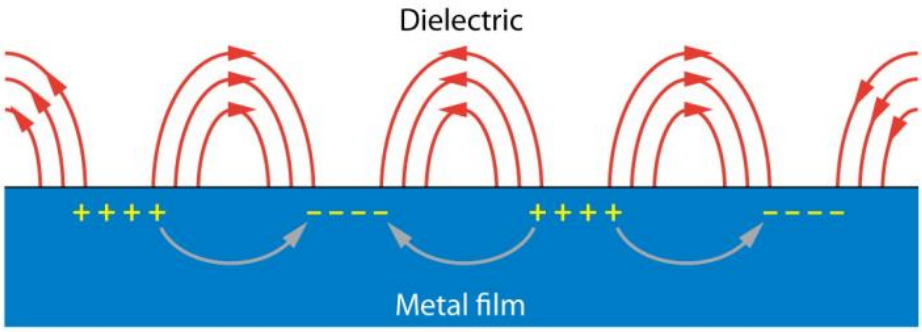

Figure 2-1. Illustration of propagating surface plasmon Polaritons (SPPs) at metal-dielectric interface where, an incident field excites a charge-compression wave that propagate along the interface.

By solving Maxwell's equations for this geometry, it is shown that this geometry supports transverse magnetic (TM) electromagnetic (EM) solution for the following equations [20]:

In the dielectric:

$$\begin{cases} H_d(x,t) = (0,A,0)e^{k_z^d z}e^{i(k_x x-\omega t)} \\ E_d(x,t) = -A\dfrac{c}{i\omega\varepsilon_d}(k_z^d,0,ikx)e^{k_z^d z}e^{i(k_x x-\omega t)} \end{cases} \qquad (2-1)$$

in the metal:

$$\begin{cases} H_m(x,t) = (0,A,0)e^{k_z^m z}e^{i(k_x x-\omega t)} \\ E_m(x,t) = -A\dfrac{c}{i\omega\varepsilon_m}(k_z^m,0,ikx)e^{k_z^m z}e^{i(k_x xx-\omega t)} \end{cases} \qquad (2-2)$$

in which:

$$k_z^d = \sqrt{{k_x}^2 - \varepsilon_d(\frac{\omega}{c})^2} \quad \text{and} \quad k_z^m = \sqrt{{k_x}^2 - \varepsilon_m(\frac{\omega}{c})^2}$$

$$k_x = k_{SPP} = \frac{2\pi}{\lambda_0}\sqrt{\frac{\varepsilon_m(\omega)\varepsilon_d}{\varepsilon_m(\omega)+\varepsilon_d}} \qquad (2-3)$$

where $\lambda_0 = \frac{2\pi c}{\omega}$, is the wavelength of photons in vacuum, ε is the electron permittivity, k is the wave vector, H and E are magnetic and electric fields, respectively, and A is constant.

The mode wavelength (λ_{SPP}) and propagation length (L_{SPP}) are then determined as:

$$\lambda_{SPP} = \frac{2\pi}{Re(k_{SPP})} \qquad (2-4)$$

and

$$L_{SPP} = \frac{2\pi}{2Im(k_{SPP})} \qquad (2-5)$$

In addition, because the surface plasmon is generated and confined at the interface as a two-dimensional wave, the SPP wave amplitude decays exponentially in both the metal and the dielectric. By assuming, Re(ε_m)>>Im(ε_m), the decay rates in metal (δ_m) and dielectric (δ_m) as

$$\delta_m = k_0\left|\frac{Re(\varepsilon_m)}{\varepsilon_d + Re(\varepsilon_m)}\right|^{1/2} \qquad (2-6)$$

and

$$\delta_d = k_0 \left| \frac{{\varepsilon_d}^2}{\varepsilon_d + Re(\varepsilon_m)} \right|^{1/2} \qquad (2-7)$$

The maximum surface plasmon frequency (ω_{SP}) is cacculated by

$$\omega_{SP} = \frac{\omega_P}{\sqrt{1+\varepsilon_d}} \qquad (2-8)$$

where, $\omega_{SP}$is the plasmon frequency in bulk material.

2-1-2. Localized Surface Plasmons (LSPs)

Like those supported by metal nanoparticles, the interaction between the electric field of incident light and the free electrons of a metal sphere (whose size is smaller than the wavelength of light) spurs oscillation of the free electron in the nanoparticles, and resulting in positive and negative charge polarization [20].

For sub-wavelength metal nanoparticles, the incident electromagnetic field can be considered homogeneous over the entire nanoparticles, known as quasi-static approximation. In this case, a uniform distribution of statistic electric field from the incident light can be experienced by conduction electrons in metal nanoparticles. Therefore, instead of travelling and propagating at the metal/dielectric interface, electromagnetic field causes a displacement between free electrons and nuclei. Two circumstances work to obstruct this displacement: (1) the action of the inter-electron Coulomb forces which tend to smooth charge density and (2) the Pauli exclusion principle leading to an effective repulsion between free electrons. A restoring force arises from the coulomb attraction between the displaced electrons and the positively charged nuclei causing the free electrons to oscillate at the dipolar plasmon resonance. A resonance condition through a constructive interface will be generated as a consequential similarity between the frequency of the dipole plasmon and the incident light, creating the strongest signal for the plasmon [20]. Figure 2-2 illustrates a small metal nanoparticles incident with a flux of electromagnetic radiation.

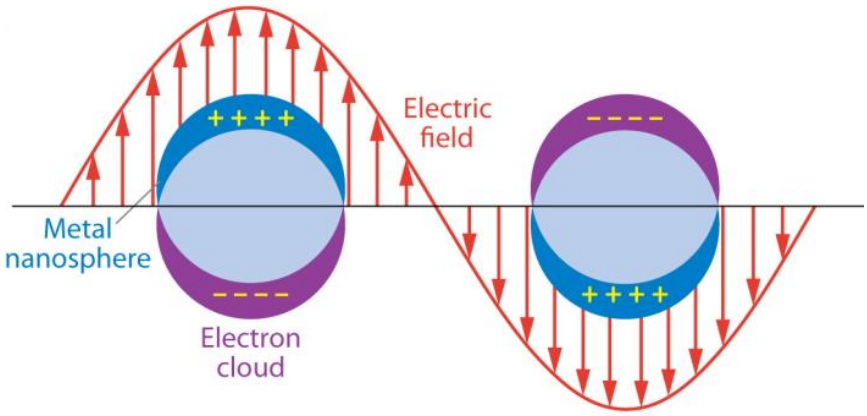

Figure 2-2. Illustration of Localized Surface Plasmons (LSPs) in a metallic nanosphere, where an incident electromagnetic field causes a disturbance of the free electrons in the particle (negative charges), leaving behind a positively charge portion of the particle. Oscillation happens at the dipole plasmon resonance frequency.

2-2. Nanoplasmonics for Photovoltaics

The incorporation of nanoplasmonic architectures in solar cells offers the possibility of reducing the absorber layer thickness through effective light trapping due to strong light interaction in plasmonic nanostructures and surrounding media [21].

Nanoplasmonics in photovoltaics was used unintentionally in 1990, when Hiramoto and his colleagues [23] decided to investigate the effect of inserting a thin (<3nm) gold interstitial layer on the photovoltaic properties of Me-PTC/H2Pc tandem organic solar cell. They observed that the short circuit current (J_{SC}) of their cell gradually increased; with heightened thickness of the Au layer from 0 to 3nm; showing an approximate maximum of 2nm. They also observed that deposited thin Au film seemed to have an island structure. Unfortunately, at that time Hiramoto and his colleague could not have known the contribution of surface plasmon polaritons of Au nanoisland on the enhancement of J_{SC}; hence they attribute the enhancement to the prevention of electron-hole recombination by electron repulsion from the interface of 2 cells, owing to uniform Schottky barrier at the Au/Me-PTC junction [23]. In 1995, Stenzel discovered a significant enhancement in photovoltaic conversion efficiency in CuPc organic cell by applying exactly Hiramoto method, and incorporated this enhancement to resonant light absorption in the metallic nanoisland cluster and not to a general modification of the interface [24].

Ensuingly, quite a few pioneer works with nanoplasmonic solar cells have been carried out by different researchers [21]. A primary focus of these studies centre on improving the thin-film solar cells through the use of metal nanoparticles distributed on the surface. The following list summarizes some original research, based on each date of completion.

- 1990: M. Hiramoto and et. al., incorporating gold nanoisland as an interstitial layer into the Me-PTC/H2Pc organic solar cell [23].
- 1995: Stenzel and colleagues, photovoltaic conversion enhancement factor of 2.7 for CuPc thin film organic cell by incorporation of copper clusters [25].
- 1998: Stuart and Hall, photocurrent enhancement by 18x with 165 nm SOI photodetector, with a wavelength of 800 nm using silver nanoparticles for scattering and absorption of light [26][27].
- 2000: Westphalen, Kreibig, Rostaslk, and Luth: enhancement for silver clusters incorporated into ITO and zinc phthalocyanine solar cells [28].
- 2004: Rand, Peumans, and Forrest, enhanced efficiencies for ultra thin-film organic solar cells due to 5 nm diameter silver nanoparticles [29].
- 2005: Schaadt, Feng, and Yu, gold nanoparticles used for scattering and absorption of light on doped silicon possessing 80% enhancements with 500 nm wavelength [30].
- 2006: Derkacs, Lim, Matheu, and Yu, gold nanoparticles on thin-film silicon gaining 8% on conversion efficiency [31].
- 2007: Pillai, Catchpole, Trupke, and Green, silver particles on thin-film and wafer based solar cells obtaining up to 19% efficiency in c-Si solar cells [32].
- 2008: Lindquist, Luhman, Oh, and Holmes, absorption enhancement in OPV by a factor of 3.2, through a plasmonic silver nanocavity array [33].
- 2008: Nakayama, Tanabe, and Atwater, absorption enhancement by scattering incident light, utilizing GaAs solar cells with size-controlled Ag nanoparticles at a wavelength below surface plasmon resonance [34].
- 2009: Ferry, Verschuuren, Li, Ruud, Schropp, Atwater, and Polman, creating a silver nanohole array back reflector for aSi:H solar cells, in order to achieve 4.2%-6.5% cell efficiency improvement with a 26% increase in short circuit current density through SPP coupling [35].

2-2-1. State of the art

Nanoplasmonic structures contribute to enhanced absorption in solar cells via three distinct mechanisms:

i) Light scattering and coupling using metallic nanoparticles as sub-wavelength scattering objects placed at the absorber surface. The purpose is to couple and trap freely propagating plane waves from incident sunlight into a distribution of angles through light-folding, and, in so doing, increase the optical path length within the absorber layer (Figure 2-3(b)) [21].

ii) Light concentration using localized surface plasmon resonance (LSPR) to increase efficacy in the absorption cross-section (Figure 2-3(a)) [21].

iii) Light trapping using surface plasmon polaritons (SPPs) through metallic nanostructured film on the back side of thin-film solar cells, enabling incident light coupling into SPP modes supported at a metal/semiconductor interface, as well as with guided modes in the semiconductor by which the light is converted to photocarriers (Figure 2-3(c)) [21].

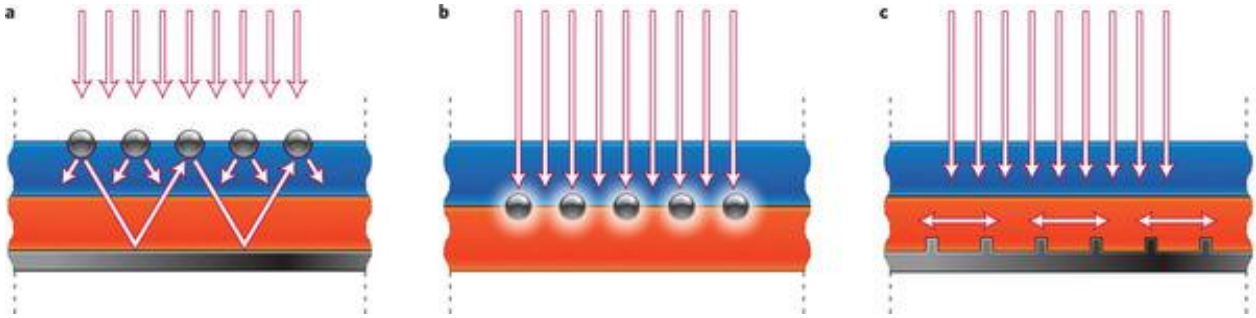

Figure 2-3. (a) Light trapping and concentration mechnaisms by the excitation of localised surface plasmons resonance around metallic nanoparticles embedded in the semiconductor of PV device. (b) Light scattering by the metal nanoparticles at the surface of the PV device. (c) Light trapping using SPPs on the back surface of PV device. This Figure is reproduced with permission –See Letters of Copyright Permission (Courtesy of Nature Materials) [21].

In the following the key feature of each mechanism following a brief review of research works will be presented.

2-2-2. Light scattering and coupling using Localized Surface Plasmons (LSPs) in nanoplasmonic particles

A conventional use for nanoplasmonic photovoltaics is to deposit metal nanoparticles on the top surface of thin film solar cells. The interaction of incident light with free electrons in

metallic nanoparticle excites LSPs and theses LSPs will increase the absorption in solar cell by three different mechanisms [36][37][38][39]:

1) *Light scattering due to an electromagnetic field interaction with LSPs, which causes the light to scatter in many different directions.* This allows light to travel along the solar cells and bounce between the substrate and the nanoparticles enabling the solar cells to absorb more light (Figure 2-4).

2) *High near-field intensities (NFI) associated with the LSP resonance of a particle.* Depending on the shape and size of a metallic particle, the frequency of optical excitation will result in strongly enhanced fields near the particle. Nonetheless, since the optical absorption is corresponding to the field intensities, high local fields will lead to increased absorption in solar cells.

3) *Excitation of propagating waveguide modes within the absorbing layer of solar cells.* The propagating waveguide modes may be either photonic waveguide modes or SPPs modes, in which the scattering centre is used to overcome the momentum mismatch between the incident wave vector and that of the waveguide mode.

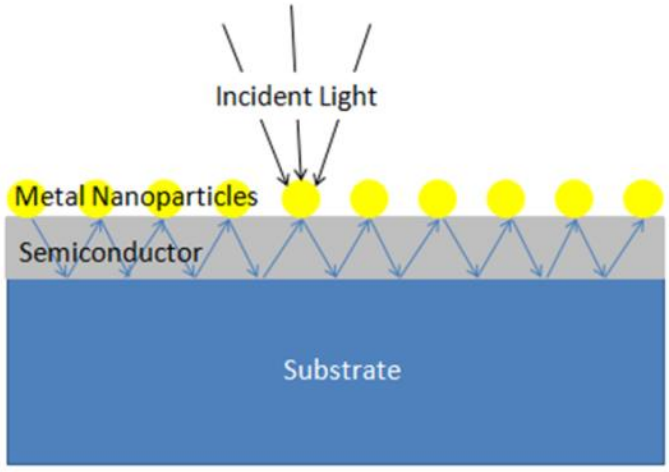

Figure 2-4.Schematic of light trapping at the surface of the solar cell. The incoming light is trapped into the absorption layer as a consequntial of a forward scattering at a multiple high angle, increasing the effective optical path length of the ligh in the absorbing layer and leading to higher light absorption [40].

2-2-3. Scattering and absorption in metallic nanoparticles

The basic principles for the functioning of plasmonic solar cells include scattering and absorption of light from the deposition of metal nanoparticles. Metal nanoparticles are strong scatterer of light at wavelength near the plasmon resonance. Enormous amount of theoretical

works have been done by scientists to describe localized surface plasmon phenomenon and its effect on absorption and scattering of incident light [21]. For particles with sub-wavelength dimension (the quasistatic limit) the best way to describe their light scattering and absorption is to consider them as a source of electromagnetic radiation. This approximation is known as the Rayleigh's approximation or Dipole approximation, in which the simplest radiator is an oscillating electric dipole with dipole momentum **p** [41].

In this assumption, the emitted electric and magnetic field from a sub-wavelength dipole in far-field zone (distance, $r = |\boldsymbol{r}| \gg \lambda$) described by:

$$E = \frac{k^2}{4\pi\varepsilon_0\varepsilon_m}[r \times (r \times p)]\frac{e^{i(kr-\omega t)}}{r^3} \qquad (2-9)$$

and

$$H = \frac{1}{Z_0}\frac{k^2}{4\pi\varepsilon_0\varepsilon_m}(r \times p)\frac{e^{i(kr-\omega t)}}{r^2} \qquad (2-10)$$

where $Z_0 = \sqrt{\frac{\mu_0}{\varepsilon_0}}$, is the vacuum impedance, ε_m is the dielectric constant of the surrounding medium, and ε is the dielectric constant of the particle.

The Rayleight approximation could be described by the following conditions:

$$x \ll 1 \ \ and \ \ |m|x \ll 1$$

where x is the size parameter and generally defines as the ratio of circumference to the wavelength. The relative index of reflection, m, is defined as:

$$m = \frac{n(\lambda)}{n_m(\lambda)} = \sqrt{\frac{\varepsilon(\lambda)}{\varepsilon_m(\lambda)}} \qquad (2-11)$$

As the dipole in the particle is induced by the incident electric field E_0, the dipole momentum **p** is connected with E_0 through

$$p = \varepsilon_0\varepsilon_m\alpha E_0 \qquad (2-12)$$

where α is the polarizability of the particle (or dipole).

The rate at which energy is absorbed and scattered by the particle, can be calculated using the above fields, and can be explained in terms of cross-sections for scattering and absorption:

$$\sigma_{sct} = \frac{k^4}{6\pi}\sum_{i=1}^{3}|\alpha_i|^2 , k = \frac{2\pi}{\lambda} \qquad (2-13)$$

$$\sigma_{abs} = k.Im\sum_{i=1}^{3}\alpha_i \qquad (2-14)$$

The outgoing radiation (scattering) is proportional to $\frac{{V_P}^2}{\lambda^4}$ (V_P is the particle volume), and the absorbed ingoing light is proportional to $\frac{V_P}{\lambda}$ [40]. This term dominates the extinction (absorption+scattering) of light for strongly absorbing particles. In addition to the interdependence of size, the shape of the nanoparticle and the dielectric properties of the nanoparticle and surrounding media are also affected by scattering and absorption. The imapct of these parameters is shown in the polarizability (α) generally defined as

$$\alpha_i = V_P\frac{\varepsilon-\varepsilon_m}{\varepsilon_m+G_i(\varepsilon-\varepsilon_m)} = V_P\frac{m^2-1}{1+G_i(m^2-1)} \qquad (2-15)$$

The G_i parameter takes the shape of the particle into account. For each shape there is a specific G_i, for example in sphere defined as $G_i = 1/3$. This G_i parameter satisfies the conditions:

$$\sum_i G_i = 1 \quad and\ G_i \le 1\ \forall i \qquad (2-16)$$

It is observable that for spherical particles when the polarizability of the particle becomes large:

$$\alpha_i\ maximize \xrightarrow{G_i\ sphere\frac{1}{3}} \frac{1}{3}\times(m^2-1)+1=0 \xrightarrow{m=\sqrt{\frac{\varepsilon}{\varepsilon_m}}} \frac{\varepsilon}{\varepsilon_m} = -2 \qquad (2-17)$$

This polarizability value is known as the surface plasmon resonance, at which by increasing α, the scattering cross-section can well exceed the geometrical cross section of the particle (Figure 2-5). For example at resonance a small silver nanoparticle in the air has a scattering cross-section that is approximately 10 times the cross-sectional area of the particle. In such a case, a substrate covered with 10% real density of particles could fully absorb and scatter the incident light.

Equations 2-13 and 2-14 indicate a larger particle size that is more appropriate for dominant scattering. However, the single dipole approach will fail for large particle sizes, because of disturbance in homogeneous distribution for all microscopic dipoles in the volume, as a result of introduction to a curvilinear surface. In this case, rigorous solutions for light scattering are needed; the most evolved being the Mie theory for spherical particles of arbitrary size. At the beginning of the 20th century, Gustav Mie established a semi-analytical theory, called the Mie theory, by solving Maxwell's equation for spherical nanoparticles to explain plane-wave scattering from the collective movement of free electrons in metal nanoparticles [42]. This theory has provided significant insight into normal modes for the oscillation of electromagnetic fields in spherical particles, and their effect on light absorption and scattering. It must be said, however, that neither general particle shapes nor the impact derived from arrays of interacting nanoparticles, can be adequately studied with Mie theory.

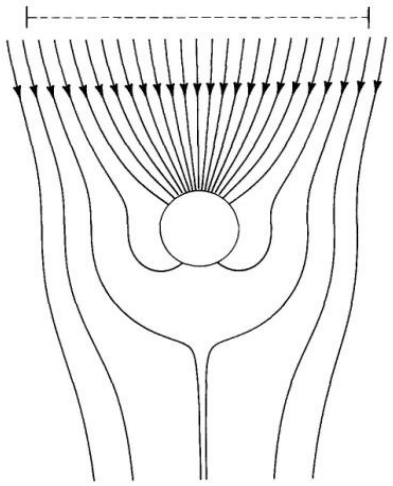

Figure 2-5. Schematic of scattering cross-section of arbitrary particles with electromagnetic wave.

Therefore, a variety of numerical methods have been developed to model arbitrary particle shapes, including FEM (Finite Element Method), FDTD (Finite difference Time Domain), and FDFD (Finite Difference Frequency Domain), along with discrete dipole, multiple pole methods, and the T-matrix method [20].

2-3. Light concentration with LSPRs

Another way to incorporate surface plasmon resonance in solar cell is to maximize the strong local field enhancement around the metal nanoparticles to increase absorption in a surrounding semiconductor material. In this instance, nanoparticles store the energy of incident sunlight in localized surface plasmon modes and act like an effective antenna, coupling the light with surrounding semiconductor media.

K. Tanabe [43] investigated the field enhancement factors, which are defined as the intensity ratio between the fields around the object and those in absence of the object or the original incident fields, for spherical metal nanoparticles and nanoshells in different environments. He used the classical electromagnetic field theory in the quasistatic limit, utilizing empirical wavelength dependent dielectric constants and a defined electric field at a distance of r around a metallic nanoparticle with radius, a, as follows:

$$E = E_0\left[\left(1 + 2\frac{a^3}{r^3}\frac{m^2-1}{m^2+2}\right)\hat{e}_r cos\theta + \left(-1 + \frac{a^3}{r^3}\frac{m^2-1}{m^2+2}\right)\hat{e}_\theta cos\theta\right] \qquad (2-18)$$

where $m = \sqrt{\frac{\varepsilon}{\varepsilon_m}}$, $\hat{e}_r$ and $\hat{e}_\theta$ are the unit vectors of r and θ in spherical dimension. Accordingly, the electric field intensity will be heightened at the direction $\theta = 0, \pi$ for most cases and the field enhancement factor defined as:

$$\eta = \frac{|E|^2}{|E_0|^2} = \left|1 + 2\frac{a^3}{r^3}\frac{m^2-1}{m^2+2}\right|^2 = \left|1 + \frac{\alpha}{2\pi r^3}\right| \qquad (2-19)$$

where α is polarizability of sphere (equation 2-15). K. Tanabe [43] evaluated the effect of different parameters, such as wavelength, distance from the nanoparticle/nanoshell, metal

element, dielectric core material, surrounding medium, and diameter ratio between the core and the shell on field enhancement factor. Figure 2-6 shows the calculated field enhancement factor, η, for different metals. As may be seen, Au, Ag and Al are among the best candidates for field enhancement [41].

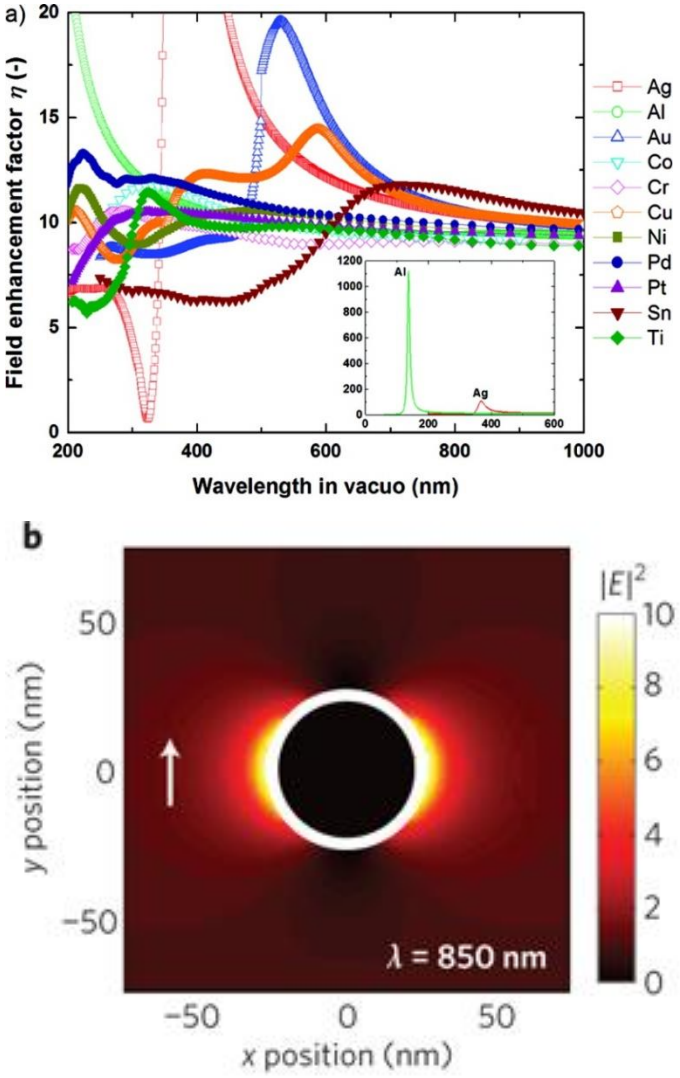

Figure 2-6. a) Calculated field enhancement factors, η, of spherical metal nanoparticles of 11 metals in the air. b) Metal nanoparticles show an intense near-field close to the surface. This Figure is reproduced with permission –See Letters of Copyright Permission (Courtesy of Nature Materials) [21].

Using light concentration through LSPRs is particularly beneficial in materials where the carrier diffusion lengths are small, and photocarriers must thus be generated close to the collection junction area. As well, effective energy conversion depends on the absorption rate in the semiconductor,

which must be larger than the reciprocal of the typical plasmon decay time (life time ~ 10-50fs) to prevent dissipation of the absorbed energy into ohmic damping in metal. This condition is achievable in many organic and direct-bandgap inorganic semiconductors [21].

2-4. FDTD simulation for nanoplasmonics

Relatively rapid descriptions of nanoplasmonic systems can be considered with a computational technique called finite-difference time-domain (FDTD) [44]. The fundamental physical equations that govern classical electromagnetic interactions are Maxwell's equations. These four related equations describe how the electric and magnetic fields interact, subject to environmental and material constraints. They are valid when the system is large enough that quantum considerations can be ignored. The differential forms of these equations (with SI Units in parentheses) are given by:

$$\frac{\partial B}{\partial t} = -\nabla \times E - M \quad (Faraday's\ Law)$$

$$\frac{\partial D}{\partial t} = -\nabla \times H - J \quad (Amper's\ Law)$$

$$\nabla . D = \rho_f \quad (Gauss's law\ for\ the\ electric\ field)$$

$$\nabla . B = 0 \quad (Gauss's law\ for\ the\ magnetic\ field)$$

where in the following symbols are defined:

E: electric field (V/m)

D: electric flux density (C/m^2)

H: magnetic field (A/m)

B: magnetic flux density ($V.s/m^2$)

ρ_f: free charge density (C/m^3)

J: electric current density (A/m^2)

M: equivalent magnetic current density (V/m^2)

$\nabla\cdot$: the vector divergence operator (contribute units of $1/m$)

$\nabla\times$: the vector curl operator (contributes units of $1/m$)

In linear isotrpic nondispersive material (i. e. materials having field-independent, direction-independent, and frequency-independent electric and magnetic properties), D to E and B to H can be related using simple proportions:

$$D = \varepsilon E \quad and \quad B = \mu H$$

where ε and μ are the complex electric permittivity ($C^2/J.m$) and magnetic permeability (N/A^2), respectively.

In the classical sense, these equations are exact in the limit that the space and time differentials (dx, dy, dz, and dt in Cartesian coordinates) go to zero. While this is possible mathematically, it is not possible to implement computationally. In practice, simulations are done with small "finite differences" Δx, Δy, Δz, and Δt in place of the infinitesimal differential elements dx, dy, dz, and dt in Maxwell's equations. Both the discrete and finite difference equations can be used with appropriate boundary conditions and material parameters to simulate classical electromagnetic problems [44]. As the finite differences become smaller and approach zero, the simulations grow more accurate, converging to classically "exact" solutions of Maxwell's differential equations in the zero limit.

One significant challenge for numerical methods is the fact that, even in their simplest forms, Maxwell's equations contain two strongly coupled differential equations with three different spatial coordinates. This can easily lead to numerical instabilities and computational problems if the electric and magnetic fields are calculated at the same points and times. Most FDTD electromagnetic simulations today adhere to a variation of the "Yee" methodology, [44] illustrated in Figure 2-7, because it applies clever "leap-frog" techniques that prevent these problems. Basically, the electric and magnetic field components are calculated on separate interwoven spatial grids at distinct, alternating time steps. This allows the electric field to be calculated completely and independently before it is used to calculate the magnetic field, and

vice-versa. The electric field at one particular time, along with the spatial grid, is used to calculate the magnetic field at a later time on a different spatial grid. The newly calculated magnetic field is then used to calculate the electric field at the next time step, and so on.

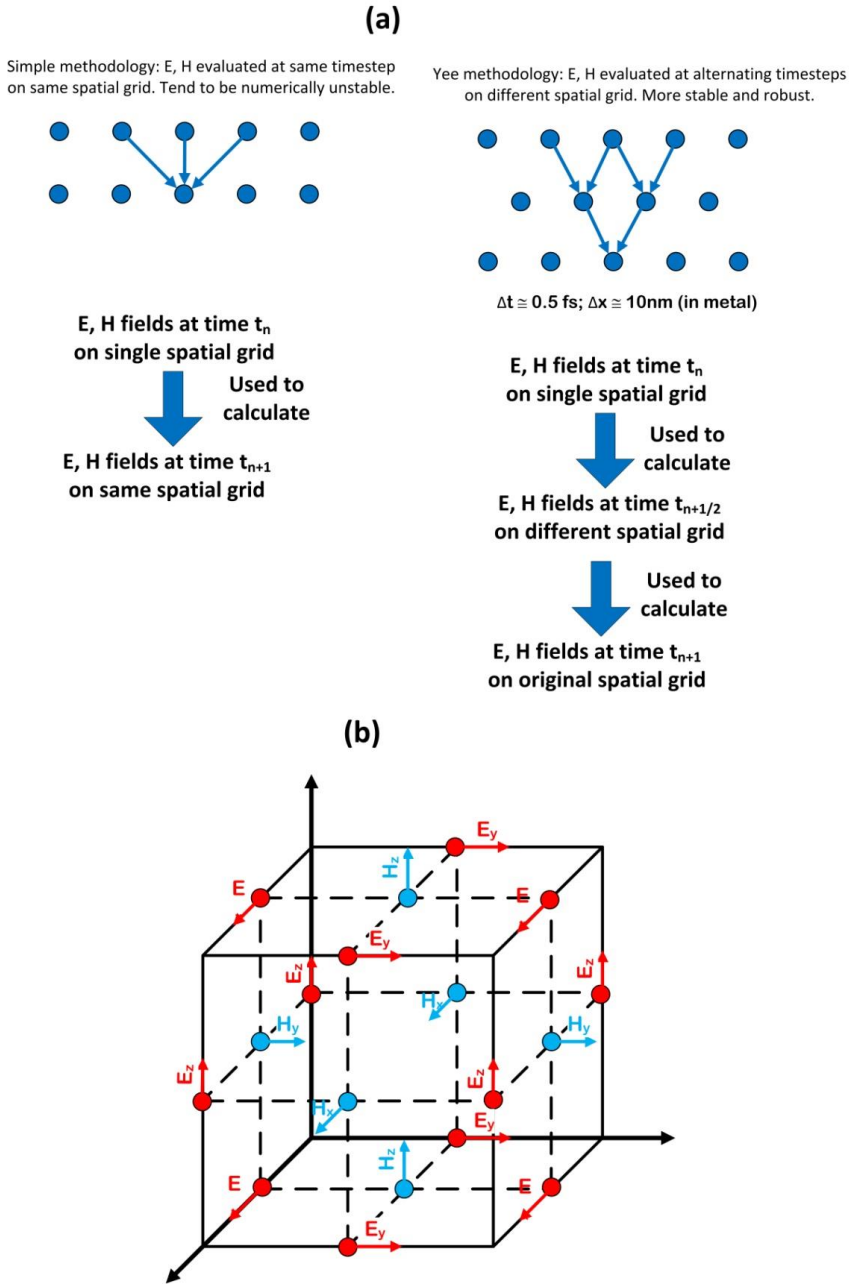

Figure 2-7. (a) Simple methodology compared to Kane Yee's "leapfrog" methodology for 1- dimensional system. (b) Representation of 3-dimensional Yee cell that illustrates the different spatial grids for the various electric and magnetic fields [44].

2-5. Thesis Objectives

The main objectives of current thesis is : "Enhanced Ultra-Thin Film Nanocrystalline Silicon Photovoltaic Device Architecture". To achieve this, following objectives are considered:

1. • TCO development for ultra-thin film solar cells with enhanced conductivity and transmission.
2. • Develop and optimize nanocrystalline silicon thin film solar cells.
3. •Theoretical understanding of design parameters for nanoplasmonic architectures in ultra-thin film solar cells.
4. • Develop a simple and scalable technology for nanoplasmonic structures integrable for solar cells.
5. • Integrate the nanoplasmonic architectures to ultra-thin film solar cells.

The research work flow for execution of the above objectives is demonstrated in the Figure 2-8.

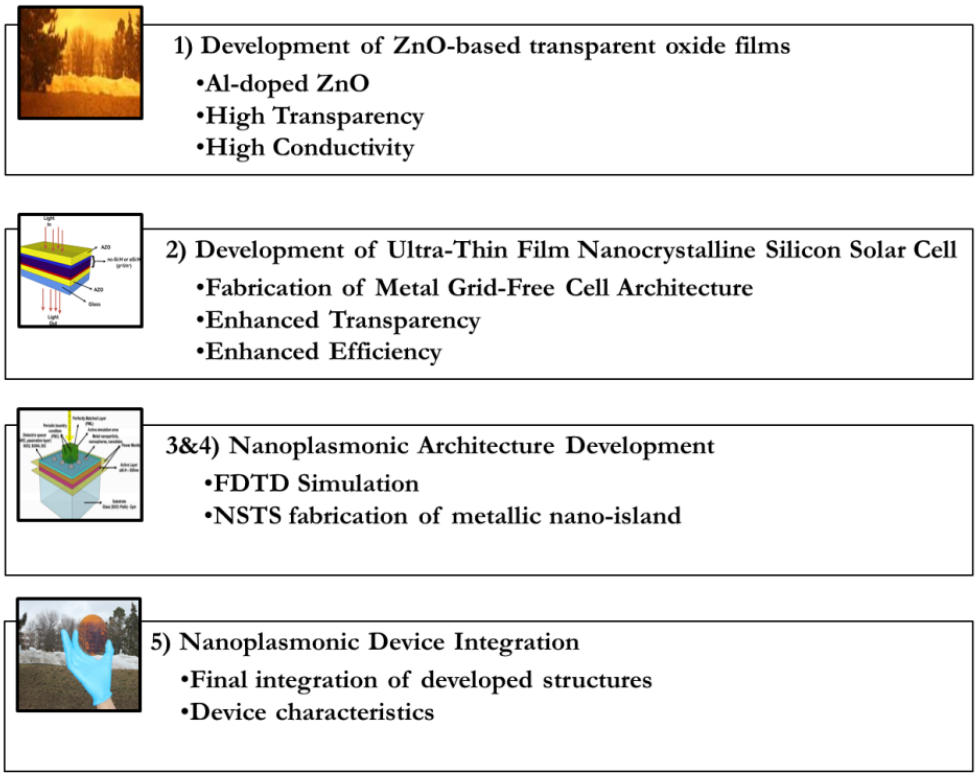

Figure 2-8. Work flow of research conducted in this PhD thesis.

2-6. State-of-the-art

The main novelty of the present research is the investigation of nanoplasmonic architectures for ultra-thin film devices. There have been numerous studies on the development and parameterization of nanoplasmonic structure based on metallic nanoparticle arrays for crystalline silicon wafer [21][22][38] and thin film solar cells [35][39].

V. E. Ferry and et al. [35][39] for the first time investigated the advanced light management based on nanoplasmonic structure for aSi:H thin films. Their main focus was to improve the performance of ultra-thin film n-i-p aSi:H solar cells by developing nanoplasmonic back-reflector structure by using large-scale nanopatterning method, SCIL (substrate conformal imprint lithography). She investigated and established design criteria for her suggested structure for difference thin film thickness [35][39]. Moreover, she demonstrated a 10% performance enhancement mainly due to the increase of light absorption and the IR region of solar spectrum in thin film solar cells [39].

Regarding the design parameterization, there have been numerous efforts to establish criteria and guideline for designing nanoplasmonic structures [38][39]. Different parameters mainly focused on metallic type and nanoparticle array parameters. R. Santbergen and et al. studied the effect of silver nanoparticle shape and dielectric constant of embedded medium on the amorphous silicon thin film developed [45]. He observed that parasitic absorption is the key disadvantage of using silver nanoparticle for top of the solar cells.

There has not been a systematic study on the parameterizing of metallic nanoparticle array for application as nanoplasmonic architecture for semi-transparent nanocrystalline silicon thin film solar cells. In this these a systematic approach provided through FDTD simulation to distinguish the effect of different elements in performance of metallic nanoparticle array for nanoplasmonic enhancement in ultra-thin film devices. The effect of absorber layer thickness, different spacer materials and thickness is investigated and optimized array characteristics for the best performance structure reveled. Additionally, the dependency of metallic materials to the array characteristic is investigated.

In the materials development section, the main focus is to develop an enhanced TCO based on the Al-doped ZnO as accost effective transparent conductor applicable for ultra-thin film solar cells. For nanoplasmonic structure development the main approach is on the development of a scalable and simple technique for the large area development of nanoplasmonic architecture suitable for ultra-thin film devices.

Chapter

3

Semi-Transparent Nanocrystalline Silicon Ultra-Thin Film Device Development-I: Development of Transparent Conductive Oxide

This chapter presents the development of semi-transparent nanocrystalline silicon (ncSi:H) ultra-thin film devices to be used as a platform for the integration of nanoplasmonic structures. The new transparent nc-Si solar cell with p-i-n configuration is developed on glass substrates incorporating highly conductive aluminium doped zinc oxide (AZO) films as top and bottom electrodes.

3-1. Introduction: why ultra-thin film nc-Si:H?

The ultimate goal of this PhD research is to design and fabricate nanoplasmonic architecture for enhanced ultra-thin film structure. The aim is to create a new route for the development of efficient cost effective photovoltaic devices. There are two primary motivations for this approach:

1- Reducing the active layer thickness by nanoplasmonic light trapping not only reduces cost but also improves the electrical characteristics of solar cells. First of all, reducing the film thickness reduces the dark current (I_{dark}), causing the open-circuit voltage (V_{oc}) to increase, as

$$V_{oc} = \left(\frac{K_B T}{q}\right) ln\left(\frac{I_{photo}}{I_{dark}} + 1\right)$$

where K_B is the Boltzman constant, T is temperature, q is the charge, and I_{photo} is the photocurrent. Consequently, the cell efficiency rises in logarithmic proportion to the decrease in thickness, and is ultimately limited by surface recombination.

Figure 3-1 shows simulated absorption spectrum for 2µm silicon in comparison with 300nm and 200nm amorphous silicon. In this simulation single path absorption and no reflection is assumed. It reveals that 200nm-300nm thin film amorphous silicon could have equal absorption as 2µm crystalline silicon film. It shows the potential of ultra-thin film amorphous silicon for enhanced solar cell absorption for fabrication of ultra-thin film devices with acceptable efficiency suitable for specific applications such as transparent solar cell for building application.

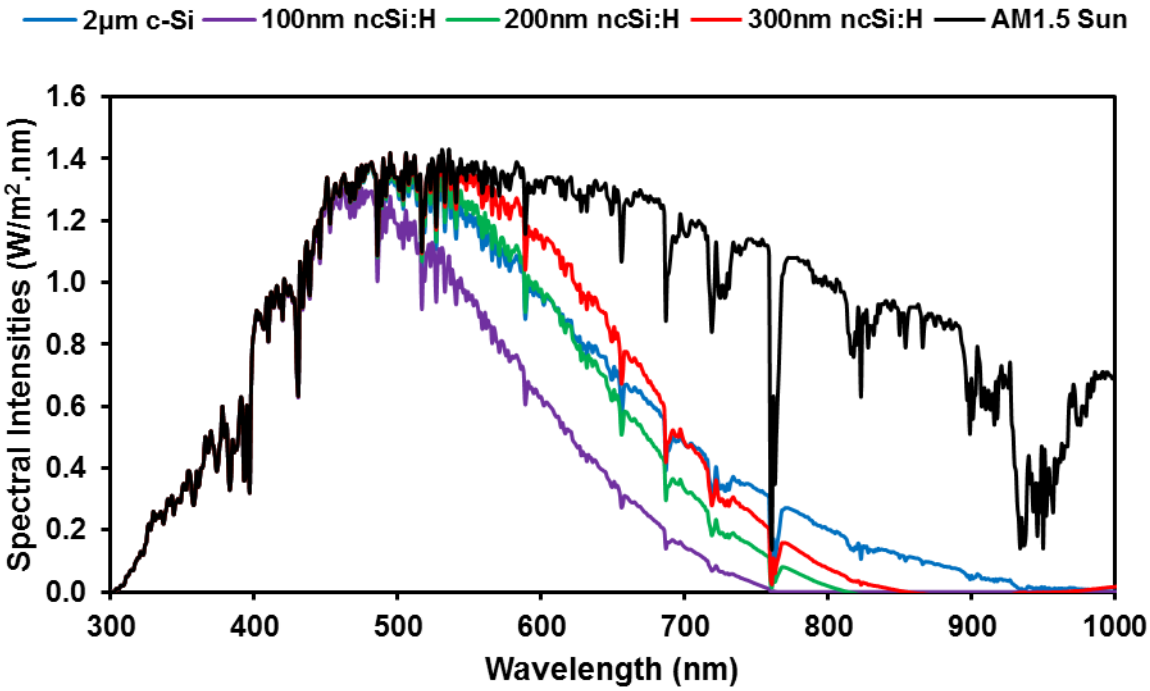

Figure 3-1. Solar absorption spectrum simulated graph for 2µm silicon, 300nm amorphous silicon, and 200nm amorphous silicon with AM1.5 solar spectrum.

2- Reducing the carrier recombination in thin-film geometry as carriers requires travel of only a small distance before being collected at the junction. This leads to a higher photocurrent. Additionally, greatly reducing the semiconductor layer thickness allows the use of semiconductor materials with low minority carrier diffusion lengths, such as a-Si, polycrystalline semiconductors, quantum dot layers, or organic semiconductors.

As well, the advancement of transparent photovoltaics empowers the building-integrated photovoltaics (BIPV), making it one of the fastest growing segments of the photovoltaic

industry. Among current technologies, ultra-thin film solar cells have promising potential as a transparent cell to be replaced by conventional glass or placed over the glass. The main challenge is to incorporate good transparency with acceptable photovoltaic efficiency.

To achieve this goal, certain issues must be addressed, particularly those regarding an enhanced conductive dopant layer, high efficient thin absorber layer, and high conductive transparent conductive oxide are. Ultra-thinnanocrystalline silicon, due to higher electron mobility and transparency with good optical absorption, is a prospective candidate for transparent solar cells. In addition, incorporating nanocrystalline silicon material as the absorber layer in single or tandem thin-film solar cells greatly enhances the spectral efficiency and stability of these devices.

In the current chapter, an investigation is done on the development of new transparent solar cells with enhanced photovoltaic conversion efficiency, through the incorporation of nanocrystalline silicon thin films and the full elimination of metallic contact to increase active device area and transparency.

For this approach, as demonstrated in Figure 3-2 , a new p-i-n nanocrystalline silicon (nc-Si) solar cell with enhanced high conductive aluminium doped zinc oxide (AZO) was developed.

To achieve this goal, optimization and investigation of the following processes have been accomplished:

1. Optimization of AZO sputtering deposition at low pressure and moderate power with enhanced conductivity and transparency.
2. Development of nanocrystalline silicon absorber layer with enhanced absorption at a high rate and low temperature from pure silane in a modified ICP-CVD system.
3. Optimization of doped and undoped micro and nanocrystalline silicon layers at a temperature of 300˚C.
4. Single junction p-i-n devices optimization and fabrication on glass substrate at a temperature of 300˚C.

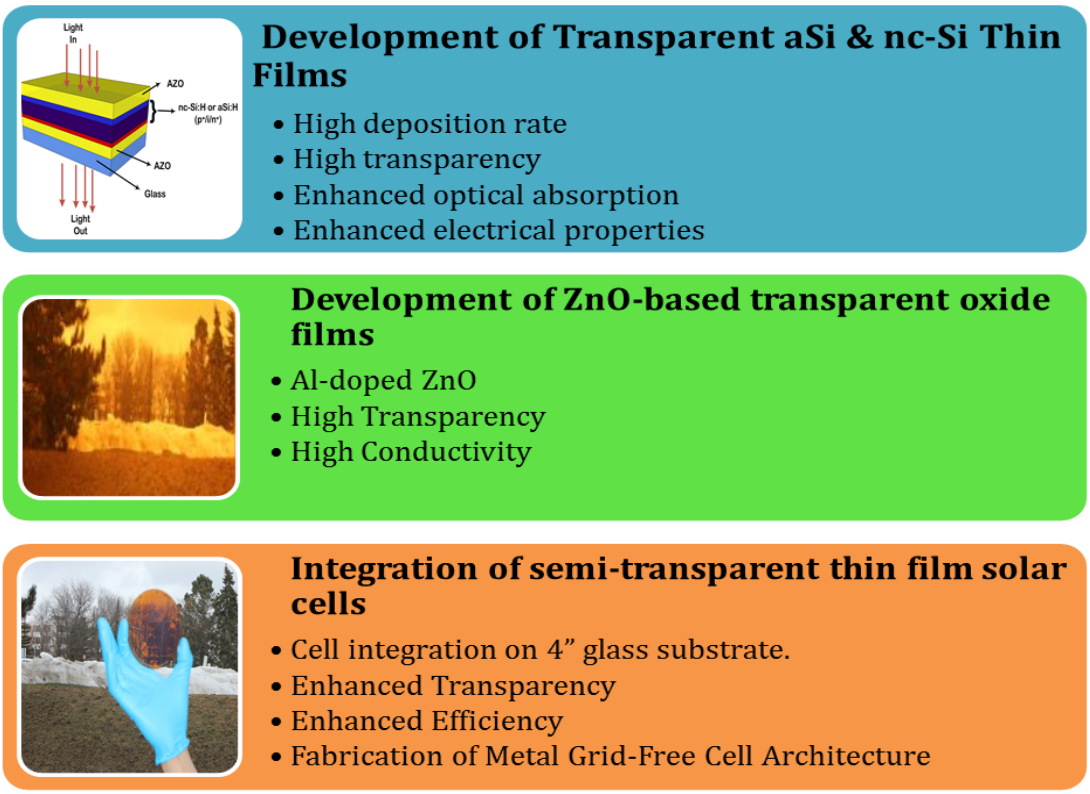

Figure 3-2. Development procedure for fabrication of enhanced semi-transparent nanocrystalline ultra-thin film solar cells

3-2. Optimization of Al-doped ZnO

An Achilles' heel for the development of enhanced ultra-thin film device is the incorporation of a transparent conductive layer with good transparency and conductivity. Transparent Conductive Oxides (TCOs), due to their compatibility with low-temperature fabrication methods and their high mobility compared to nano-crystalline silicon (nc-Si:H), have proven functionality for application in amorphous/nanocrystalline silicon thin-film solar cells[46].

Among TCOs, ZnO is an interesting candidate since zinc (Zn) is inexpensive, abundant, and non-toxic. Additionally, its large intrinsic band gap (~3 eV) creates high transparency in visible range (>80%), which makes it an attractive candidate for transparent solar cells as well. Furthermore, their low absorption in UV range and the ability to be doped with more available elements (boron, aluminium, gallium or indium) enable to tune its conductivity.

ZnO and Aluminium doped zinc oxide (Al:ZnO) thin films are prepared by a variety of techniques such as evaporation, pulsed laser deposition, chemical deposition, metal-organic chemical vapor deposition (MOCVD), spray pyrolysis, and magnetron sputtering. Among these techniques, magnetron sputtering is of particular interest, since it offers a low temperature deposition, robust process, repeatability, uniformity, and large area fabrication adaptability.

Sputtered Aluminium doped zinc oxide (Al:ZnO or AZnO) is often used as a transparent front contact and back reflector for light trapping in first generation solar cell technology [47][48][49][50]. Al:ZnO is also widely used as a transparent electrode in second generation thin film solar cells [48]. Sputtered Al:ZnO is a degenerated, semi metallic and highly conductive TCO. Resistivity of sputtered Al:ZnO has been lowered down to that of ITO ($\rho \sim 10^{-4}$ Ω.cm) over the past decade. The resistivity of impurity doped zinc oxide TCOs have been reduced to the range of 10^{-5} Ω.cm under controlled laboratory conditions, by increasing the carrier concentration up to1.5×10^{21} cm^{-3} [49][50]. Although a high carrier concentration might be desirable for better electrical properties, it remains comparably unfavorable in terms of optical properties, particularly in higher wavelengths range. The heightened number of free carriers increases light reflection, due to free electrons oscillations above a wavelength known as plasma frequency. This effect is mainly prominent in near infrared and infrared, where a decrease in light transmission is accordingly caused [51]. Consequently, in thin-film solar cell applications, or some third generation solar cell applications where a high transmission in the range of 400 nm-1300 nm is required, it is desirable to have a control over carrier concentration and mobility to optimize the reflection from free-electron oscillations above plasma frequency [52][53][54][55].

3-2-1. Development and Optimization of Al-ZnO TCO Thin Films: Methods and Materials

Al doped zinc oxide film was developed in collaboration with Navid. S. Jahed at CAPDS. The method is as follows:

Radio frequency magnetron sputtering was used as a deposition technique on corning glass (Eagle XG) in an Intel Vac. sputtering tool. Ceramic discs of Al_2O_3: ZnO (2 wt %), with a purity of 99.999% and diameter of 3 inches from Angstrom sciences, were applied as an Al:ZnO target. Standard RCA cleaning procedures were employed to clean the samples prior to loading them into the chamber. The samples were then placed parallel to the targets in four sample holders at a distance of 50 ± 3mm.

To improve the uniformity (>94%) a mechanical system was designed to provide both revolution (for 4 sample holders) and rotation (for each individual sample holder) motion to the sample holders batch (Figure 3-3). The sample holder batch had 40 revolutions per minute, while each individual sample holder possessed rotations of 14 per minute. The chamber was left for 24 hours to reach a background pressure of 1×10^{-7} torr before each deposition. The non-reactive deposition was carried out in Ar as an inert gas inside the chamber. The deposition pressure varied between 0.5 mtorr and 10 mtorr. The pressure was stabilized during the deposition by controlling the gas flow rate with mass flow controllers. The deposition power varied within the range of 80W to 300W. Deposition temperature was controlled by a thermocouple placed in the vicinity of sample holders. Temperature controller was recalibrated to match the temperature readings of the reference temperature logger temporarily placed on the back of the substrates for more accurate readings. The temperature was stabilized inside the chamber by 1 hour, preheating the chamber at deposition temperature. Prior to every deposition, 2 minutes of pre deposition (with closed shutter) was performed at 100 (Wrf) to clean up the surface of the targets, followed by a 1 minute warm up at deposition power. The deposition was performed with stabilized plasma for up to 120 minutes.

The sheet resistance of the samples was measured with a four point probe system right after unloading them from the chamber. The samples were patterned by a UV lithography mask aligner system (OAI: optical associates incorporation) and wet etched in a solution of 10% HCl in water. The thickness of the samples were measured using a stylus-type profilometer (Dektak 150). The transmission of light on samples prepared on corning glass was measured using a PerkinElmer UV/VIS/NIR Lamda 1050 spectrometer, with air as the reference. The open

source PUMA software was used to verify the thickness on Al-ZnO coated glasses and attain the refractive index using the transmission spectra of the samples [56].

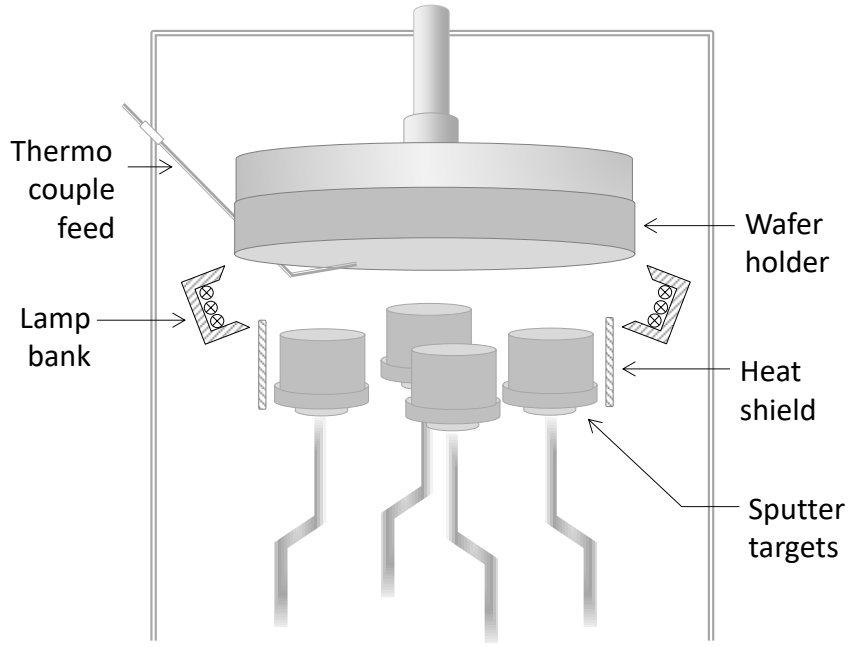

Figure 3-3. Schematic representation of the modifications made to the sputtering system for heating and temperature monitoring.

The carrier concentration and mobility of the films were characterized by a Hall Effect experiment in a Van der Pauw configuration, with Ecopia HMs-300 setup in a magnetic field of 0.54 T at room temperature. To avoid temperature effect on the films instead of making contact with soldering of In-Sn or E-beam deposition of Al/Ti , silver paste was used to make Ohmic contact on the Al-ZnO coated glass samples when possible. Samples were diced from the centre of 4-inch coated glass wafers. Compared to the alternative ways of making Ohmic contact, silver paste provided faster and acceptably lower resistivity Ohmic contact.

Prior to every Hall measurement experiment, the I-V characteristic of our samples prepared in Van der Pauw configuration was studied to ensure that contacts were Ohmic. The Hall measurement current was adjusted accordingly for every sample to have a meaningful Hall measurement experiment.

3-2-2. Results and Discussion

3-2-2-1. Sputter deposition at room temperature: Optimization of RF power and pressure

Al:ZnO films can be sputtered from Al_2O_3:ZnO targets with different Al_2O_3/ZnO weight ratios, often referred to as target doping concentration (TDC). Ceramic Al_2O_3: ZnO targets with TDCs of 0.5%, 1%, 2% and 4% are available. Al_2O_3:ZnO targets with 2% TDC are of particular interest since they result in the least thickness dependent resistivity in the thin films [57]. Moreover, lowest reported resistivity is achieved by targets with TDC of 2%[58].

Deposition pressure is the sputtering parameter that strongly affects electrical properties of AZO thin films. As a rule of thumb, at higher pressure, the deposition rate is lower because of a smaller mean free path in particles. In dynamic sputtering systems (with rotation and/or revolution motions), the deposition rate is several times lower than stationary systems. As a result in dynamic sputtering systems, it is desirable to optimize sputtering parameters for high quality, conductive AZnO thin films at lower pressure to increase target life and reduce material waste.

The first phase of experiments were carried out under different deposition pressure and P_{RF} conditions. Table 3-1 summarizes the electrical properties of Al-doped ZnO samples prepared from ZnO:Al2O3 targets, which have 2% TDC at different pressures and powers. Figure 3-4 shows the AZO film deposition rate under different conditions at room temperature. The deposition rates were obtained from the measured film thickness and deposition time. A general trend of increased deposition rate with increased P_{RF} and with decreasing pressure was observed. The sheet resistance of samples is measured right after unloading them from the chamber measured by four point probe measurements. The resistivity (ϱ) of the samples was also measured by Van der Pauw set up as part of the Hall analysis. The films deposited at the highest pressure (10 mT) were found to be not stable, showing varying (increased) resistivity over time.

Table 3-1. Variation of electronic transport parameters Sheet resistance (R_{sh}), Resistivity (ρ), Carrier concentration (N_e) and Hall mobility (μ) of the ZnO:Al films sputtered on glass substrate at room temperature with different deposition power and pressure.

Chamber Condition	RF Power (Watt)	Rate of deposition (A^0/min)	R_{Sh}* (Ω/sq)	Film resistivity ρ (Ω.cm)	Carrier concentration N_e (cm^{-3})	Hall mobility μ ($cm^{-2}V^{-1}s^{-1}$)	Rate (nm/ min)	Thickness (nm)
Pressure: 10 mtorr Ar flow: 165sccm	200	36.67	504	6.18E-03	1.34E+20	7.563	3.67	220
	150	21.7	79	2.24E-01	1.79E+20	0.155	2.17	130
	120	6.61	1505	2.95E-01	4.829E+20	0.0438	0.67	80
Pressure: 5 mtorr Ar flow: 120sccm	240	70	130	2.24E-02	6.19E+19	4.496	7.00	420
	150	41.7	249	4.70E-02	6.60E+19	2.018	4.17	250
	80	18.3	287	3.09E-03	9.30E+19	0.217	1.83	110
Pressure: 2 mtorr Ar flow: 80 sccm	300	125	51.6	3.33E-02	1.817E+20	1.032	12.50	750
	200	49.3	18.8	1.33E-01	1.19E+19	3.956	4.93	740
	100	36.7	263	3.62E-03	1.75E+20	9.834	3.67	220
Pressure: 0.5mtorr Ar flow: 50 sccm	200	79.2	25.2	2.017E-03	3.75E+20	8.182	7.92	950
	150	56.7	27.2	1.52E-03	5.51E+20	7.57	5.67	680
	100	36.25	43.4	1.9E-03	2.67E+20	8.805	3.63	435

* Sheet resistance of all of the samples are measured right after deposition whereas Hall experiment is performed after a week.

A possible reason for this could be the diffusion of atmospheric oxygen in the AZO film. As suggested in [59][60], enhanced oxygen diffusion in thinner films and in humid ambient can lead to a decrease in carrier concentrations and mobility, both of which can lead to degradation of film conductivity. In AZO films, impurity atoms (Al) and oxygen vacancies constitute the carrier concentration, and the diffusion of oxygen reduces the free carriers from oxygen vacancies. It seems that for films deposited at high pressure, the oxygen vacancy is the main source of free carrier concentration [57]. When the deposition is carried out at higher

temperatures, more Al dopants are activated and the oxygen diffusion effect is diminished on the electrical stability of the films. As we will see later on, other experiments carried out with the in-situ substrate heating system resulted in good electrical and optical properties. The other problem encountered during deposition at high pressure was the arcing in the plasma at high P_{RF} (>150W). This causes re-deposition of AZO from coated films on the sample holder leading to the appearance of black spots on the samples. This effect does not happen at lower deposition pressures.

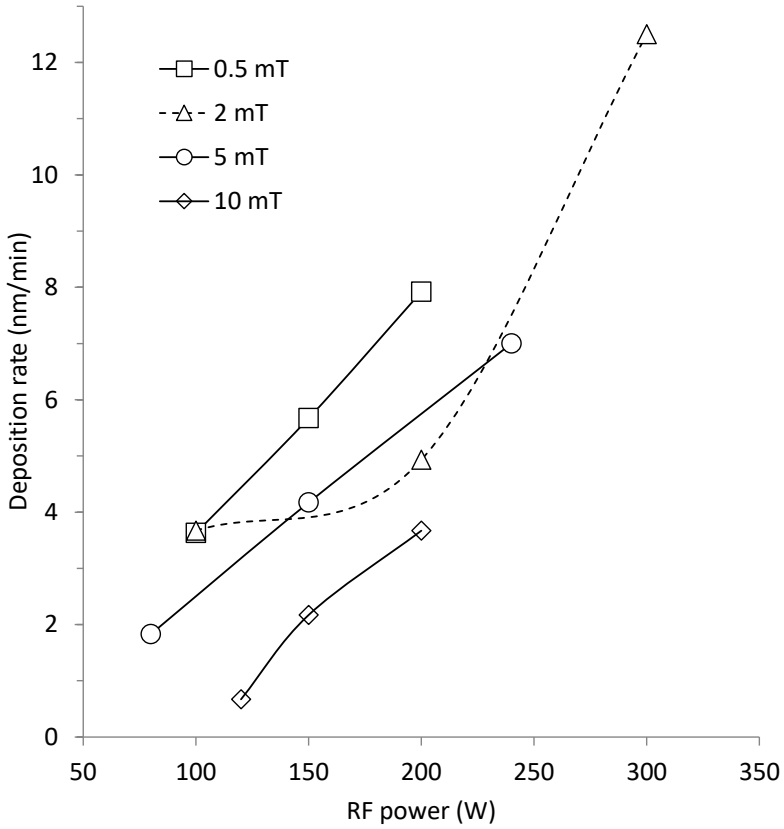

Figure 3-4. Sputter deposition rate of the AZO films under different chamber pressure and RF power conditions. All films were deposited at room temperature. The points are connected to guide the eye.

Figure 3-5 shows the ϱ values of the stable AZO films deposited at room temperature in the pressure range of 0.2 - 5 mT. The films deposited at 0.5 mT yielded low ϱ values, the lowest being 1.52 x 10^{-3} Ω-cm for the P_{RF} of 150W. It can also be observed that for the pressure of 0.5 mT the ϱ values are much less sensitive to RF power variation compared to other pressures. For these reasons, a pressure of 0.5mT and a P_{RF} of 150W were chosen for the next phase of

experimental investigation to study the effects of substrate heating with the aim of further reducing ϱ.

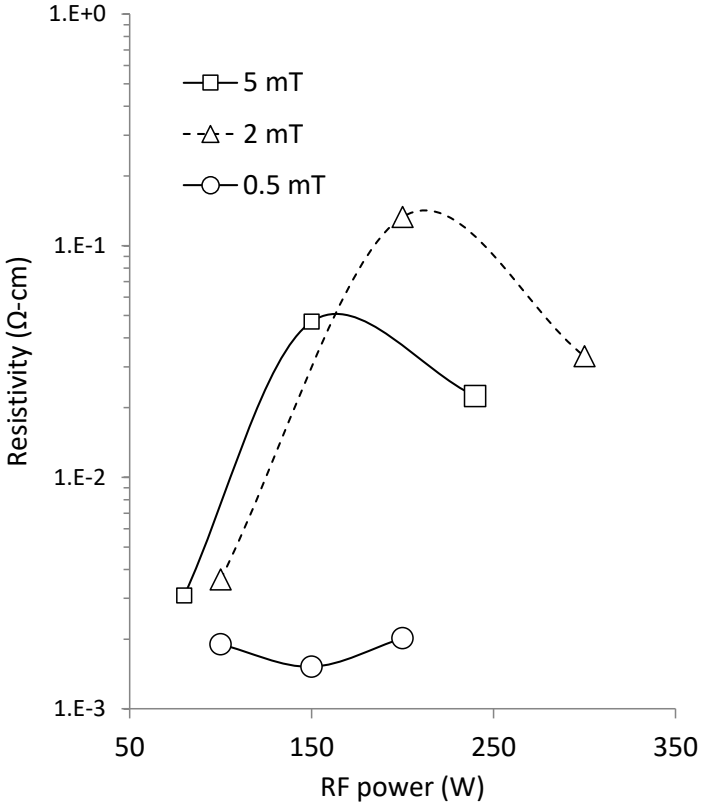

Figure 3-5. Resistivity of the sputtered AZO films under different chamber pressure and RF power conditions. All films were deposited at room temperature. The points are connected to guide the eye.

3-2-2-2. Sputter deposition with in-situ heating and film characteristics

In another set of experiments, for the deposition with *in-situ* heating, the three lamp-banks in the modified heating setup provided uniform heating of the substrates. The temperature was kept at the desired values during the deposition thanks to the control system. For these experiments the deposition pressure and P_{RF} were kept at 0.5mT and150W respectively. Film resistivity and carrier concentration were measured by Van der Pauw and Hall measurements, and the carrier mobility was extracted. Table 3-2 gives the electrical parameters of the AZO films. A steadily decreasing trend in resistivity was observed with increasing deposition temperature.

Table 3-2. Electrical parameters of the sputtered AZO films deposited at different temperatures

Deposition Temperature (°C)	Film Thickness (nm)	Resistivity (Ω cm)	Carrier density (cm^{-3})	Hall mobility ($cm^2/V.s$)
25 (RT)	680	1.52×10^{-3}	5.51×10^{20}	7.45
120	760	1.14×10^{-3}	5.91×10^{20}	9.26
180	775	6.67×10^{-4}	5.57×10^{20}	16.8
250	780	2.94×10^{-4}	1.07×10^{21}	19.8

At the deposition temperature of 250°C a resistivity of 2.94×10^{-4} Ω cm was achieved and this is among the lowest recorded resistivity for the AZO films. The carrier concentration significantly increased, to a value of 1.07×10^{21} cm^{-3}, for the deposition temperature of 250°C. The extracted mobility also showed an increasing trend with temperature. The ZnO:Al system undergoes a transition from metal-semiconductor to metal-like behaviour at increased deposition temperatures, and this transition is attributed to the competition between thermally activated carriers and scattering effect of free carriers in a degenerate semiconductor [61].

The optical transmission of the films is represented in Figure 3-6. Transmission of light in visible range is above 85% for all samples. Demonstrably, by increasing deposition temperature, there is a continuous decline in light transmission in the infrared region. This decrease in light transmission, within the infrared range, occurs because of the rising trend observed in carrier concentration when the deposition temperature falls. The refractive index at λ=550nm (n_{550}) was obtained using the procedure described in [62]. For the curves in Figure 3-6, the values of n_{550} were 1.85, 1.89, 1.85, and 1.86 respectively from RT through 250C°.

The structural analysis, investigated by low angle X-Ray Diffraction, is presented in Figure 3-7(a) for the samples prepared at pressure 0.5mTorr, and at different temperatures (room temperature and 250°C). The X-ray diffraction pattern shows that both films are polycrystalline hexagonal wurtzite structure associated with ZnO with a preferred crystallographic orientation in the (103) plane. To calculate the mean crystallite size (d) the Scherrer formula [63] is used as following equation:

$$D = \frac{K\lambda}{\beta cos\theta} \qquad (3-1)$$

where D is the crystallite size, K represents a shape factor with standard value of 0.9, λ is the wavelength of the x-ray (Cu Kα, 0.15406 nm), β is the value of the Full Width at Half Maximum (FWHM) of diffraction peak, and θ corresponds to the Bragg diffraction angle. Table 3-3 summarizes the crystallite size and lattice parameters extracted from the measured d-spacing and using the lattice constants for the hexagonal wurtzite structure in equation (3-2) [64].

$$\frac{1}{d^2} = \frac{4}{3}\left(\frac{h^2 + hk + k^2}{a^2}\right) + \frac{l^2}{c^2} \qquad (3-2)$$

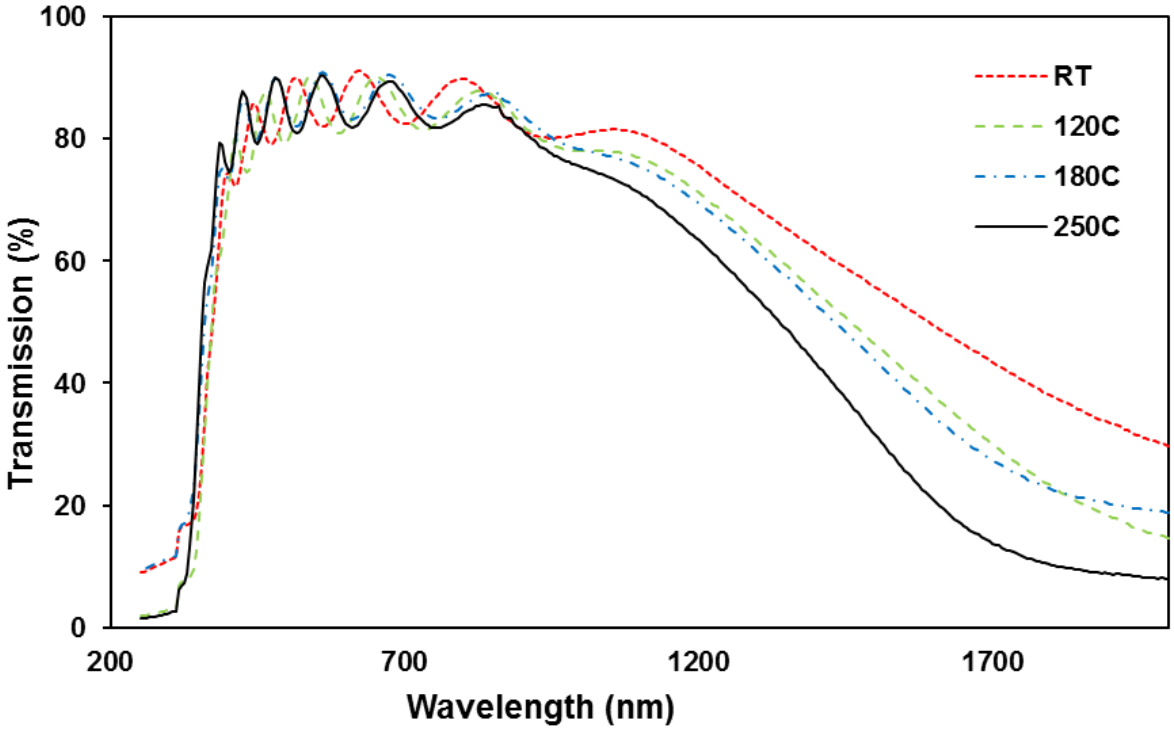

Figure 3-6. Change in Transmission of ZnO:Al film deposited at pressure=0.5 mtorr, Power=150 Wrf with respect to deposition temperature.

Regarding the main crystal peak (103), both samples has similar peak intensity which indicates that the crystal structure is not degraded, although by increasing deposition temperature grain size increases. Comparing the FWHM for the two films shows that at high temperature thin film has slightly better quality since FWHM is decreased [63].

To further elaborate the effect of the Al addition and temperature on the structure of ZnO, thin films of ZnO were prepared with the same deposition parameters as AZO at 250°C. Figure

2(b) shows the diffraction pattern of AZO and ZnO prepared at a high temperature. Table 3-3 summarizes the lattice parameters, the (002)/(103) peak intensity ratios (I(002)/I(103)), and crystallite size calculated by Scherrer equation.

Table 3-3. Calculated lattice parameters, (002)/(103) peak ratio and crystallite size for AZO at RT and 250°C and ZnO at 250°C.

Sample	Lattice parameters (Å)	$I_{(002)}/I_{(103)}$	Crystallite size (nm)	d-spacing (nm)
AZO-RT	a=b=3.22 c=5.24	5.141E-3	11.92	0.148
AZO-250T	a=b=3.23 c=5.20	61.823E-3	12.94	0.147407
ZnO-250T	a=b=3.26 c=5.20	8507.475E-3	17.2	0.14769

A comparison of the results reveals that doping of Al in ZnO is changing the dominant crystal orientation from (002) in ZnO to (103) in AZO. In addition, considering the FWHM which in ZnO for (002) is 0.3936° and in AZO for (103) is 0.72°, indicate that the quality of the film decreased with slight incorporation of Al in the developed thin film.

Calculation of crystallite size, utilizing the Scherrer equation, proves that ZnO also has a higher crystallite size of 17.2 nm when compared to that of 12.94 nm for AZO. As well, increasing deposition temperature has a minor effect on the increase of crystallite size for AZO.

The higher I(002)/I(103) shows a higher tendency towards the c-axis direction orientation, and the smaller value of I indicates the greater likelihood of thin film to become disordered. In conclusion, the incorporation of Al in ZnO degrades the structural quality of the film by introducing defects and influencing the dynamics of grain growth through the enhanced formation of nano-crystallites in grain boundaries [65]. Increasing deposition temperature eliminates these negative effects and improves the crystal quality of the film.

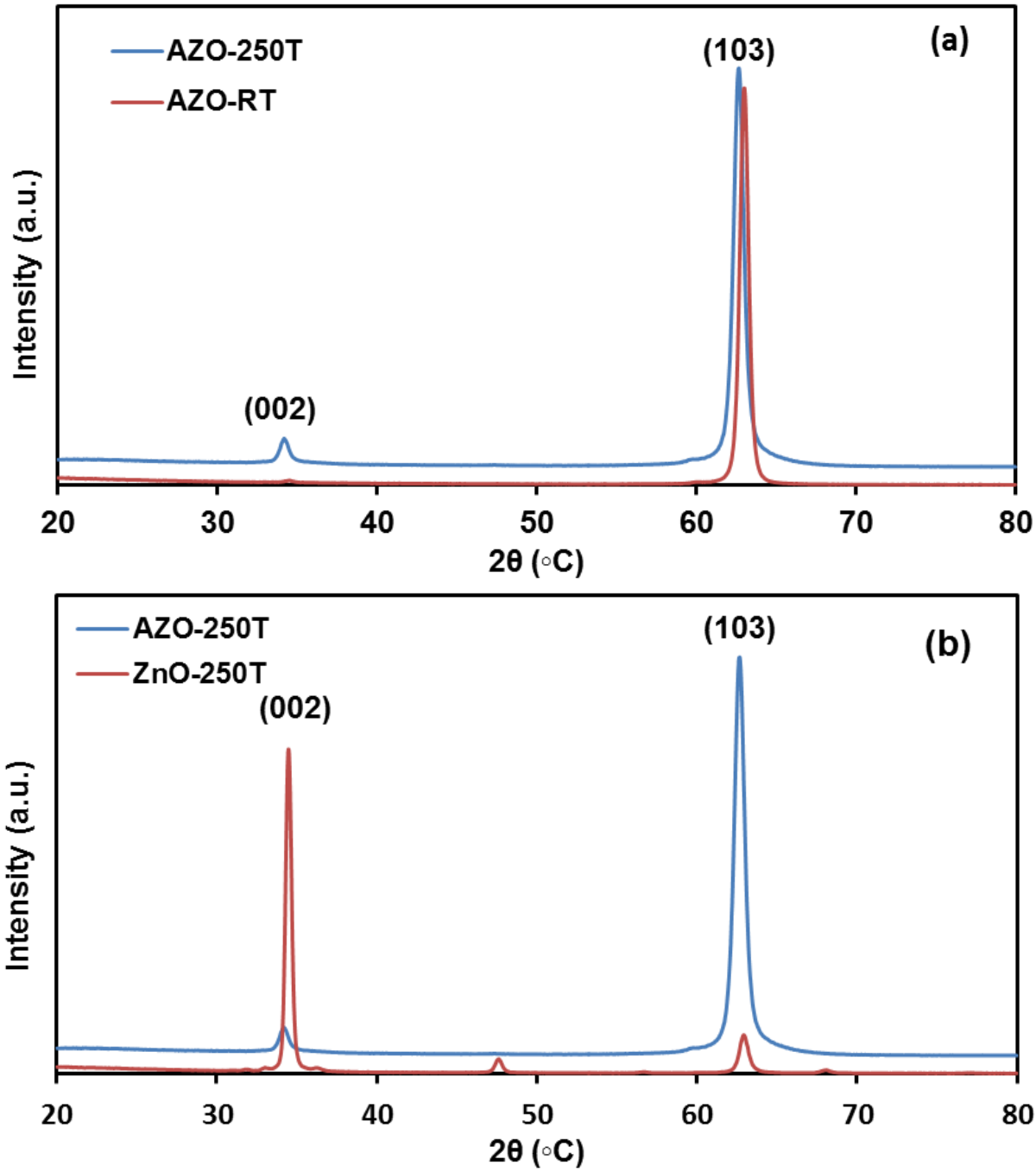

Figure 3-7. a) XRD analysis of a) ZnO:Al film deposited at pressure 0.5 mTorr, Power 150 Wrf and different temperatures (room temperature and 250°C). b) Comparison of the X-ray diffraction pattern of ZnO:Al with ZnO at the same deposition condition (pressure 0.5 mT, power 150 Wrf, temperature 250°C).

One important signature of every material is its near band edge photoluminescence (NBEPL). There are several mechanisms responsible for the occurrence of near band edge peaks, such as free exciton emissions (FX), bound excitons (BX), donor-acceptor pairs (DAP), etc. All of these mechanisms have excitonic behaviour and are temperature dependent. Zinc oxide possesses large exciton binding energy (~ 60 meV), which makes it possible to have free exciton emissions up to room temperature [66].

An important precondition for NBE emissions at room temperature is the suppression of non-radiative processes, which corresponds with better crystalline quality. As a result, the presence of NBE emissions is an indication of better crystalline quality. In addition, zinc oxide also has deep level emissions (DLE), typically within the range of 405 nm to 750 nm. The origins of broad band DLEs are still under debate, but it is believed that defects, in the form of zinc vacancy/interstitial and oxygen vacancy/interstitial, are the main cause for the alleged defect related emissions. In order to further study the evidence of structural change in the AZO films due to elevated deposition temperature, photoluminescence (PL) analysis was carried out. Room temperature PL spectra was obtained, with a 310 nm excitation, for the AZO films deposited at RT and 250°C. The near band edge (NBE) photoluminescence can be an important indicator of material quality [67]. Room temperature NBE emission requires the suppression of non-radiative processes and this corresponds to better crystalline quality. The occurrence of NBE peaks are caused by mechanisms such as free exciton emission, bound exciton, or donor-acceptor pair. These mechanisms are temperature dependent and have excitonic behaviour. Zinc oxide (ZnO) has a large exciton binding energy (~ 60 meV) which makes it possible to have free exciton emission up to room temperature [68]. In addition to NBE emission, ZnO has also deep level emissions (DLE) at room temperature in the 2.5 eV (497nm) to 1.95 eV (637nm) range [69]. It is believed that the defects in the form of zinc vacancy/interstitial and oxygen vacancy/interstitial are the main cause for the DLEs [70]. For ZnO materials the defect energy levels responsible for DLEs have been calculated using full potential linear muffin-tin orbital method and attributed the DLE peak at 426nm to zinc vacancies and those at 595nm and 615nm to oxygen interstitials [71]. Also ratio of intensities (I) between the I_{NBE} and I_{DLE} peaks have been correlated to the material quality in ZnO films [72]. Therefore the room temperature

PL spectra of the AZO films also can provide important information on changes in the material structure.

Room temperature photo luminescence spectra of ZnO:Al films deposited at 150 (Wrf) and 0.5 mtorr at different deposition temperatures on glass substrates are shown in Figure 3-8. In the PL spectrum of the film deposited at RT the NBE peaks are hardly noticeable except for two rather suppressed peaks at 370and 382nm. For this sample, three DLE peaks are visible at 422, 465, 743nm. On the other hand, the sample deposited at 250°C clearly exhibits NBE peaks at 366 and 393 nm, and DLE peaks at 460, 680, and 736 nm. The peak seen at 620 nm in both samples is a measurement system artefact coming from second harmonic of the 310nm excitation source. Given the prominent NBE peaks for the 250°C case, and the fact that I_{NBE}/I_{DLE} changed from ≈0.652 to ≈2.898 from the RT to 250°C cases indicate the structural change crystalline quality improvement that are attributable to the high deposition temperature.

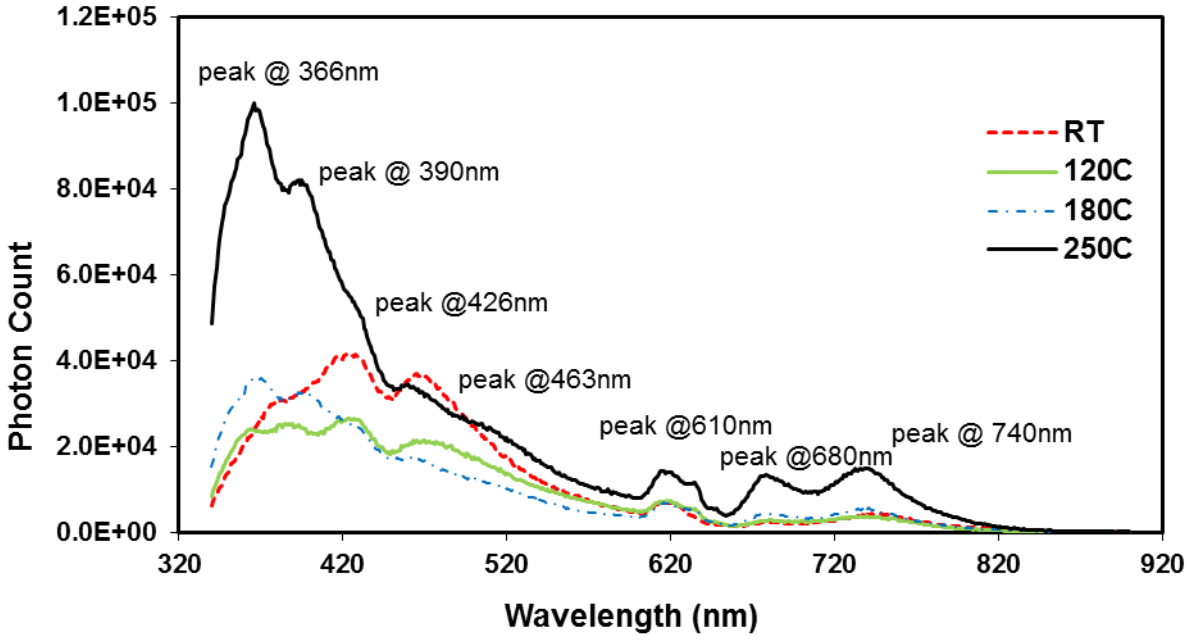

Figure 3-8. Room temperature photo luminescence spectra evolution of ZnO:Al film deposited at 150Wrf and 0.5 mTorr on glass substrate with different deposition temperatures in a logarithmic scale. Excitation wavelength is 310 nm. The emission peaks for sample prepared at substrate temperature of 2500C is depicted.

The effect of deposition temperature on photoluminescence of ZnO:Al samples prepared on glass substrate is even more drastic as depicted in Figure 3-8. The change in position of

emission peaks along with change in photoluminescence intensity is an indication that samples have gone through a structural change at higher deposition temperatures [70]. The I_{NBE}/I_{DLE} ratio for samples prepared on glass substrate at RT and 250°C is 0.003 and 2.95 respectively which is an indication of an improvement in crystalline quality. All of the samples, regardless of the substrate being glass or silicon, show a strong near band edge photoluminescence emission (NBE) at deposition temperatures above 120°C.

3-3. Summary

In this chapter the optimization of individual layer for the fabrication of ultra-thin film solar devices presented. Al-doped zinc oxide films have been deposited on glass substrates at various temperatures in a magnetron sputtering system modified for controlled, in-situ heating of the substrates. Operating at a low chamber pressure of 0.5mT gave reasonably high film deposition rates of 4-8 nm/min, and rendered the film resistivity minimally sensitive to variations in the RF power. Hall effect, four-point-probe, and UV-Vis spectrometry were used to study the resistivity, carrier concentration, mobility, and optical transmission of the films at different deposition temperatures. A very low resistivity of 2.94×10^{-4} Ω-cm was obtained with a highest deposition temperature of 250°C. Correlation between the optical transmission in the high wavelength range (>1000 nm) and carrier concentration has been obtained. X-ray diffraction and photoluminescence measurements were carried out to analyse the effect of Al doping and the structural changes in the films deposited at high temperature. The AZO films showed dominant peaks along (103) orientation compared to the undoped ZnO films where the (002) orientation was dominant. Undoped ZnO films showed better crystallinity than AZO. On the other hand, the XRD analysis also showed that the AZO films deposited at 250°C showed slight improvement in crystal quality over those deposited at RT. The evolution of near-band edge and deep level emission peaks as observed on the photoluminescence measurements also provided further evidence that the 250°C-deposited AZO films to have an improved crystal structure compared to the RT films. These results are useful in optimizing the AZO films in the design of advanced solar cells and optoelectronic devices.

Chapter

4

Semi-Transparent Nanocrystalline Silicon Ultra-Thin Film Device Development-II: Cell Design Configuration and Device Integration

This chapter presents development of semi-transparent nanocrystalline silicon (ncSi:H) film devices to be used as a platform for the integration of nanoplasmonic structures. New transparent nc-Si solar cell with p-i-n configuration is developed on glass substrates incorporating highly conductive aluminium doped zinc oxide (AZO) films as top and bottom electrodes.

4-1. Development of Semi-Transparent Nanocrystalline Silicon Thin Film Solar Cells

For the development of semi-transparent nanocrystalline silicon thin films RF-PECVD fabrication technique is used due to its advantages over other deposition methods. It is the most common deposition tool for "device quality" aSi:H/nc-Si:H both in laboratory and industry scales. In particular, low-temperature process, good deposition rate, and good optimization parameters makes PECVD a good candidate for nc-Si:H thin films development.

In this section the integration of semi-transparent nanocrystalline silicon thin film solar cells is demonstrated. Individual thin films (doped layers and absorber layer) were previously developed by E. Fathi [74] and L. Tian [75] at the CAPDS and in this work further optimization of window layer and absorber layer through device integration discussed.

4-1-1. Methods and Materials

4-1-1-1. Device Structure

Considering the semi-transparent functionality of the final device superstrate p-i-n thin film structure was used as the base device structure in full-penetration (FP) superstrate configuration (Figure 4-1). In general, for p-i-n structure p-layer will always be used as a window layer to avoid holes recombination in p-layer due to low mobility of hole carrier compared to electron mobility in a-Si:H and nc-Si:H. Also, p-doping normally required higher RF power to achieve good doping and to avoid damaging from high power plasma to lower layer superstrate structure is chosen since p-layer is the first layer deposited on glass substrate.

In addition, in FP configuration, light can be transmitted through the entire area of the cell while generating electricity unlike aperture semi-transparent configuration composed of rectangular grid fabricated by patterning technique.

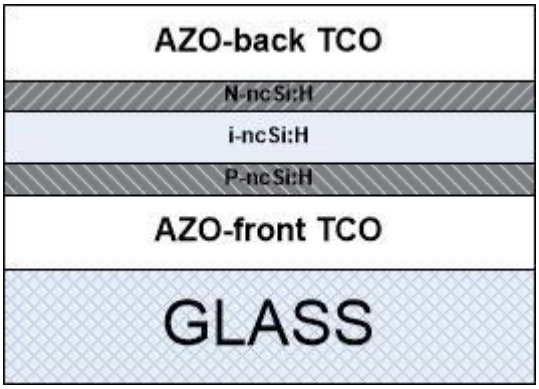

Figure 4-1. Schematic configuration of the semi-transparent superstrate p-i-n solar cell.

4-1-1-2. PECVD System

In RF-PECVD, silicon thin films are deposited by decomposition and surface reaction of a silicon bearing gas. A common parallel plate reactor developed by Trion Technology (Orion III) is used for deposition, the details of this tool is explained in Figure 4-2. It is a cluster tool comprised of a load lock and two PECVD chambers: one is an Inductive Coupled Plasma (ICP) and the other is a capacitive coupled parallel plate PECVD. The capacitive discharges excitation between two cylindrical electrodes by applying radio-frequency (RF) signal; gas is

thereby dissociated through the collision between the gas molecules (SiH_4, H_2) and the accelerated secondary electrons in the plasma. These dissociated gases create a mixture of radicals, ions, neutral atoms, molecules, and other highly excited species. Due to the mobility of electrons, the gas mixture becomes positively charged, and a potential drop zone, called sheath, is formed between the plasma and neighbouring objects. Radicals will be accelerated to the objects after diffusing to the edge of plasma, and start film growth.

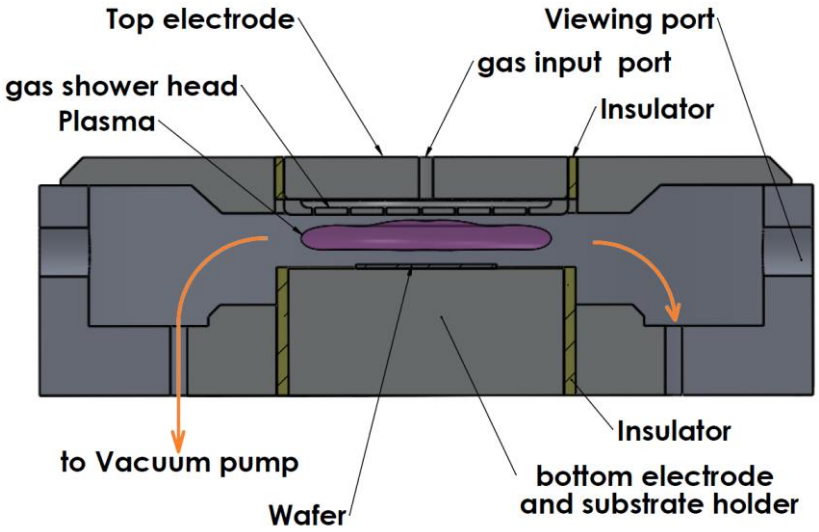

Figure 4-2. A schematic view of PECVD tool used for the deposition of different silicon thin films. The electrode separation is 37mm and the area of the electrode is 301.7 cm^2 and the bottom electrode is made of steel capable of heating up to around 450°C. All other part of chamber is made of Aluminium. The power supply consists of a 600Watt, 13.56MHz power source for top electrode and a 600Watt, 300KHz power supply for bottom electrodes. This configuration is called "Triode" by Trion Technology [76].

Device quality a-Si:H is normally deposited by SiH_4 gas between 200 to 250ºC, at the rate of 2-5Å/s. this temperature range provides a wide range of possible low cost substrates such as glass, stainless steel, and flexible plastic foils. Doping is attained by adding proper gases with source gas, usually diborane (B_2H_6) or pyrophoric trimethylboron (TMB) for p-type, phosphine (PH_3) for n type film. By controlling different gases, it is possible to deposit multi-layer structures throughout a continuous process. As well, film deposited by PECVD has good adhesion and uniformity.

4-1-1-3. Chamber Preparation

One of the limitations for this research work was the development of doped and intrinsic silicon thin films in a single chamber. In order to obtain good quality films with repeatability, a well-established chamber condition is required; therefore, before each film deposition, the chamber is cleaned and pre-deposited to a known and controlled condition.

After each doped thin film deposition, a chemical cleaning process was run, using 20% O_2 in CF_4 plasma, to etch the deposited film from the chamber walls and electrodes. It should be noted that CF_4 plasma can react with metal surfaces, and, in so doing, generate a yellowish coloured powder from within the chamber surface and vary the chamber's internal condition. To avoid this, the duration of cleaning was determined by considering the accumulative thickness of deposited film, and by etching a glass wafer coated with known thickness. Also physical surface cleaning was done between each 8-10 chemical cleaning. Every session of chemical cleaning will have some undesirable by-products: for example, residual CF_4 inside the chamber, or in the gas pipeline, which was applied to ensure the chamber is free of any by-product. The multi-step H_2 flush-vacuum procedure, followed by pre-deposition of amorphous silicon with H_2 plasma, was also done to passivate the chamber walls and electrode surfaces. A flow chart depicting chamber conditioning for each deposition is shown in Figure 4-3.

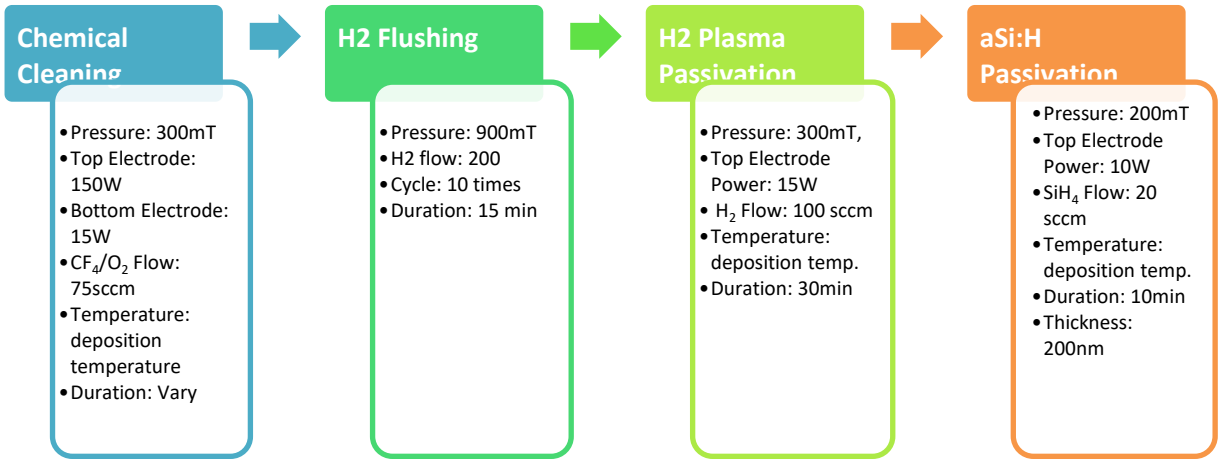

Figure 4-3. Flow-chart of chamber preparation steps

4-1-1-4. Characterization Methods

As schematic of fabricated cell structures showed in Figure 4-1, in order to assign the cells area, a shadow mask used for defining 3 different cells area, 1cm^2, 0.25cm^2, and 0.0625cm^2 as shown in Figure 4-4.

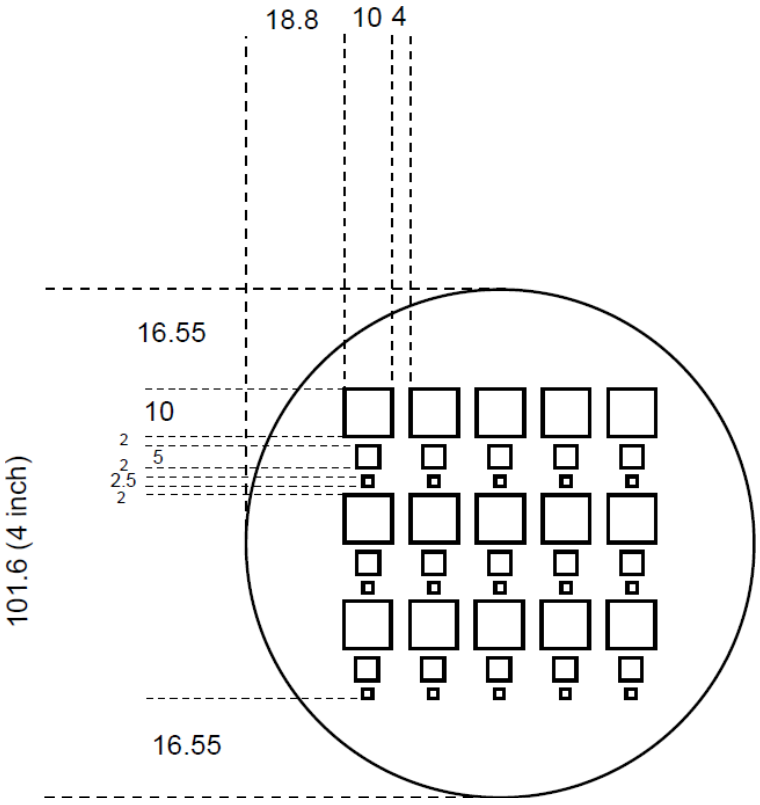

Figure 4-4. A 4inch shadow mask used to fabricate cells with different area.

For the back contact electrical connection, the p-i-n layers are removed through RIE by placing a square glass wafer to cover the front contact and surrounding silicon films. For fast measurement of the I-V characteristic, a custom Cell Readout Board (CRB) has been designed and fabricated by E. Fathi (Figure 4-5) [74].

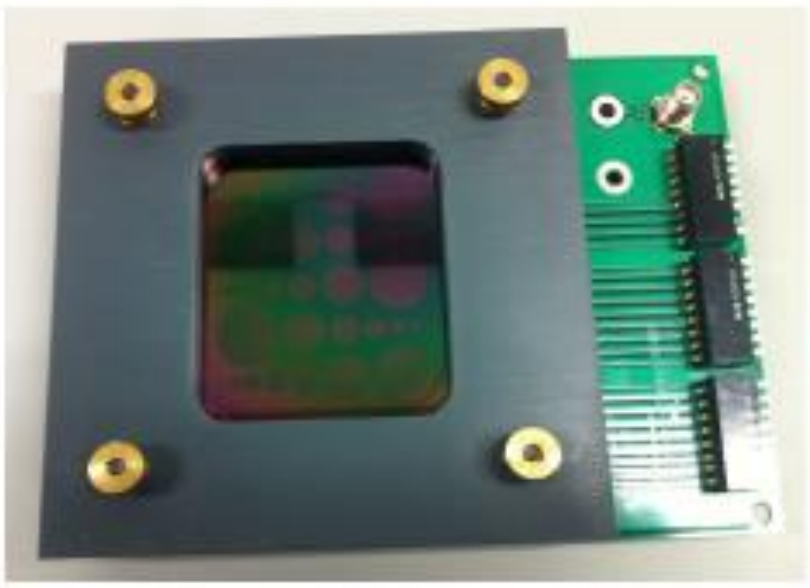

Figure 4-5. Fabricated Cell Readout Board, used for the EQE and I-V characteristic measurments.

4-1-2. Nanocrystalline Silicon Thin Films Development

The first step is to develop individual doped (n- and p- type) and intrinsic thin films. In this thesis, n-type µc-Si:H, p type µc-Si:H, and intrinsic protocrystalline aSi:H was developed based on previous work done by L. Tian [75] and E. Fathi at CAPDS with Trion III PECVD. In this section the initial thin film development is presented and in the next section, device optimization is discussed based on the integration of the developed layer.

4-1-2-1. N-type ncSi:H thin film development and optimization

Phosphone (PH_3) gas diluted in hydrogen to a 1% concentration is used as doping gas for n-doped nanocrystalline thin films. It has been shown that by attacking weak silicon bonds, high H_2 dilutions (~98-99%) rebuild the atomic structure and increase the crystalline percentage of silicon thin films. The first step for n-dope thin film development is to find the optimized doping gas ratio (R_n, B_2H_6-SiH_4 ratio). By measuring the crystallinity and conductivity of film, the optimum ratio will be investigated. Figure 4-6 shows the crystallinity and dark conductivity of n-type µcSi:H films as a function of R_n deposited on glass substrate, which was developed by E. Fathi and L. Tian [75]. The Raman measurement was used to calculate the crystallinity of

deposited thin films. It is clear that increasing R_n reduced crystallinity, a result attributable to the introduction of more defects.

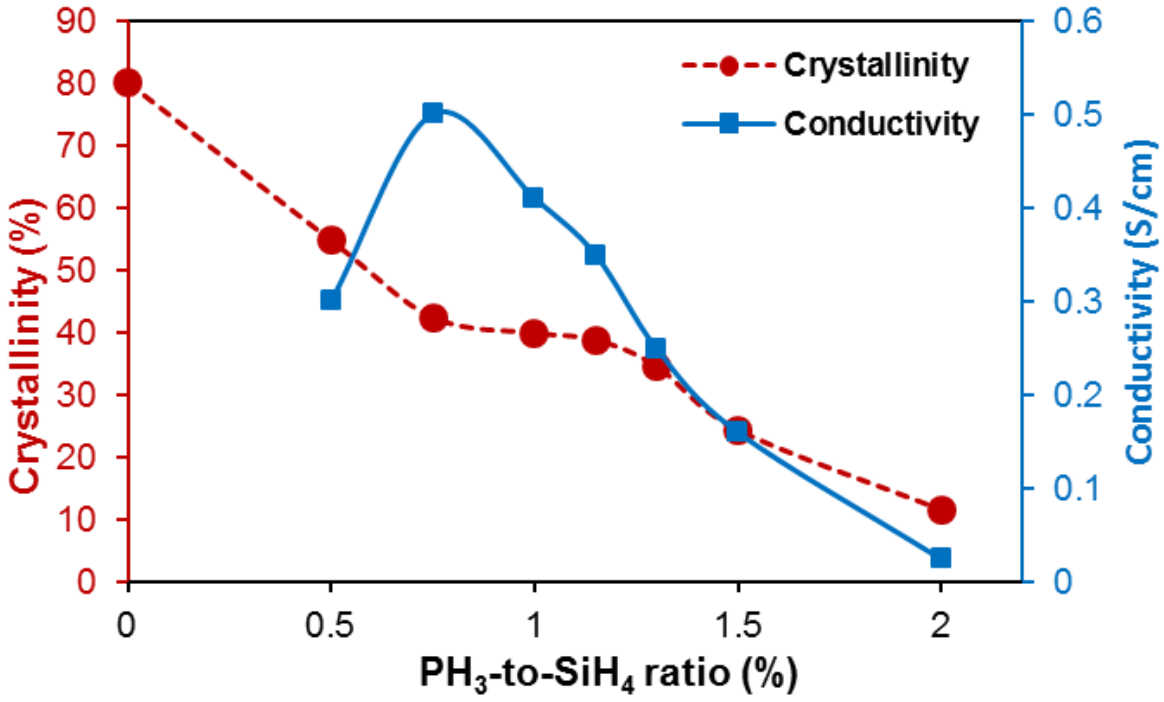

Figure 4-6. Dark conductivity and crystallinity of a 40nm μcSi:H as a function of R_n=PH_3/SiH_4 ratio.

The conductivity shows a maximum peak at the 0.6%<Rn<1%, with crystallinity at approximately 40%. With this data, n-doped μcSi:H was developed in the R_n range of 0.8%-1%. The deposition condition is summarized in the table below.

Table 4-1. n-type nanocrystalline silicon thin film deposition condition

Rn=PH_3/SiH_4 %	SiH4 Flow sccm	Power W	Pressure mT	Temperature ◦C
0.8-1	2	5	600	250-300

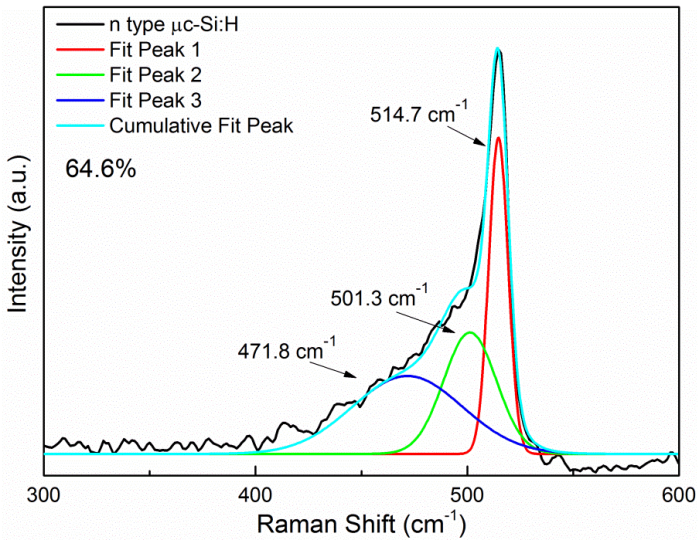

Figure 4-7. Raman of developed n-doped ncSi:H thin film with PH_3-to-SiH_4 ratio 1%, H_2 dilution 99% at 180°C [75].

4-1-2-2. p-type ncSi:H thin film development and optimization

There have been numerous studies to optimize p-doped nanocrystalline silicon thin films as a window layer with good conductivity and low defect density [77][78][79]. Boron-doped ncSi:H has an advantage over p-type aSi:H or aSiC:H alloy, on account of better conductivity and lower optical absorption in the visible range [74]. In general, boron-doped ncSi:H films have lower conductivity compared to phosphorous-doped nc-Si:H films, due to lower mobility of the minority carrier in p-doped ncSi:H.

In this research, pure silane SiH_4, along with diborane B_2H_6 diluted in H_2 to 1% concentration, were used as the gas source in RF PECVD. Guided by previous studies, the effect of H_2 concentration, B_2H_6/SiH_4 ratio, and pressure was investigated by L. Tian and E. Fathi at the CAPDS. Their results indicate that increasing the H_2 concentration from 98.9% to 99.5% has rising effect on dark conductivity for roughly 20%, and a reducing effect on deposition rate. It is commonly understood that H_2 flow has a passivation effect on weak bonds. Removing silicon dangling bonds increases the crystallinity of the structure, which, in turn, improves the conductivity while simultaneously reducing the time in deposition rate (Figure 4-8) [75].

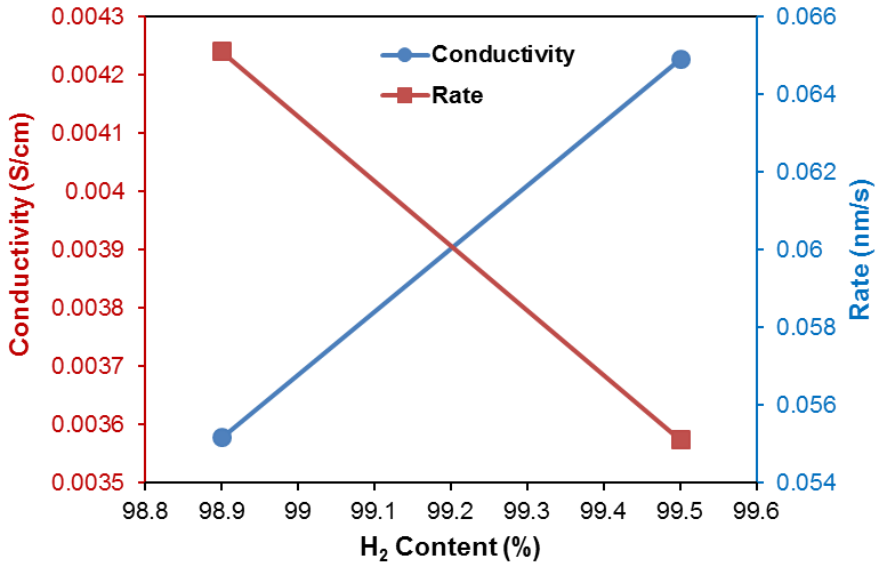

Figure 4-8. Effect of H_2 dilution on the conductiovity and deposition of diborane doped ncSi:H thin films. Deposition condition: SiH_4 flow rate 2sccm, B_2H_6 (1%H_2) 0.6sccm, pressure 300mT, and Temperature 180°C.

Also, in Figure 4-9, the effect of different B_2H_6/SiH_4 ratio showed that maximum conductivity is at the range of 0.055-0.065 S/cm for the 0.5-0.7% B_2H_6/SiH_4 gas ratio. Further increase of gas ratio caused a sharp decrease in conductivity. This is because heavily doping reduced crystallinity of film and widened the amorphous grain boundary, causing an increase in the mobility barrier for carrier. The effect of chamber pressure on film conductivity and deposition rate is indicated in Figure 4-10, for thin film deposited at the SiH_4 flow rate of 2sccm, and at the B_2H_6/SiH_4 ratio of 0.009, at 300mTorr chamber pressure and 180°C temperature. It is evident that chamber pressure has a great impact on conductivity. By increasing the chamber pressure, conductivity increases around 300-400mTorr, and then undergoes a sudden drop for approximately one or two orders of magnitudes.

The effect of chamber pressure is mainly ascribed to pressure dependent H_2 incorporation into growing film. At low pressure, the probability of collision between electrom-SiH_4 and electron-hydrogen would be low, causing the generation of atomic hydrogen to decrease. The quality of developed film is affected by low atomic hydrogen existence, since there would be less H_2 for the passivation of developed Si:H thin film. At high H_2 concentration, atomic hydrogen—rather than thin film passivation—becomes the precursor generation, enabling the growth of a porous, hydrogen-rich amorphous phase and reducing conductivity.

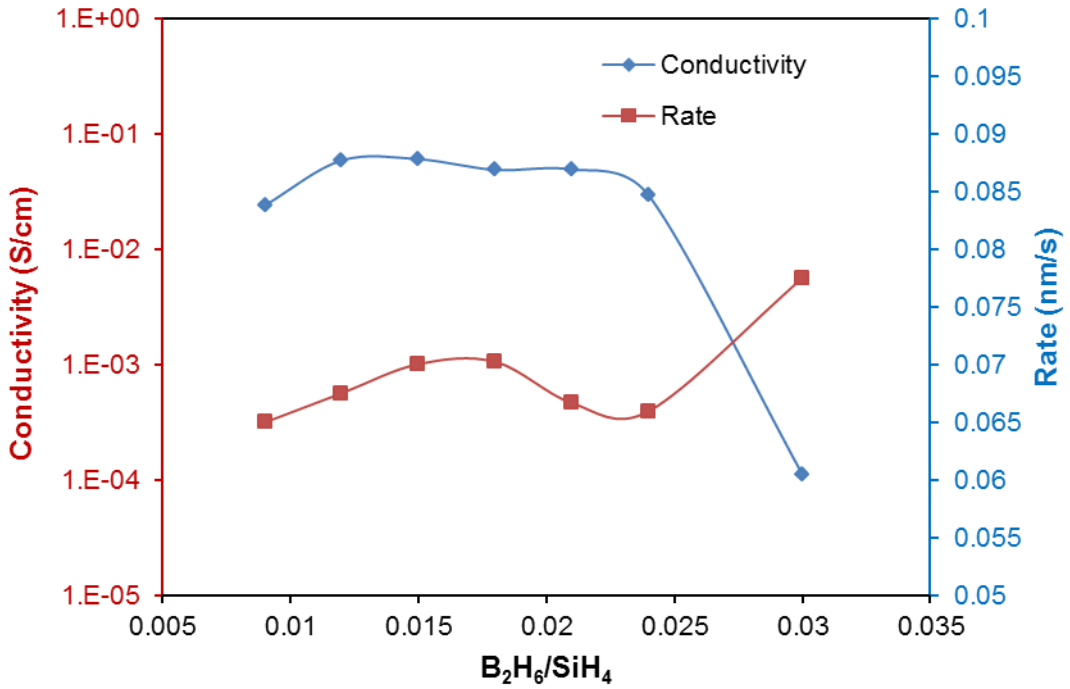

Figure 4-9. The effect of different B_2H_6/SiH_4 gas flow ratio on conductivity and deposition rate of diborane doped ncSi:H thin films, deposition condition: SiH_4 flow rate 2sccm, pressure 300mT, and Temperature 180°C.

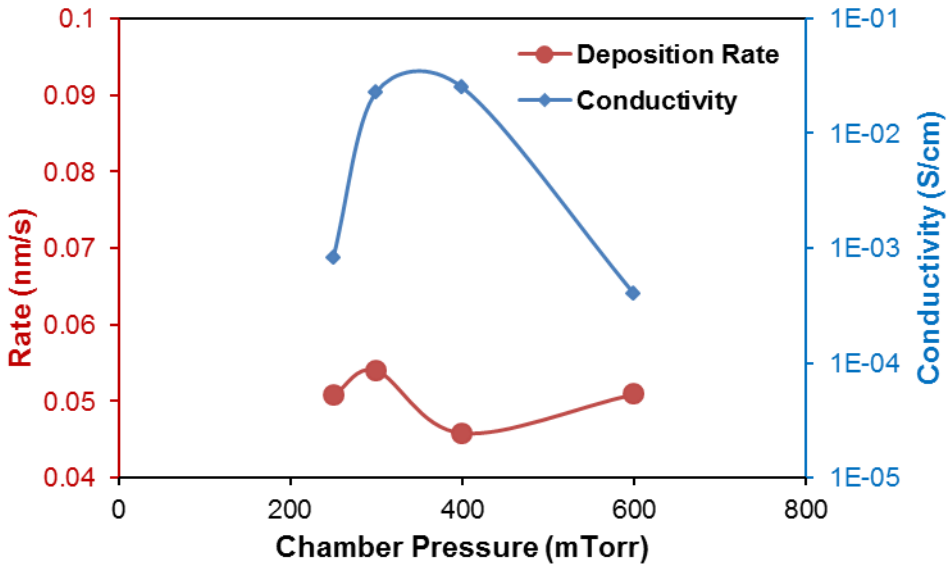

Figure 4-10. The effect of chamber conditions on the conductivity and deposition rate on p-type nc-Si:H.

The effect of power on deposition rate and electrical properties is shown in Figure 4-11. At high power, the deposition rate increases as the high radical densities increase with almost a linear dependency between power and deposition rate. Also, for favourable electrical

behaviour, there is a power window (55-65W) for good conductivity/crystallinity, as high power would normally decrease crystallinity by enhancing the amorphous phase deposition [75].

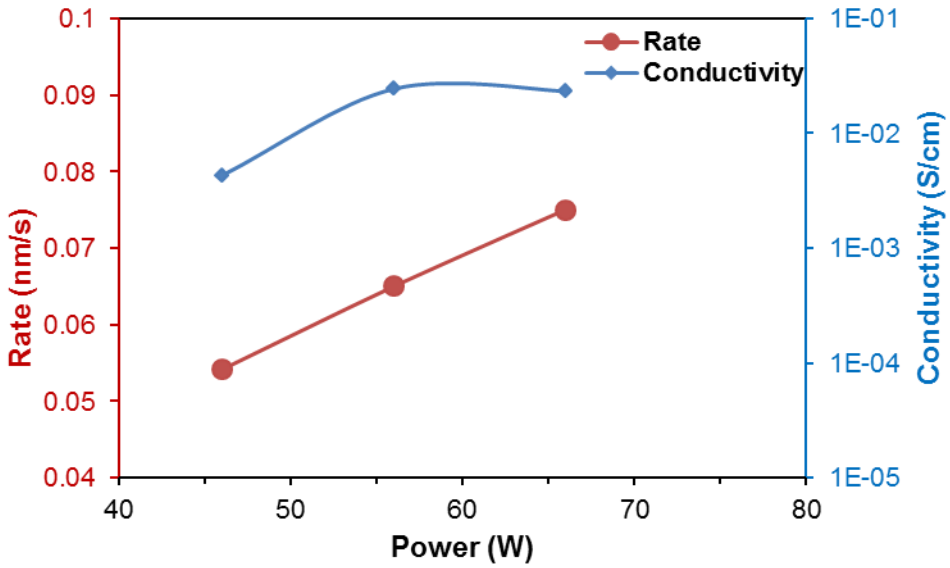

Figure 4-11. The effect of RF plasma power on the conductivity and deposition rate on p-type nc-Si:H film deposited at 300mTorr with SiH4=2sccm, B_2H_6/SiH_4=0.009, H2=400sccm, T=180°C.

4-1-2-3. Intrinsic undoped nanocrystalline thin film development

The deposition of high quality nanocrystalline silicon thin films is greatly impacted by changing hydrogen and silane flow rate [80]. Conventional a-Si:H, a-Si:H with intermediate orders (protocrystalline Si:H), mixed phase Si:H, nc-Si:H and mc-Si:H can be developed by varying the hydrogen dilution in the process gas [81][82][83]. Investigating the evolution of microstructure during deposition revealed that, at the first stage of depositing nc-Si:H, an initial amorphous incubation layer initially developed, followed by nucleation and growth of cone-like nanocrystalline clusters. By increasing film thickness, a phenomena known as nanocrystalline evolution happens, in which crystalline volume fraction and average grain size increases (Figure 4-12) [80].

In general, high crystalline volume fraction has the disadvantages of high density of micro-voids and cracks, causing ambient degradation due to impurity diffusion [80]. The key objective was to maintain a material structure that is close to the amorphous/nanocrystalline transition phase throughout sample thickness. This task was difficult, because its fulfillment

depended heavily on the control ability of the PECVD instrument. At low hydrogen dilution, a thick, amorphous incubation layer developed, and at high hydrogen dilution, a thick, high porous crystalline top layer emerged [80].

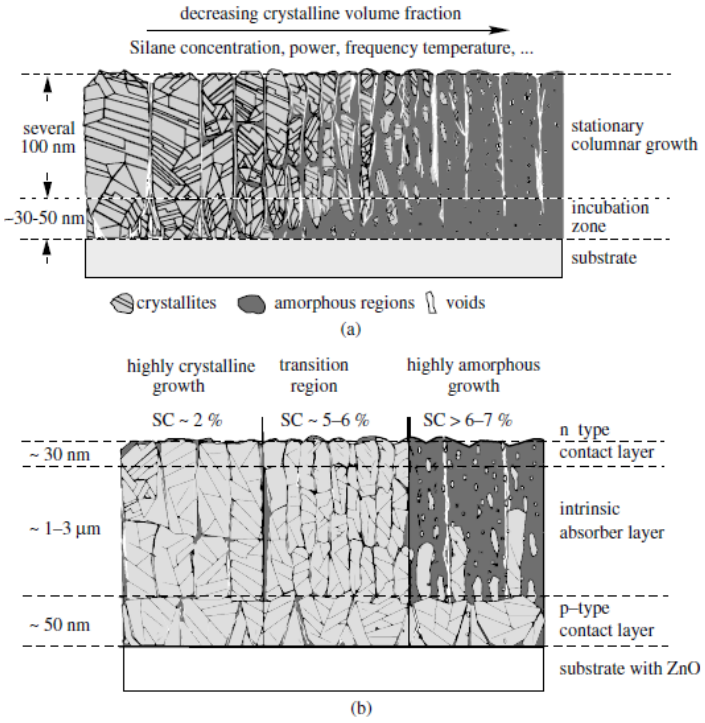

Figure 4-12. (a) Schematic view of the structure of µc-Si:H ranging from highly crystalline on the left to amorphous on the right in a cross section view on a foreign substrate like e.g. glass. For details see text (By courtesy of Forschungszentrum Julich); (b) Schematic cross section view of the structure of µc-Si:H solar cells with the i-layer grown at different silane concentrations on a highly crystalline p-type contact layer. The important local epitaxial growth of the i-layer on the p-layer, thereby avoiding the amorphous incubation layer is indicated. For details see text (By courtesy of C. Scholten et al., Forschungszentrum Julich) [80].

To maintain the quality of the i-layer within the desired regime (as explained above), a hydrogen dilution profiling technique was employed as a suppressant for nanocrystalline evolution phenomena [82]. It was also observed that the transition phase, from aSi:H to mc-Si:H, shows that the optimum absorbed layer structure achieved by a hydrogen dilution was close to the amorphous/nanocrystalline transition. E. Fathi et al. have recently optimized the formation of undoped protocrystalline silicon by measuring the $\sigma_{photo}/\sigma_{dark}$ conductivity ratio at different $R=H_2/SiH_4$ (Figure 4-13). Findings show that the H_2/SiH_4 ratio zone of 4.25-4.75 photosensitivity (has a maximum performance similar to the state-of-the-art absorber layer requirement ($>10^5$) [74]. Table 4-2 presents deposition conditions used for the development of the i-layer.

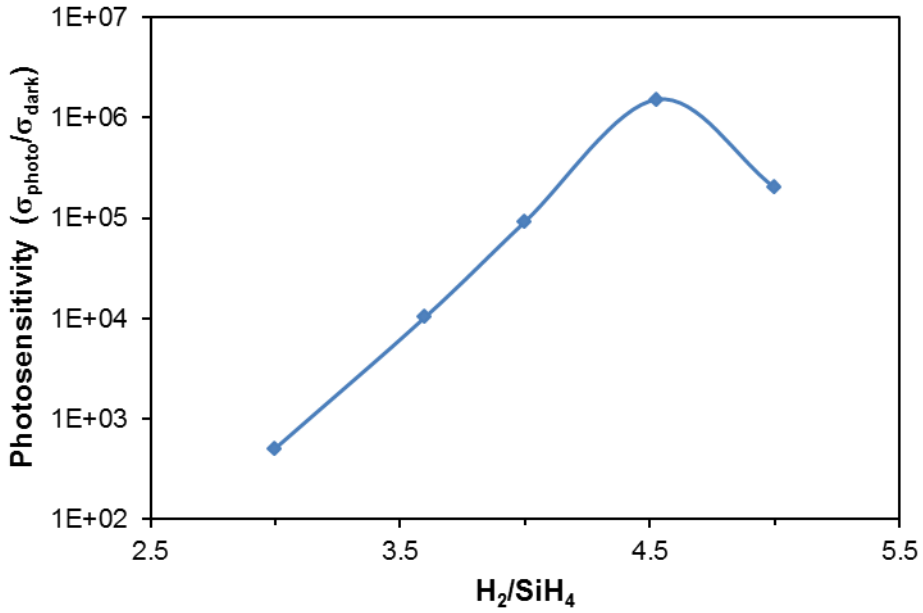

Figure 4-13. The effect of H_2/SiH_4 ratio on photosensitivity (the ratio of photoconductivity to darkconductivity) of Si:H thin film [74].

Table 4-2. Intrinsic undoped nanocrystalline silicon thin film deposition condition

$Rn=H_2/SiH_4$	SiH_4 Flow sccm	Power W	Pressure mT	Temperature ◦C
4.5-5	4	2-5	600-700	250-300

4-2. Introduction: cell design configuration and device integration

In the device configuration for ultra-thin film devices, the p-i-n structure was chosen as the device architect, with p-layer as the window layer. The main reason for this selection is that the majority of the absorption and electron-hole pair generation will occur near the absorber layer (i-layer) and window layer. For the effective charge collection, the layer with the least major carrier mobility should be deemed a window layer to avoid loss due to recombination. Therefore, the p-layer with low hole mobility compared to the n-layer with higher electron mobility first placed in the direction of incident light.

For device configuration, two well-known designs for substrate and superstrate configurations were selected, with glass to be used as the substrate (See Figure 4-14).

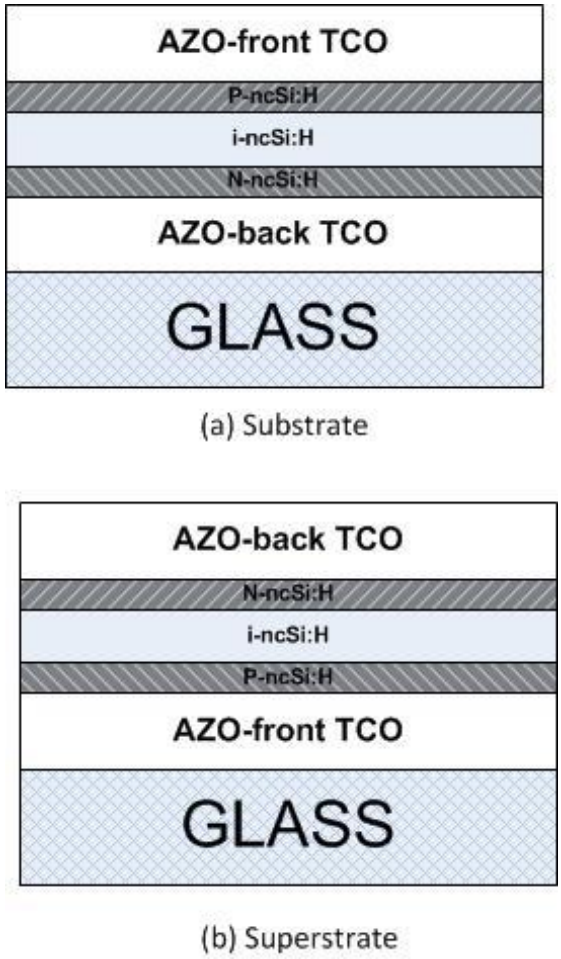

Figure 4-14. Schematic outline of the device configuration for ultra-thin film solar cell: a) substrate configuration, b) superstrate configuration.

One key parameter in cell design is defining the thickness of the layers (d_i, d_p, and d_n). The most profound effect is the i-layer thickness. The collection of carriers in the p-i-n solar cells depends on the strength of the electric field in the i-layer, spurring the SWE effect as explained in section 3-1. A thinner i-layer has a higher electric field, which reduces the influence of additional metastable defects on carrier transport.

For doped layer thickness (d_p and d_n), the condition is complicated. To better understand the effect of thickness, it is important to investigate the electric field distribution inside a p-i-n solar cell.

As shown in Figure 4-15, a space charge region in the p-layer and n-layer, due to the depletion of free carrier (p_f and n_f), is created. An internal electric field is then created in the i-layer. In addition, assuming the space charge density inside the i-layer is zero, the resulting electric field

(E_i) will remain largely constant across the i-layer. The magnitude of E_i is proportional to V_{bi}/d_i, as shown in Figure 4-16 [80].

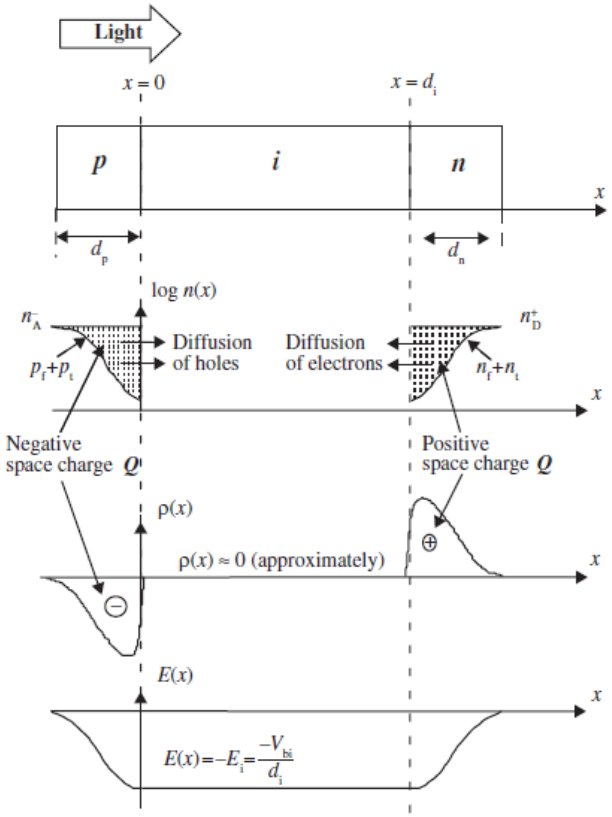

Figure 4-15. Space charge region and internal electric field distribution (E(x)) within a p-i-n solar cell [80].

The configurations in Figure 4-15 and Figure 4-16 reveal that the thickness of doped layer, dp and d_n, cannot be reduced below certain minimal values, since the intensity of space charge density is dependent on the doped region thickness. This issue is more critical for the p-layer, as a "window-layer", because the window layer thickness must be kept at the lowest minimum possible, in order to reduce waste absorption [80].

Therefore, if a minimal p-layer thickness is below the internal electric field, Voc will be reduced. When decreasing the i-layer thickness, the p-layer thickness should be increased proportionally to compensate for Voc reduction. To more effectively determine the doped layers thickness experiments is used to find required thickness.

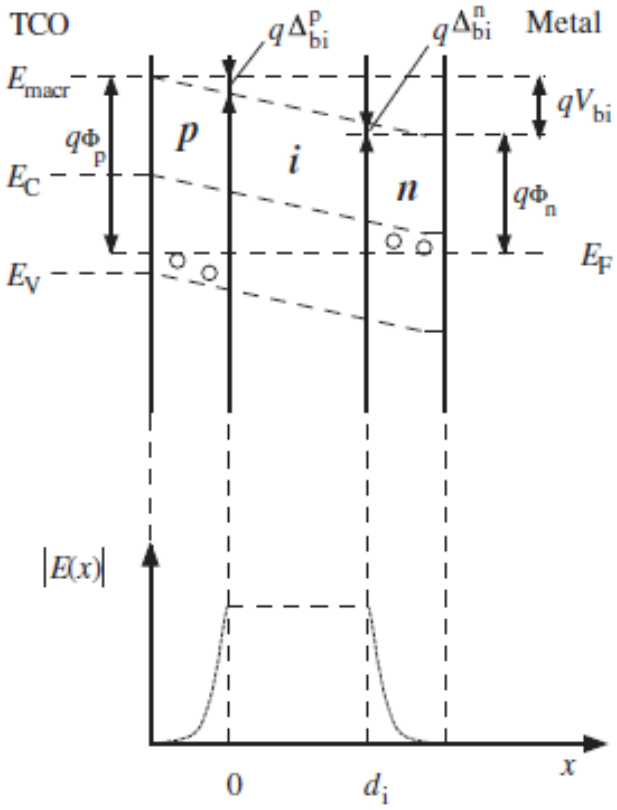

Figure 4-16. Band diagram for the ideal p-i-n solar cells [80].

The internal electric field E(x) in the i-layer will be deformed and reduced by additional space charge, from the following sources [80]:

1. Ionized atoms, due to cross-contamination from dopant atoms (mainly from the doped layer deposited before the i-layer (i.e., from boron atoms in the case of p–i–n-cells, or from phosphorus atoms in the case of n–i–p-cells). For these reasons, one must avoid cross-contamination and use either multichamber deposition systems or special chamber cleaning processes for each layer deposition.
2. Ionized atoms from impurities acting as dopants, especially from oxygen and nitrogen contamination.
3. Trapped carriers in band tails, especially trapped holes in the valence band tail.
4. Ionized dangling bonds.

4-3. Device integration optimization

In the first step, we chose superstrate device configuration for optimization. In the previous chapter, the developed n-ncSi:H layer was shown to have the best electric performance; hence, the

n-layer deposition did not change. Optimization was mainly focused on p-layer and n-layer thickness and p-layer deposition condition. For the i-layer, the deposition parameter was chosen based on the performance of the individual layer section 4-1-2-3.

For this purpose, at the first stage, different samples were prepared with p- and n-layers at different thicknesses (15, 20, and 25nm). The effect of different p-layer deposition parameters, on account of pressure (120,150, 350, 400 mT) and power (40, 45, 60), was investigated as well. The flowchart for device fabrication is illustrated in figure 4-17, and Table 4-3 summarizes the I-V performance of the developed devices.

The first step investigated the effect of n- and p-layer thicknesses and p-layer deposition conditions on the performance of the devices. For all of the deposited devices, constant i-layer conditions and thickness were chosen as recorded in Table 4-3.

One important result, from the first step of fabrication, conveyed a higher deposition pressure at which the best p-layer performance recorded (350mT and 400mT). The general performance of the devices is accordingly lower when compared to low pressure deposition. The most distinguished parameter was a lower fill factor at higher pressure.

Regarding the optimum p-layer thickness for the 150nm absorber i-layer, the best performance was achieved for 20nm p-layer thickness, specifically at low pressure. By increasing the p-layer deposition pressure, p-layer thickness should be increased to achieve sufficient build for maximum open circuit voltage. However, the thicker layer has a negative effect on the short circuit current, which, at 400mT, as shown in Table 4-3 and Figure 4-18, increased to a maximum of 25nm before decreasing. This change is accomplished by increasing the thickness from 20nm to 30 nm. One important parameter is the effect of pressure on the fill factor (FF). It is clear that by shifting the deposition pressure to a higher pressure, the fill factor decreases significantly (Table 4-3).

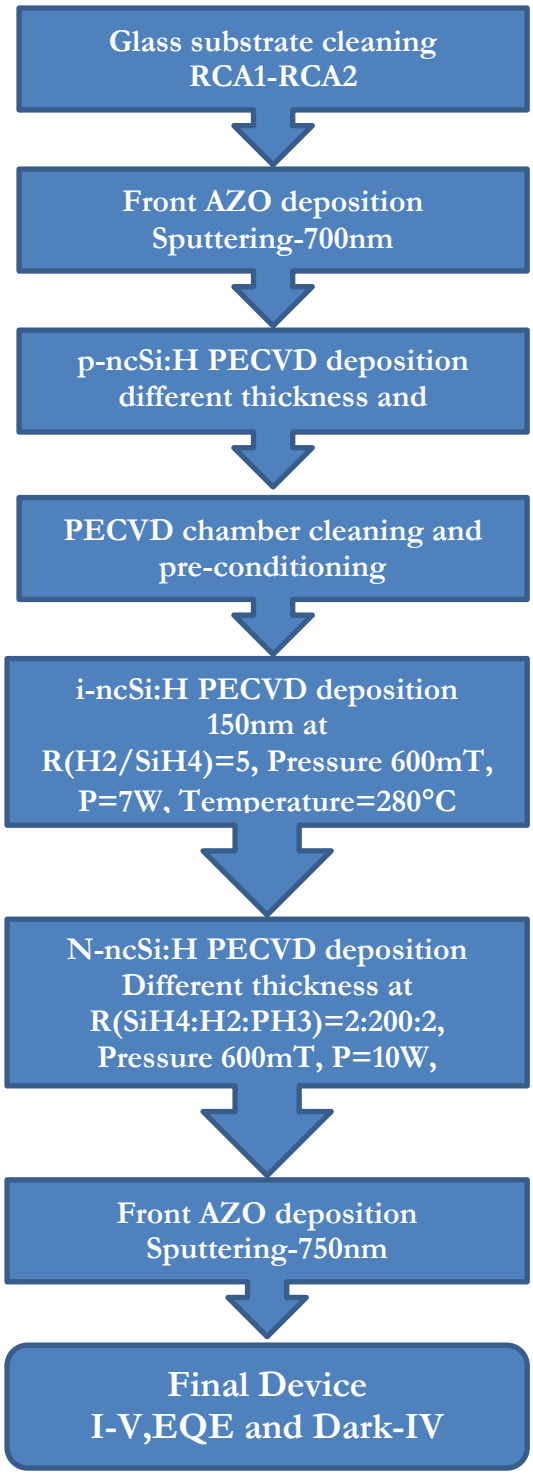

Figure 4-17. Flow chart of different steps for device fabrication.

Table 4-3. Depostion condition for developed samples with acceptable results and their I-V characteristics.

Samples			S1	S2	S3	S4	S5	S6	S7	S8	S9	S10
p-ncSi:H	Pressure	mT	125	150	150	125	125	150	350	400	400	400
	Power	W	40	40	40	45	45	45	60	50	60	60
	Gas Ratio	SiH_4:H_2:B_2H_6	2:300:14	2:300:14	2:300:14	2:300:14	2:300:14	2:300:14	2:400:14	2:400:14	2:400:14	2:400:14
	Temperature	°C	280	280	280	280	280	280	280	280	300	300
	Thickness	nm	15	20	25	20	15	20	25	30	25	20
i-ncSi:H	Pressure	mT	600	900	600	600	600	600	900	600	600	600
	Power	W	7	7	7	7	7	7	7	7	7	7
	Gas Ratio	SiH_4:H_2	3:15	3:15	3:15	3:15	3:15	4:20	5:25	3:15	5:30	4:18
	Temperature	°C	300	300	300	300	300	300	300	300	300	300
	Thickness	nm	150	150	150	150	150	150	150	150	150	180
n-ncSi:H	Pressure	mT	600	600	600	600	600	600	600	600	600	600
	Power	W	10	10	10	10	10	10	10	10	10	10
	Gas Ratio	SiH_4:H_2:PH_3	2:200:20	2:200:20	2:200:20	2:200:20	2:200:20	2:200:20	2:200:20	2:200:20	2:200:20	2:200:20
	Temperature	°C	300	300	300	300	s300	300	300	300	300	300
	Thickness	nm	15	20	40	35	35	35	35	40	35	35
Voc		mV	577	721	712	540	595	656	703	717	721	751
Jsc		mA/cm^2	13.5	11.44	9.66	12.14	13.7	11.68	8.24	8.66	10.62	8.48
Efficiency		%	3.4	3.02	2.72	2.8	3.26	3.3	1.4	2.24	2.62	1.26
FF		-	43.7	36.6	39.5	42.8	40.1	43	24.2	35.7	34.3	19.8
R_{sh}		Ω	1000	1000	1200	1000	830	1500	740	1600	720	270
Voc Slope		-	110	200	200	130	120	130	260	210	170	280

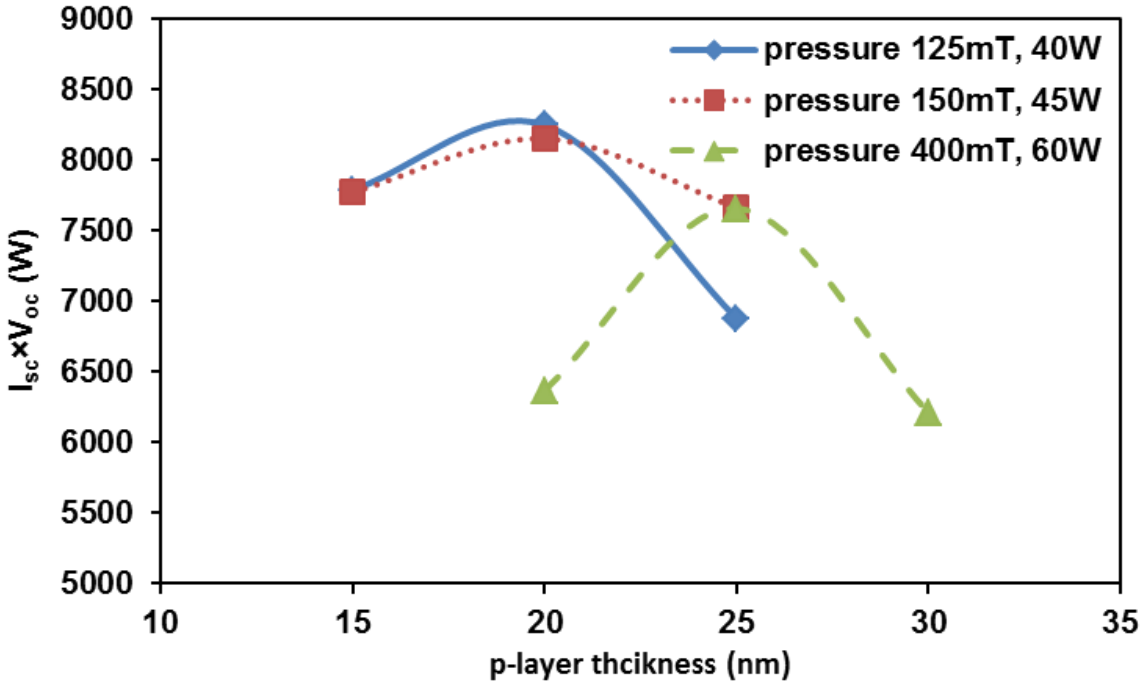

Figure 4-18. P-layer thickness effect at different deposition condition on the performance of device.

The value of fill factor is the most sensitive experimental indication of the quality of the solar cell and it shall be considered in addition to V_{oc} to identify the quality of the solar cell. Some common problems associated to low fill factor are [80][82]:

1. Low quality i-layer leads to weak charge collection;
2. p/i and i/n layers interfaces; mostly affect the Voc and external quantum efficiency (EQE) of the cell;
3. Series resistance due to low quality of the contact;
4. In adequate shunt resistance due to crack and structuring;
5. Leakge paths existence and bad diode quality.

The results in section 4-1-2-2. demonstrate that increasing the deposition temperature affects the p/i interface and possibly the recombination and collection at the interface. As expressed schematically in Figure 4-19, the density of dangling bonds at p/i interface are higher due to cross-contamination from dopant atoms diffused from p-layer to i-layer during the fabrication process [78]. Additionally, it is evident that the initial section of i-layer in contact with the p-layer will have positively charged dangling bonds, since the density of free holes (p_f) is considerably higher than the density of free

electrons (n_f). Similarly, at the interface between the i-layer and n-layer, there would be negatively charged dangling bonds ($n_f >> p_f$).

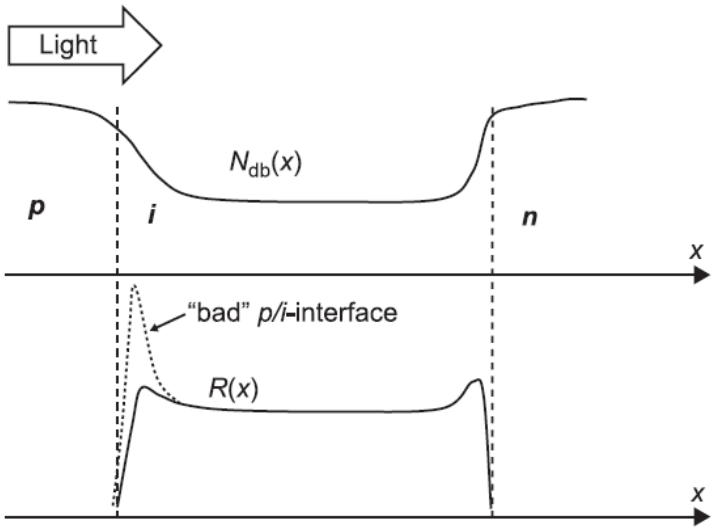

Figure 4-19. Schematic representation of p/i interface recombination due to the presence of excess dangling bond [83].

At higher pressure, one important phenomenon during fabrication entails part of the i-layer. Deposited first, it is usually contaminated by the dopant (boron) in the underlying p-type layer (so-called boron tailing), owing to etching of the underlying p-type layer by hydrogen plasma, and the release of a substantial quantity of boron atoms which interrupt the deposition of the i-layer's initial part. In addition, single chamber deposition intensifies the issue by contaminating all of the deposition chambers. With H_2B_6 as the boron carrier gas, the phenomenon of boron tailing would be even stronger. This problem is relevant to the i-layer/n-layer interface as well, since, during subsequent deposition of the n-type layer, the directly underlying part of the i-layer is somewhat affected by plasma, which then contains phosphorus (known as phosphorus back-diffusion) [84].

The existence of atomic hydrogen in the deposition plasma, along with the initial growth phase in the deposition plasma and the influence of impurities like oxygen, retain considerable influence over nanocrystalline silicon solar cells [85]. Oxygen has a dual effect in nc-Si:H: it forms donor states in the nc-Si:H, which, in turn, causes higher conductivity and decreases absorption. (It must be noted that, despite this awareness, the microscopic doping mechanism is not yet formally understood [86]).

In order to characterize the recombination mechanism in the prepared samples, dark I-V measurement was used. An ideal solar cells follows the typical diode characteristics as follow:

$$I = I_0\left(exp\left(\frac{qV}{nKT}\right) - 1\right) \qquad (4\text{-}1)$$

where, I_0 is the reverse saturation current for ideal diode, q the unit charge, T the measurement temperature, K the Boltzmann constant, and n the diode ideality factor. Figure 4-20 shows a dark I-V curve of two samples prepared at low pressure (150mT-40W) and high pressure (400mT-50W). In the dark I-V characteristic curve, the first region, 0V<V<0.4V, is dominated by parallel or shunt resistance, since there is a linear relationship between current density and electric field [87]. From the second region, 0.4V<V<0.8V, the diode factor n and the reverse saturation current, I_0, are evaluated based on equation (4-1).

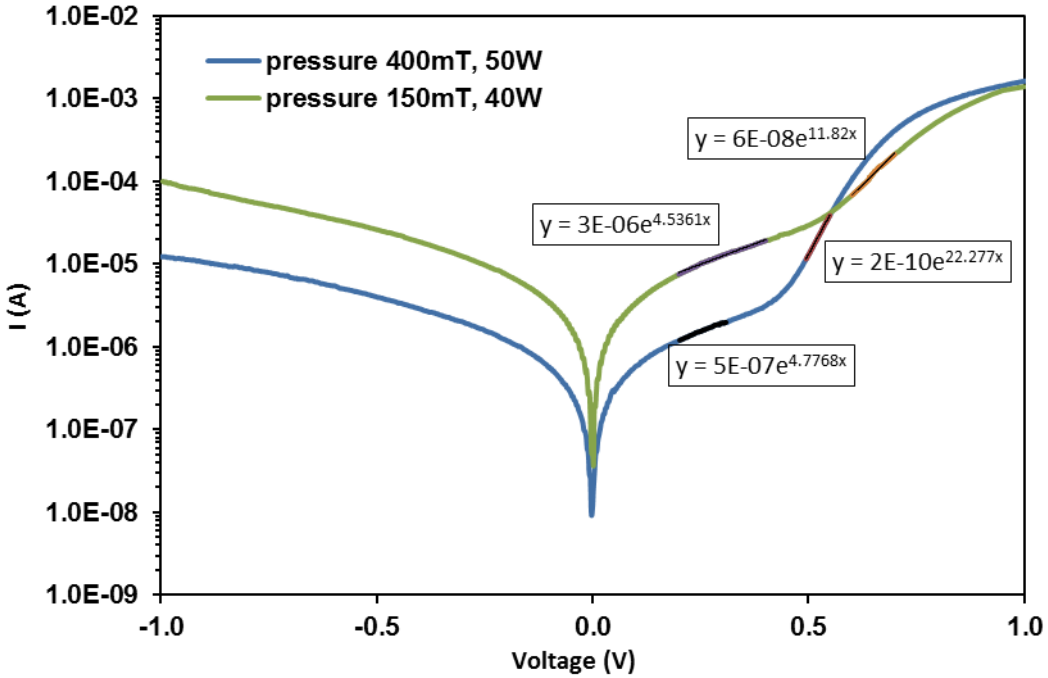

Figure 4-20. Dark I-V characteristics of samples prepared at 400mT-50W and 150mT-40W

The last part of the curve shows the beginning of the current saturation, caused mainly by AZO series resistivity and the space charge limited current effect. It is evident that both samples had a high shunt current density or interface recombination current at the low voltage region. Additionally, at the higher voltage region and low pressure, the series resistivity is slightly higher when compared to high pressure deposition, although both samples have identical open circuit

voltage near 720mV. The double diode model is the one that would normally be applicable when recombination at the interface is dominant:

$$I = I_{01}e^{\left(\frac{q}{KT}(V-IR_s)\right)} + I_{02}e^{\left(\frac{q}{2KT}(V-IR_s)\right)} + \frac{V-IR_s}{R_{shunt}} \qquad (4\text{-}2)$$

By fitting the data of all prepared sample to the diode characteristics, reverse saturation current, and ideality factor associated to the shunt resistivity and series resistivity calculated, as listed in

Table 4-4.

Table 4-4. The dark I-V fitting parameters of the prepared samples.

Sample no.	I_{01} (A/cm_2)	I_{02} (A/cm_2)	n_1	n_2
S8	3×10^{-8}	6×10^{-11}	5.01	1.69
S7	2×10^{-7}	7×10^{-10}	3.78	1.33
S6	3×10^{-6}	6×10^{-8}	8.5	3.27
S1	2×10^{-8}	7×10^{-11}	6.59	1.21
S3	2×10^{-8}	3×10^{-11}	6.59	1.35
S18	5×10^{-7}	2×10^{-10}	8.1	1.74
S17	4×10^{-7}	7×10^{-9}	7.1	2.55

One can see that the diode quality factors at low voltage, associated with shunt resistivity, are identical for most of the samples. However, reverse saturation current was different, indicating the existence of different recombination rates.

Further investigation of dark I-V fitting parameters on

Table 4-4 reveals that at lower pressure, reverse saturation current is lower, but shunt resistivity is almost identical for all samples. Series resistivity is different, as for samples at higher pressure and voltage with which smaller series resistance is observed. Shunt current in thin-film silicon solar cells can originate from various fabrication problems:

1. Particles may be deposited on the substrates or on the growing layers because of either a dusty environment or the formation of powder during the deposition itself (due to plasma polymerization (i.e., chemical reactions in the gas phase); after the particle falls off, a pinhole remains and a short-circuit will be formed when the final contact layer is deposited and makes contact to the conducting substrate through the pinhole.
2. Non-uniformities distributed across the surface.

3. Cracks may develop during the growth of the nanocrystalline silicon layer when a rough substrate is used and precautionary measures are not taken.

Considering ultra-thin film thickness for the absorber layer (150nm), it is known that the performance of thin-film solar cells with the thin absorber layer is mainly dominated by the p/i and i/n interface [85].

Figure 4-21 summarizes the external quantum efficiencies (EQE) of prepared samples. As expected from dark I-V measurements, all samples with the p-layers prepared at high pressure have lower EQE. In addition, EQE results reveal that the efficiency of absorption at lower wavelength (400-600) is dominant at lower pressure for the p-layer.

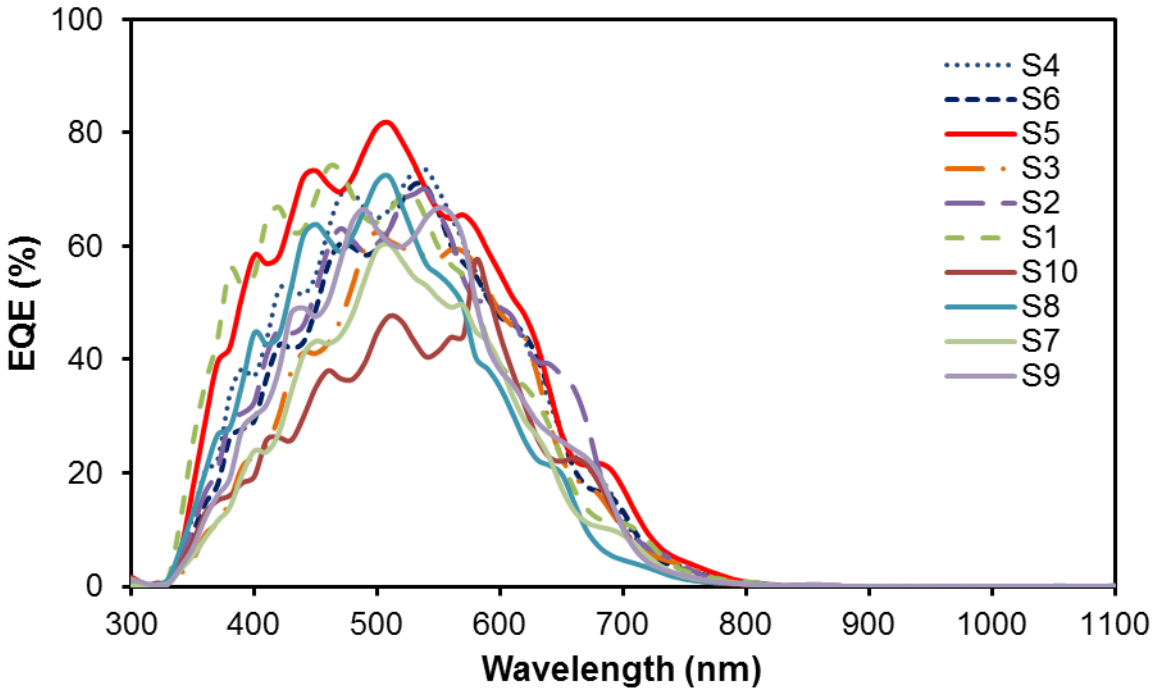

Figure 4-21. External quantum efficiency spectra of prepared samples.

One indication of p/i interface quality is the absorption at blue light observed in the EQE measurement. The EQE results shows that at lower p-layer pressure the p/i interface has the best performance due to higher blue light absorption.

4-3-1. Interface effect: AZO/p-layer, p-layer/i-layer, i-layer/n-layer, n-layer/AZO

In this section, an extended investigation is executed to elaborate more on the performance characteristic of prepared devices.

4-3-1-1. AZO/P-layer and n-layer/AZO interface

There are 2 approaches to investigate the AZO and doped layer interfaces. One can be done through band diagram investigation. The other approach is the investigation of deposition conditions, specifically H_2 plasma, on the interface properties. It is recognized that atomic hydrogen has a strong influence on ZnO and Al:ZnO surfaces. The most prominent effect of hydrogen plasma on Al:ZnO is the reduction of the materials [88][89][90].

Given the work function of the p-layer (near 5eV), as shown in Figure 4-22, the work function of TCO must be above 5eV to create an appropriate barrier for reducing the amount of recombination at the TCO/p-layer interface. For Al:ZnO, the work function is approximately 4.2-4.6eV, lower than the p-layer, causing an increased barrier potential to occur at the front interface and an obstruction in carrier movements, thus lowering the fill factor [90].

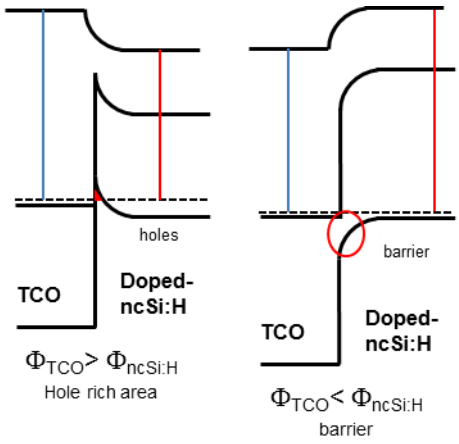

Figure 4-22. Schematic band diagram AZO as TCO/p-layer aSi:H.

One solution for this purpose is to lower the work function of p-layer, which can be done by inserting a highly conductive layer between AZO and p-layer. To achieve this, 2 approaches are

possible: 1) inserting highly doped p-layer (+p-layer), or 2) inserting the n-layer between AZO and p-layer with highly conductive properties with a lower work function layer (Figure 4-23).

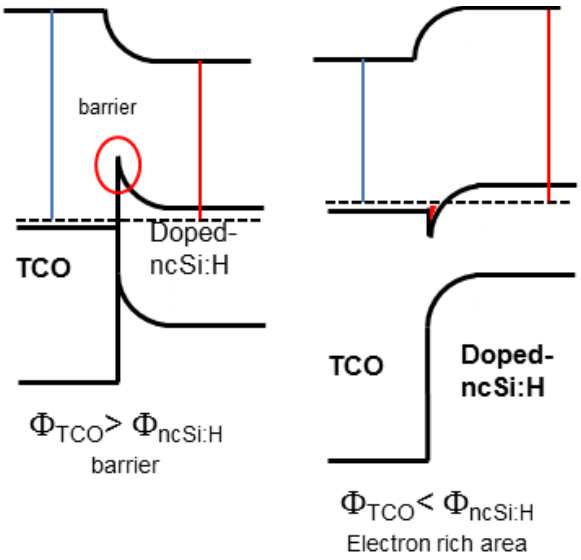

Figure 4-23. Schematic band diagram of AZO as TCO /n-layer aSi:H.

The already developed n-type ncSi:H thin film is a perfect candidate for option 2, and highly doped p-type ncSi:H another candidate for option 1. Table 4-5 summarizes three different buffer layers as a solution for AZO/p-layer interface recombination: AP1 is selected as a highly doped p-type layer; AP2 is selected as a n-type buffer layer; and AP3 is chosen as nanocrystalline silicon layer with high hydrogen plasma for higher bandgap.

Table 4-5. Proposed buffer layer thin film for AZO-P-layer interface

Samples		**AP1**	**AP2**	**AP3**	**AP4**
Pressure	**mT**	600	600	600	600
Power	**W**	10	10	10	10
Gas Ratio		SiH4:H2 2:200	SiH4:H2:H2B6 2:200:20	SiH4:H2:PH3 2:200:5	SiH4:H2:PH3 2:200:10
Temperature	**°C**	280	280	280	280

4-3-1-2. p-layer/i-layer and i-layer/n-layer interfaces

The band offsets at the p/i-layer, by preventing photo generated carriers in valance band (holes) moving to the p-layer from absorber layer, contributes to the observation of a weak device performance, and specifically an S shape like I-V curve behaviour under illumination, as shown in Figure 4-24 in sample S5.

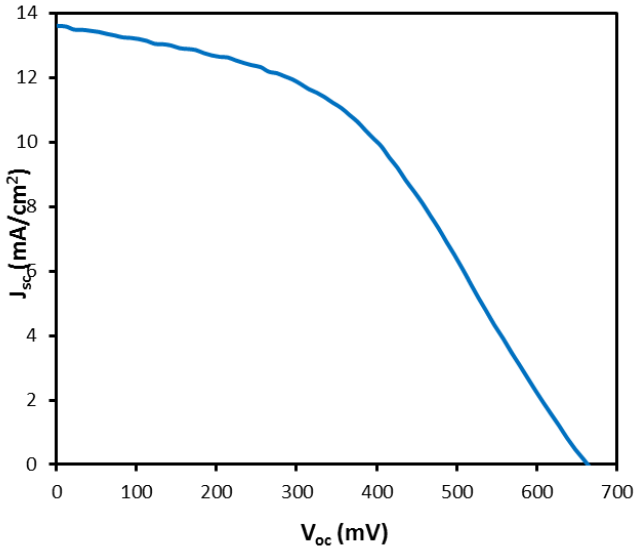

Figure 4-24. I-V curve of sample S5.

Vlahos et al. showed in their study that the recombination at the i/p interface is affected by a) defect density at the interface, b) the p/i-layer interface band gap, c)the p/i-layer alignment between p and i-layer, and d) the built-in potential, V_{bi} [91]. V_{bi} is not a good option since its determination is complicated. The efficiency of p-layer doping and p-i-layer alignment affecting V_{bi}, which these 2 effect are against each other.

Various recommendations have been made to solve this issue. The most well-known solution involves using a wide-band gap p-layer such as nc-SiC:H, which, due to the lack of CH_4 supply in the CAPDS lab, is not viable. It is suggested that having a buffer layer with a higher mobility gap than the mobility gap of the i-layer in the p/i-layer interface will improve the V_{oc} of the solar cell, since the V_{oc} is proportional to the mobility gap (improving item 4). Considering the available gas supply at PECVD, the best solution entails the insertion of an amorphous silicon buffer layer with a wider band gap. By controlling the H_2/SiH_4 gas ratio, the band gap of

deposited layer changes and the lower gas ratio, in turn, shows a higher band gap close to the amorphous silicon band gap.

The other advantage of using a buffer ncSi:H layer with lower H_2/SiH_4 gas ratio is the effect of hydrogen plasma and its effect on etching the p-dopant (boron) into the absorber layer. By using a lower gas ratio at the interface the effect of hydrogen plasma will be reduced and the quality of interface will increase. Lower etching of underlying p-layer by atomic hydrogen reduces the band tailing at the p/i-layer interface. Finally, the larger band gap and narrower band tails in the p/i-layer interface region would lower electron hole recombination and improve the fill factor and V_{oc}. The same conditions for band offset exist in i-layer/n interfaces. However, in this case, since the n-type nc-Si:H layer developed with high hydrogen plasma, band tailing is generally narrower and recombination at the interface is thereby reduced [94].

Table 4-6 outlines deposition condition for two different hydrogen dilution grading ncSi:H buffer layers.

The same conditions for band offset exist in i-layer/n interfaces. However, in this case, since the n-type nc-Si:H layer developed with high hydrogen plasma, band tailing is generally narrower and recombination at the interface is thereby reduced [94].

Table 4-6. Proposed ncSi:H buffer layer for p/i--layer and i-layer/n interfaces.

Samples		**PI1**		**PI2**
Pressure	**mT**	600		600
Power	**W**	5		5
Gas Ratio		$SiH_4:H_2$ 10:20	SiH4:H_2 10:20	$SiH_4:H_2$ 20:20
Time	**S**	20	40	45
Temperature	**°C**	280		

In addition, atomic hydrogen can reorder the surface of the interface layer by etching away the disordered Si–Si bonds and/or pre-existed impurities [94], and passivating the interface [95]. The excess atomic hydrogen in the plasma can also diffuse into the layer to allow structural relaxation [95]. To take advantages of H_2 passivation, a 30-second hydrogen plasma treatment is

set at 300mT pressure. 100 sccm H_2 gas flow rate is carried out in all interfaces before depositing any buffer or original layers.

4-3-2. Optimized device integration

The optimization is mainly focused on two different developed p-layers—one in high pressure (400mT) and the other one in low pressure (150mT). Table 4-7 summarizes different deposition conditions for developed optimized samples with illuminated I-V characterization.

Table 4-7. Depostion condition for developed optimized samples with acceptable results and their I-V characteristics.

Samples			OP1-S41	OP2-S30	OP3-S32	OP4-S42	OP5-S46	OP6-S45
AZO/p-layer buffer layer-deposition time (s)			AP1-120s	AP2-90s	AP3-120s	AP3-120s	AP3-120s	AP2-120s
p-ncSi:H	Pressure	mT	400	400	400	150	150	150
	Power	W	50	50	50	40	40	40
	Gas Ratio	SiH_4:H_2:B_2H_6	2:400:14	2:400:14	2:400:14	2:300:14	2:300:14	2:300:14
	Temperature	°C	260	260	260	260	260	260
	Thickness	nm	25	25	25	25	30	25
p/i buffer layer			PI1	PI1	PI2	PI2	PI1	PI2
i-ncSi:H	Pressure	mT	600	600	600	600	600	600
	Power	W	7	7	7	7	7	7
	Gas Ratio	SiH_4:H_2	4:20	4:20	4:20	4:20	4:20	4:20
	Temperature	°C	300	300	300	300	300	300
	Thickness	nm	150	150	150	150	150	150
n-ncSi:H	Pressure	mT	600	600	600	600	600	600
	Power	W	10	10	10	10	10	10
	Gas Ratio	SiH_4:H_2:PH_3	2:200:20	2:200:20	2:200:20	2:200:20	2:200:20	2:200:20
	Temperature	°C	300	300	300	300	300	300
	Thickness	nm	40	20	40	35	35	35
Voc		mV	733	714	757	681	682	704
Jsc		mA/cm^2	11.62	12.04	11.36	16.48	15.31	16.42
Efficiency		%	3.86	4.76	4.7	5.9	5.51	5.79
FF		-	45.4	55.4	54.7	52.6	52.8	50
R_{sh}		Ω	2800	2800	2600	1600	2200	940
Voc Slope		-	110	59	56	59	85	59

When comparing the V_{oc} and I_{sc} results of the optimized samples deposited with p-layer at 400mT, an increase in V_{oc} and I_{sc} was observed due to the incorporation of the two buffer layers. The most effective buffer layers for AZO/p-layer interface were AP1 and AP2, which showed an increase in V_{oc} of 2.23% and 7.12%. The short circuit current revealed an increase of 33.7%, rising from 8.66mA to 11.58mA. The overall performance enhancement boost is thus achieved when AP2 buffer layers for the AZO/p-layer interface and PI-1 buffer layers for the p-layer/i-layer interface are used, as improvement in the fill factor indicates.

Figure 4-25 shows the effect of buffer layers on the dark I-V curve of samples prepared with a p-layer at 400mT and 50W. It shows that AP1 and PI1 buffer layers improve the performance and fill factor by controlling the shunt current. Comparing the diode characteristics of these two samples demonstrates that shunt current is reduced after the deposition of buffer layers. Because the p-layer is the emitter and first deposited layer, the deposition condition of p-layer does not match the chamber specification (size of electrodes and chamber volume). It also decreases the quality of the next developed layers (i-layer), which causes the shunt current.

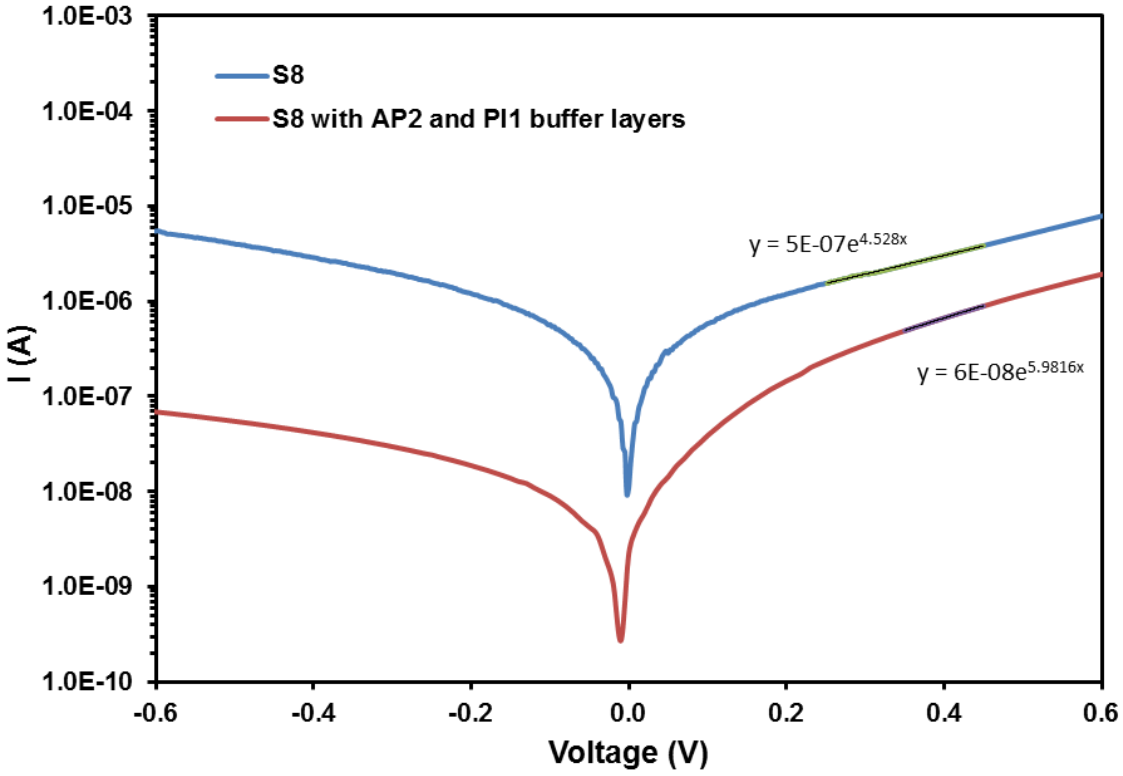

Figure 4-25. Effect of AP2 and AI1 buffer layers on Dark I-V characteristics of sample prepared with p-layer at 400mT and 50W.

The buffer layer effect on the performance of the device is dominant for lower pressure (150mT) p-layer, it improves the Isc by 30%-40% compare to higher pressure (400mT) p-layer. Figure 4-26 summarizes the Dark I-V characteristic p-layer with low pressure deposition at 150mT.

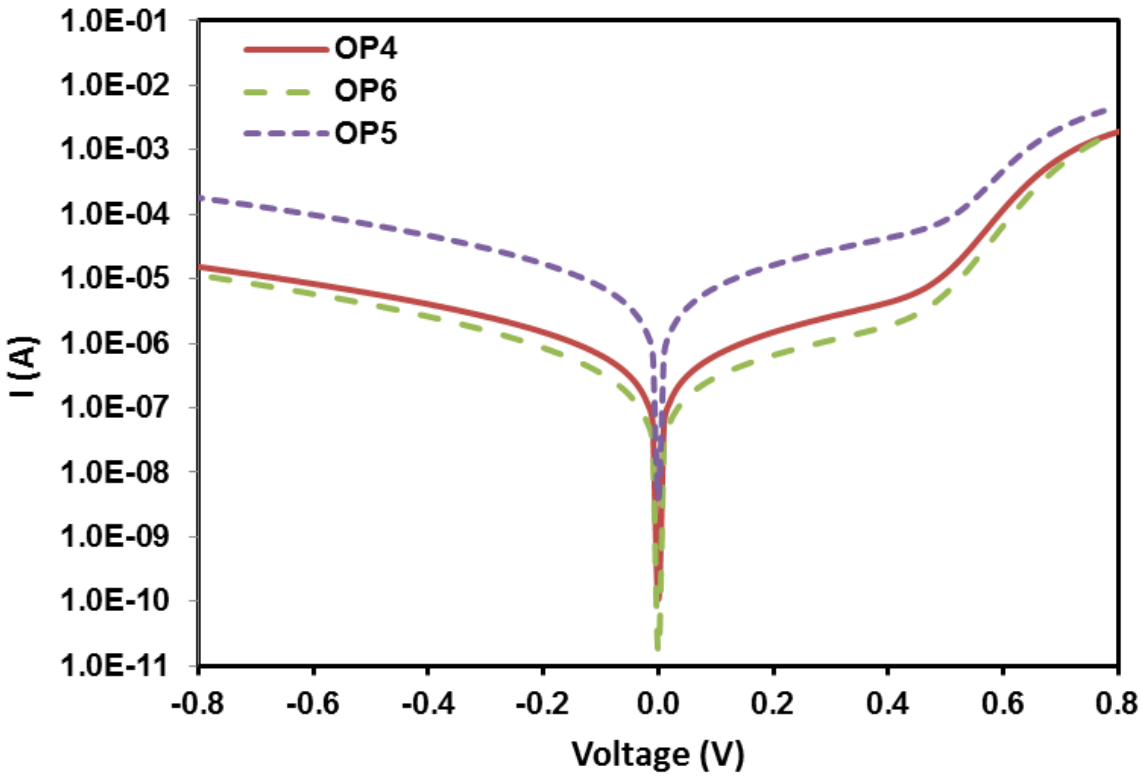

Figure 4-26. Dark I-V characteristic of samples with lower p-layer deposition pressure at 150mT.

Figure 4-27 shows the typical current-voltage characteristics of prepared solar cells with different p-layer depositions and different buffer layer under AM1.5 illumination.

One of the dominant effects of buffer layer integration is the enhancement of the short circuit current density (Jsc), specifically in sample with low pressure deposited p-layer, as shown in the EQE measurement result in Figure 4-28. Figure 4-29 shows a picture of OP5-S45 sample which has the best performance.

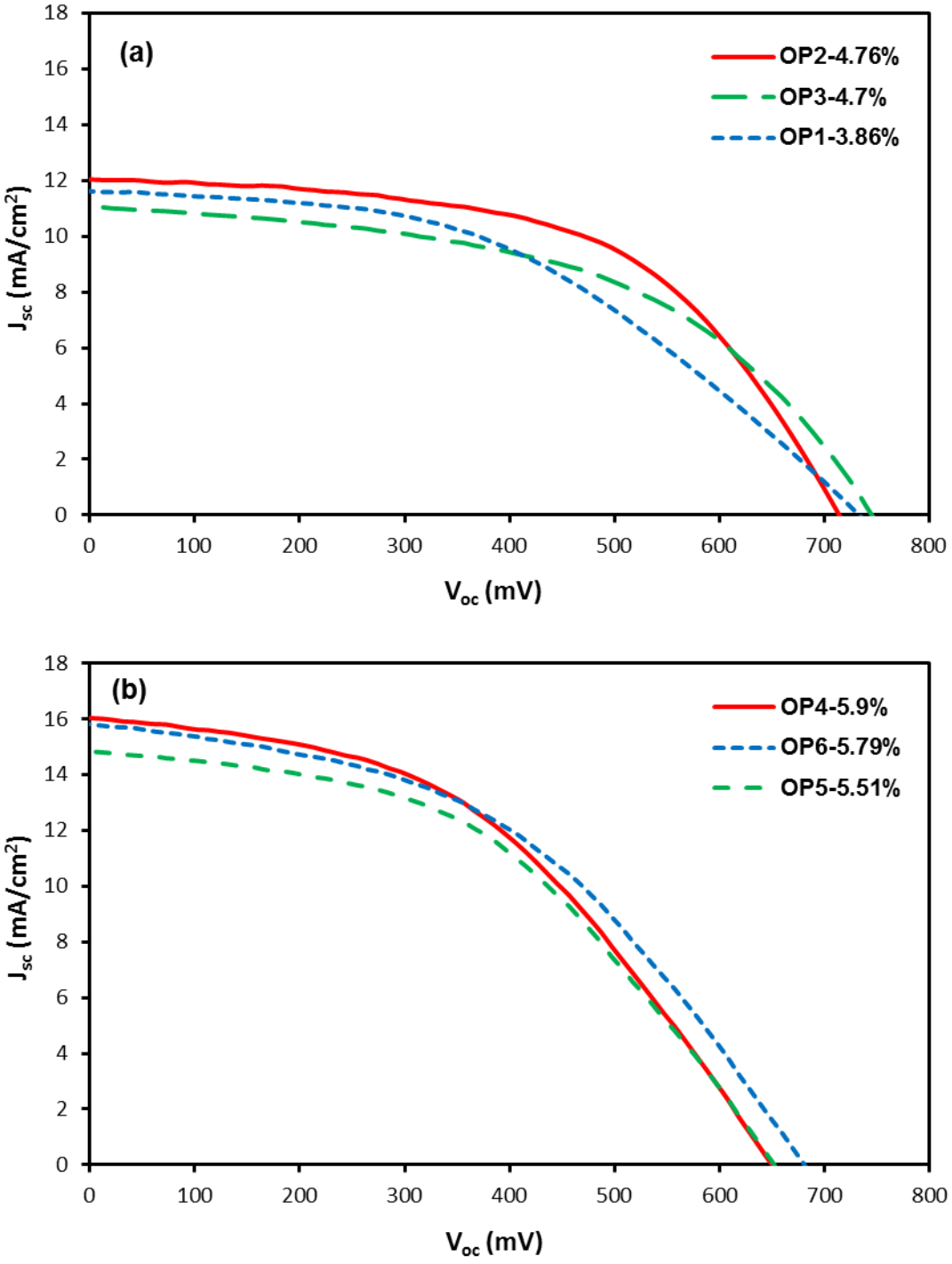

Figure 4-27. Current-Voltage characteristic of sample prepared with different buffer layer AP and PI and their efficiency, a) with p-layer deposition at high pressure (400mT), and b) p-layer deposition at low pressure (150mT), under 1.5AM illumination.

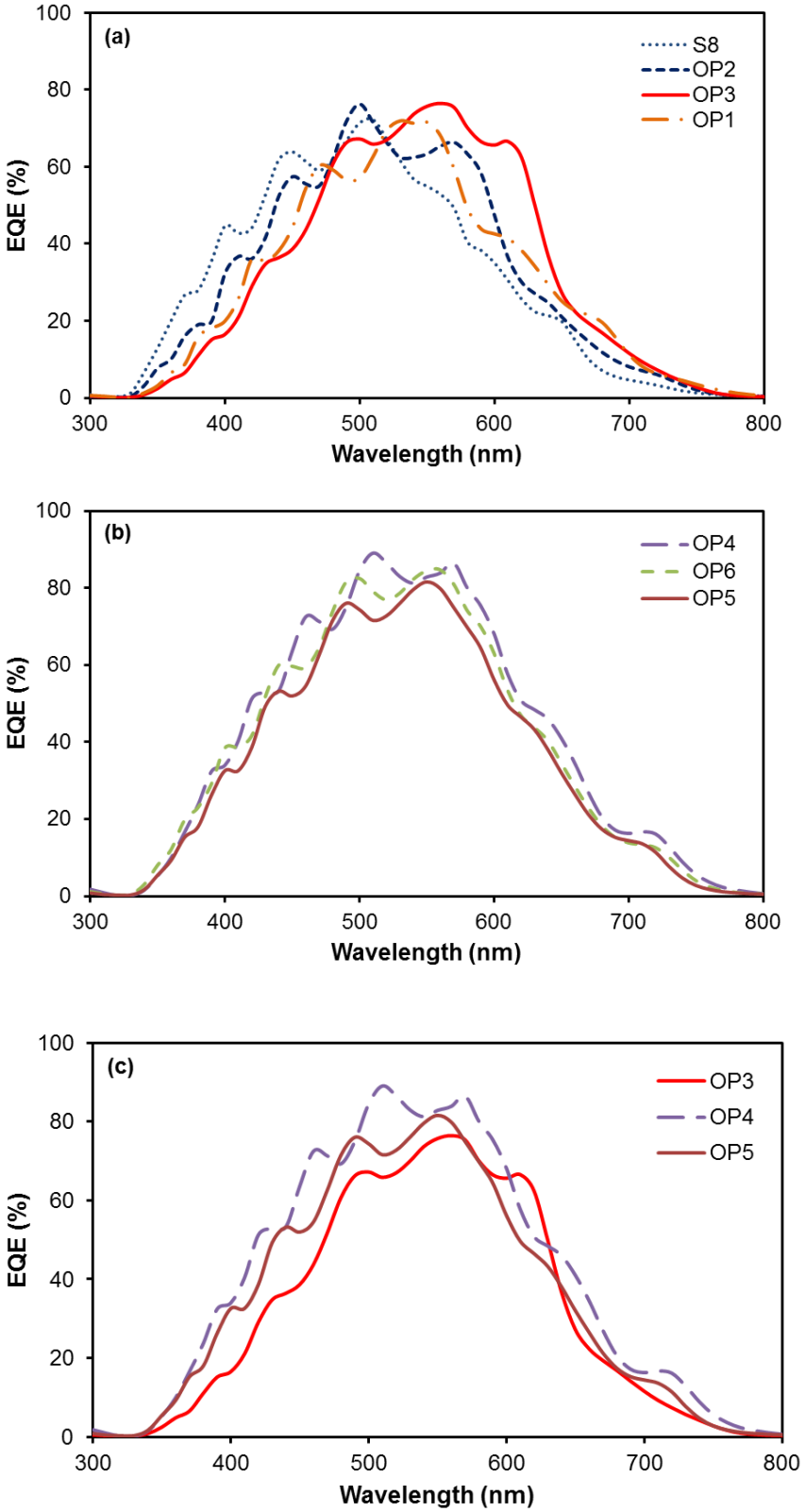

Figure 4-28. External quantum efficiency spectra of prepared samples.

Figure 4-29. Fabricated cell with actual view through the cell (200nm nc-aSi).

4-4. Summary

A study was done on the optimization of individual thin film for doped and un-doped nanocrystalline silicon. Different individual layers were deposited on glass substrate, and optimized based on their electrical and optical performance characteristics. For doped layers, p and n type, the effect of dopant gas ratio with PECVD deposition parameters (temperature, power, and pressure) was investigated to obtain the best electrical individual thin film.

The main step in performance optimization was carried out through device integration. In this step, p-layer (as the emitter) was chosen for further optimization. Different p-i-n solar devices were developed on AZO coated glass substrate. Different p-layer depositions (high pressure and low pressure) with distinct p-layer and n-layer thicknesses were chosen to investigate the effect of doped layer thickness and p-layer deposition conditions on the final device performance.

It was found that in order to achieve high V_{oc} in ultra-thin film devices, thickness of the doped layer must be increased to 25-30nm. As well, the lack of shunt current resistance and high series resistance severely affected the performance of devices. The main issue, as indicated by interface analysis, is related to the band tail offset at the p/I layer interface, and to the unsuitable barrier at the AZO/p-layer interface. Two different sets of buffer layers were developed for each of AZO/p-layer (AP1, AP2, and AP3) and p/I layer interfaces (PI1 and PI2). Different ultra-thin film devices were prepared with the implementation of these buffer layers. By utilizing dark I-V measurement, current-voltage characteristics and external EQE measurements on the effect of buffer layers were investigated.

Results show that the incorporation of a very thin lightly doped n-layer at AZO/P-layer adjusted the work function at the interface and set an appropriate barrier for carrier recombination at AZO/p interface. As well, by using a wider band-gap a-Si:H layer through varying hydrogen dilutions of ncSi:H at the p/i layer interface, the band offset problem is reduced at the interface, along with recombination current.

The final optimized devices were achieved by using the AP3 and PI2 buffer layer, and the final devices were fabricated on an AZO coated glass substrate, using AZO for back contact. The efficiency of 5.9% was achieved on a metal finger free sample, as an application for the semi-transparent ultra-thin film solar cells.

Chapter

5

Nanoplasmonic Architectural Design Parameterization and Device Simulation

In recent years nanoplasmonic architectures have witnessed a dramatic growth in interest and usage in photovoltaic energy conversion. In this chapter, by introducing nanoplasmonics and its application for photovoltaics, the simulation research and proposed structure are investigated.

5-1. Introduction: Why nanoplasmonic?

Optical absorption thickness and carrier collection length as explained in chapter 1 are the key elements in successful design of solar-cell architecture and selecting materials-fabrication methods. In Figure 5-1 by using FDTD simulation solar absorption spectrum graph for 2μm crystalline silicon wafer, and 100nm-300nm nanocrystalline silicon on glass with AM1.5 solar spectrum are shown. As shown in Figure 5-1, a large fraction of the solar spectrum is poorly absorbed, notably in the intense 600-1200 nm spectral range. Also, comparing the optical absorption graph reveals that ncSi:H thin-films has the potential of same absorption as a 2μm crystalline silicon wafer. Additionally, as explained before in the thin film cells due to the thin layer thickness the collection of all generated photocarriers do not strongly depend on the diffusion length of the junction

The small absorbance of near-bandgap light, specifically for the indirect-bandgap semiconductor, is a critical limitation in all thin-film solar cell technologies. To excel this limitation, nanoplasmonic light trapping, which allows light to bounce around inside the absorber, is an essential part of designing thin film solar cell structurs.

Many studies have been conducted on the optical properties of nanoparticle systems, but there are no systematic studies addressing the nanoplasmonic effect on photovoltaic energy conversion. This field was introduced only recently in photovoltaic energy conversion, with various scientists producing different results.

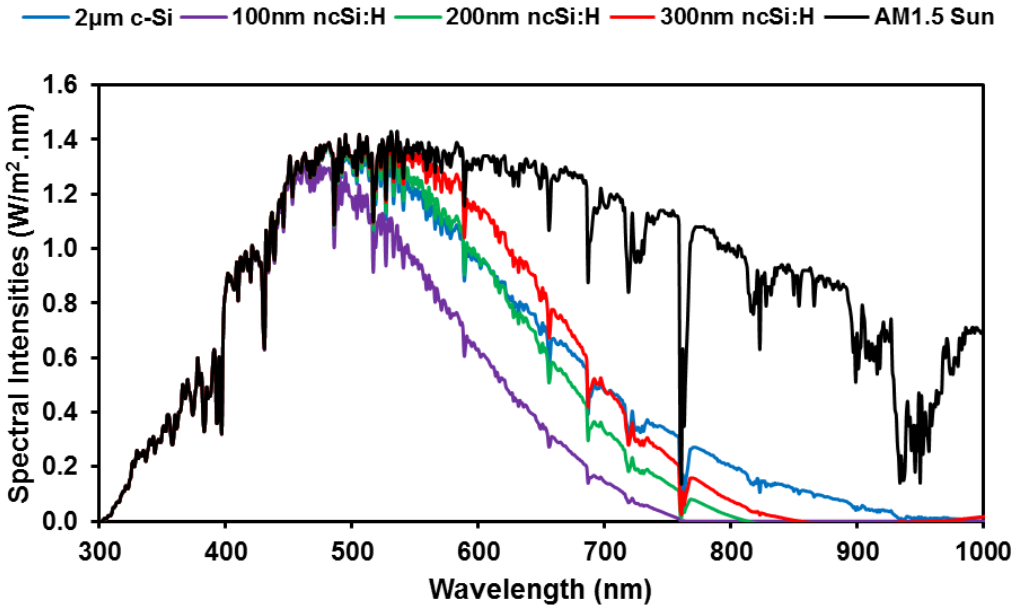

Figure 5-1. The solar absorption spectrum simulated graph for 2µm silicon, 300nm amorphous silicon, and 200nm amorphous silicon with AM1.5 solar spectrum.

One of the most pivotal discussions on assessing nanoplasmonic systems in solar cells contends the need to evaluate an array of nanoplasmonic objects, rather than a single component system. Thus, to address the issue, the overall aim of this section is to examine recent advances in nanoplasmonics and to underscore the high efficiency of ultra-thin film solar cells. The means for fulfillment will largely entail the exploration of enhanced absorption and carrier collection which is now enabled by nanoplasmonic systems in ultra-thin film with multispectral absorber layer. This chapter has three main objectives:

1) To present design parameterization for nanoplasmonic structures, in order to explore different mechanisms involved in solar light absorption enhancement in nanoplasmonic ultra-thin film solar cells.

2) To address nanoplasmonic simulation in design parameterization and optimization criteria for light trapping, light coupling, light concentration, and transparency. This step

introduces the use of a novel transparent nanoplasmonic conductor specifically designed for this research.

3) To introduce designs for new device architectures and simulation.

To summarize, by assessing the theoretical treatment in nanoplasmonic with specific consideration for photovoltaic energy conversion the device structure is presented and the device optimization through simulation is presented.

5-2. Nanoplasmonics by metallic nanoparticles

5-2-1. Design and realization of nanoplasmonic structures

Essential to designing any nanoplasmonic structures for photovoltaic energy conversion is the selection of a suitable target (base device) on which to apply nanoplasmonic architecture. For this work, nc-Si:H based thin films have been selected for further investigating the incorporation of nanoplasmonic structures for absorption enhancement. This decision was made for following reasons:

1) Hydrogenated amorphous silicon (a-Si:H) and nanocrystalline silicon (nc-Si:H) are the three major intrinsic materials used in multijunction thin film silicon-based solar cells [46].

2) Based on the best knowledge of the author, to date (when this research started) no study has been done on including and engineering nanoplasmonics for nanocrystalline silicon solar cells specifically for thin film and ultra-thin film applications.

The next step is to delineate the nanoplasmonic architecture strategy for these platforms. For this purpose the approaches of designing a nanoplasmonic structure associated with a combination of waveguide coupling and scattering effect simultaneously to further increase the possible enhancement mechanism considered. Nanostructures, based on array of nanoparticles, nanosemispheres, and nanodisks as a top or interstitial layer in nanocrystalline silicon solar cell, have been chosen for illustration. Figure 5-2 shows a schematic of this approach.

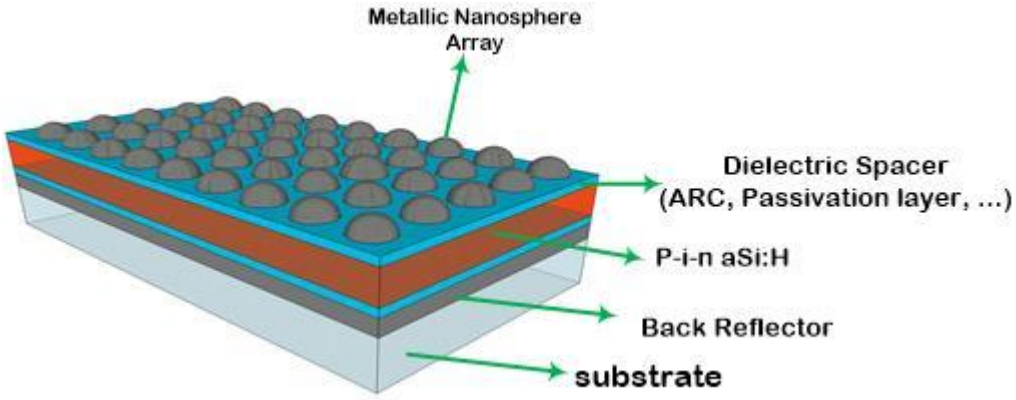

Figure 5-2. Schematic details of proposed nanoplasmonic structures for photovoltaics. An array of nanoplasmonic structures as a top layer for single junction amorphous silicon solar cells.

5-2-2. Nanoplasmonic simulation: design parameterization and optimization

Essential to designing nanoplasmonic architecture is proficiency in determining factors that affect the final performance of the structure. This process, known as parameterization, is a prerequisite for performance optimization. In nanoplasmonics, as relevant to photovoltaics, the key design aspects can be listed as follows:

1) Metallic materials type
2) Shape factors for nanoparticles, nanosemispheres, and nanodisks
3) Array parameters
4) Local dielectric environment

Selection of correct metallic material due to its effect on the presence of plasmon resonance has a critical impact on the modification of the absorption enhancement in wavelength of the incident light [21]. The most practical plasmon resonance wavelength is in visible range and since Ag and Au plasmon resonance wavelength located in this region, they have found numerous applications. A considerable amount of literature has been published on the effect of silver (Ag) as a nanoplasmonic object for the improvement of photovoltaic energy conversion [20-34]. However, there are other options, like aluminium (Al) and copper (Cu), which are cheaper, yet inspire less study in their application as a nanoplasmonic metal for absorption enhancement.

A powerful tool to evaluate different design parameters in plasmonic application is computer simulation. Finite Difference Time Domain (FDTD) is a highly integrated, and user-friendly software application that enables computer-aided design and the simulation of advanced passive and non-linear photonic components [44]. In this approach, the components of the electric field vector in a discrete volume are solved at a given instant in time. The process is repeated in an iterative nature until the desired transient or steady-state electromagnetic field behavior has fully evolved. The ability to make such computations gives rise to modeling multiple contiguous nanoparticle systems. It also allows one to rapidly investigate the use of other materials.

In the following section, FDTD simulations are used to consider more complex models, where different materials for both nanoparticles and local environments will be examined in relation to particle scattering efficiency for PV applications. Additionally, the role of particle coupling will be investigated as this has important implications in optimizing nanoparticle arrays for enhanced absorption in PV cells.

5-2-3. FDTD Solutions and Simulation Geometry

FDTD Solutions is a 3D Maxwell solver from Lumerical, capable of analyzing the interaction of UV, visible, and IR radiation with complicated structures employing wavelength scale features [96]. FDTD Solutions can solve the two and three dimensional Maxwell's equations in dispersive media, along with some simple non-linear media, where the user can specify arbitrary geometric structures and various input excitation sources [96]. The main reasons to implement FDTD solution in this research work are as follows:

- A unique material model known as Multi-Coefficient Material model (MCM) provides the capability of defining the materials properties over a wide wavelength spectrum (mainly solar spectrum, 300nm-1400nm) enables efficient calculation of device response for solar application. The key advantages of MCMs are in its extensive set of basic functions to better fit dispersion profiles that are not easily described by Drude, Debye, and Lorentz materials [96].
- Capability of utilization of multi-core computing system along with a built-in optimization framework for faster calculation of optimized nanophotonics devices responce [96].
- FDTD Solutions supports many boundary conditions, such as Perfectly Matched Layer (PML), periodic, and Bloch, which is a vital part of accurate simulation [96].

The basic simulation building block relies on the periodic array of an object (nanoparticle, nanodisks, nanosemisphere) on top of a solar cell (Figure 5-3). It should be highlighted that for the first round of investigation no conductive layer (TCO or Metal back conductor) considered in the device configuration to save in time of simulation. The active absorber layer is assumed to be a ncSi:H deposited on top of 2μm glass substrate. After investigating different parameters, a final simulation on a complete ultra-thin film nanocrystalline silicon with TCO is presented.

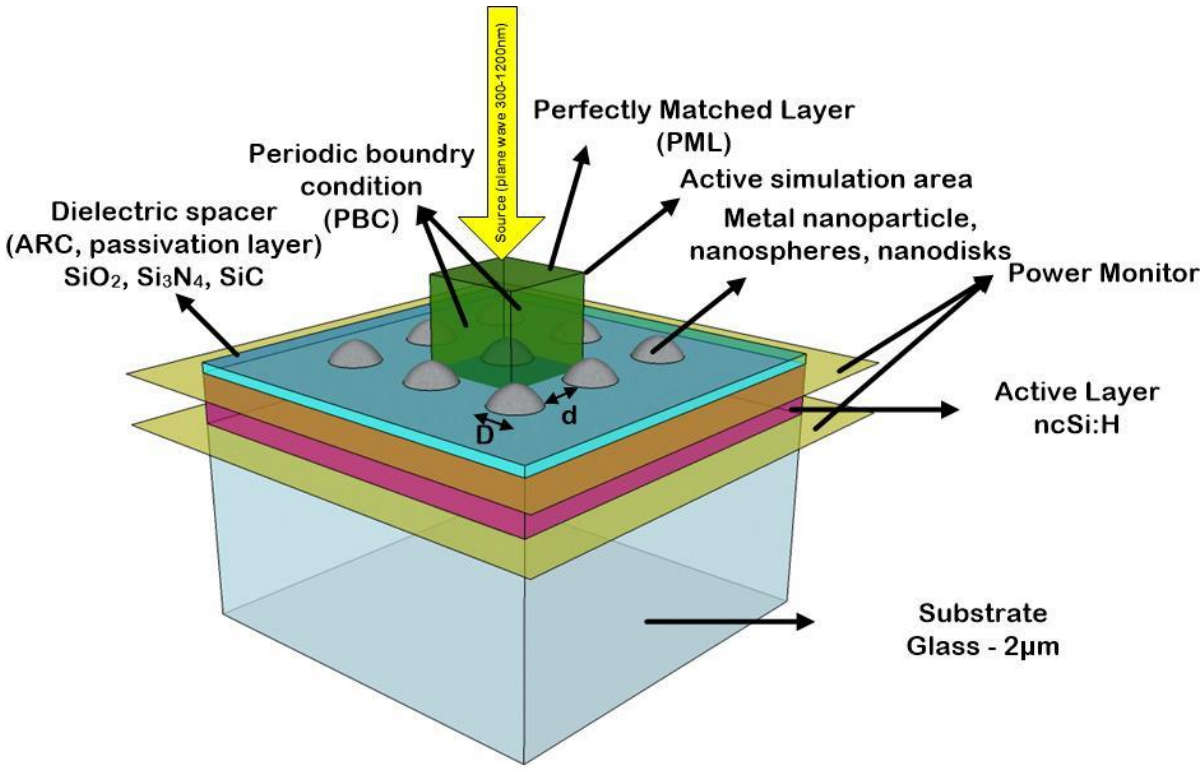

Figure 5-3. Schematic of proposed simulation building blocks. A periodic array of metal nanosphere used to evaluate absorption enhancement within ncSi:H layer. The periodic boundary condition and perfectly matched layer used as a boundary condition.

The multi-coefficient model (MCMs) is used here to model the material dispersion of metal and silicon [98]. This material model provides a much better fit for experimental data, than conventional models like Drude and/or Lorentz. Figure 5-4 shows the fitting curves given by the MCMs model for Ag, Al, Cu, ncSi:H, AZO over the solar spectrum range from 300nm to 1200nm.

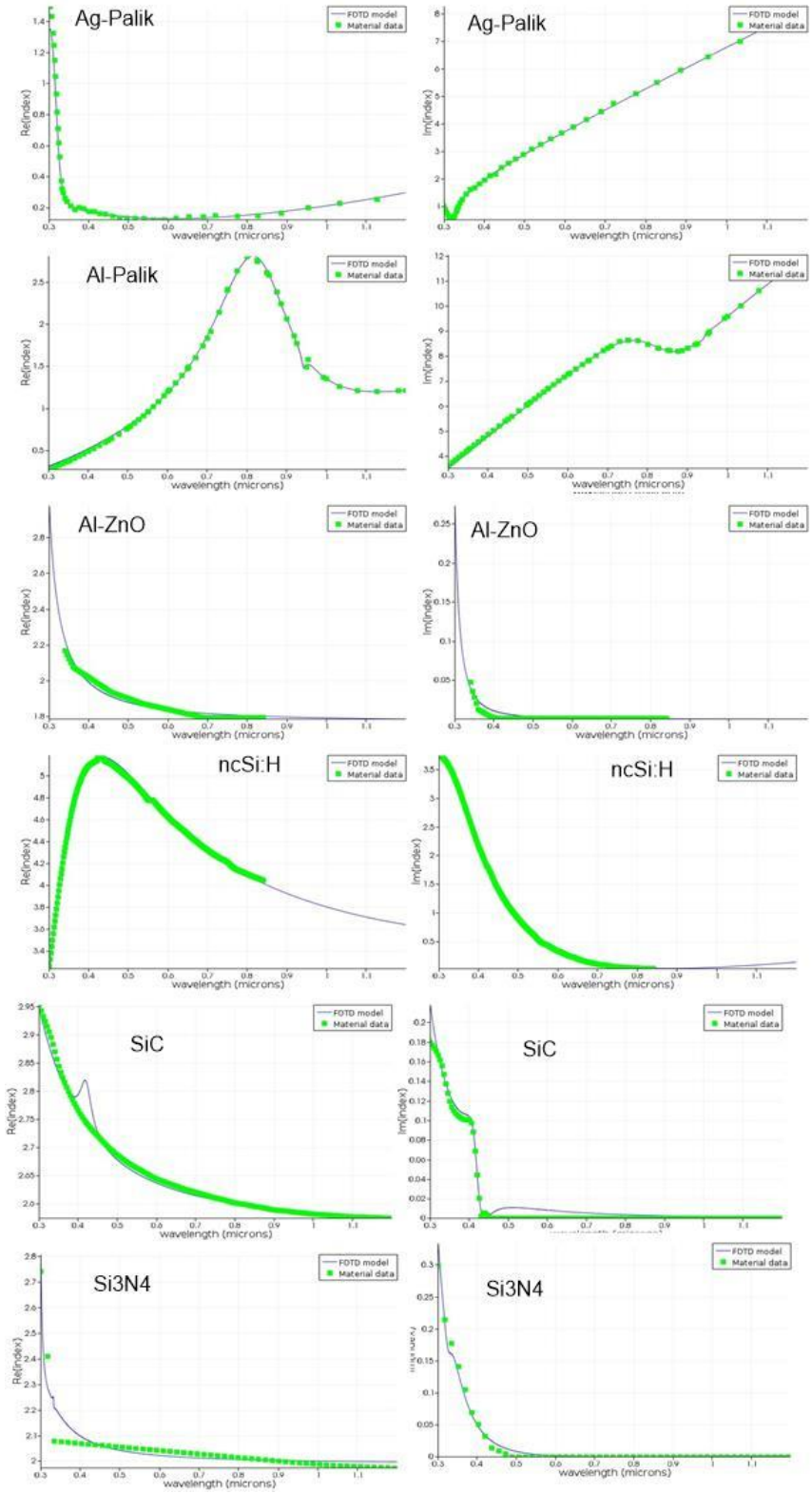

Figure 5-4. MCM models based on the materials data from experimental measurement and literature for Ag, Al, Cu, AZO, ncSi:H, SiC, Si3N4.

The dielectric function of Ag and Al are based on the measured data from Palik [97]. For ncSi:H and Al-ZnO the optical properties are measured and input as data into the software, in order to acquire more accurate simulation based on the PECVD deposition.

Perfectly Matched Layer (PML) boundary conditions are used for upper and lower boundary, while periodic boundary conditions (PCBs) are used for side boundaries to model the periodic nature of the particles. Symmetric and Anti-Symmetric boundary conditions are used to reduce the required memory size and computation time. Four mesh override regions are used: (1) "mesh-object" for abruptly changing field distribution around the object at the resonance frequency, (2) "mesh_space" for the meshing of space between the object and the surface, (3) "mesh_activelayer" for reducing the mesh points in x and y directions within absorbing layer and (4) "mesh_Glass" for the further reduction of mesh points.

A typical incident plane wave, with a wavelength range from 300nm to 1100nm, is used to model sunlight [99]. The purpose is to evaluate the impact of the proposed nanostructure on absorption enhancement in the broad sunlight spectrum, an important factor too often neglected in research works. In the results section the effect of this selection is discussed. Two power monitors are used at the top and bottom of the absorbing layer for the absorption calculation. The fraction of incident light absorbed in the ncSi:H layer is calculated by:

$$P_{abs} = -0.5\omega|E|^2 Im(\varepsilon) \qquad (5-1)$$

where ω is the frequency of incident light, $|E|^2$ is the total power inside the layer, and Im(ε) is the imaginary part of permittivity. The total integrated absorption, ABS_T, with in the spectral range of 300-1200 nm can be defined as

$$ABS_T = \int_{\lambda=300}^{\lambda=1100} P_{abs}(\lambda) I_{AM1.5}(\lambda) d\lambda \qquad (5-2)$$

where $I_{AM1.5}(\lambda)$ is AM1.5 solar spectrum obtained from the Renewable Resource Data Center [99]. To evaluate the performance enhancement in design parameterization, internal optical quantum efficiency (IQE) is used. IQE is defined as,

$$IQE = \frac{Number\ of\ photons\ absorbed\ by\ solar\ cell}{Total\ number\ of\ photons\ in\ sunlight\ (300-1200)} = \frac{\int_{\lambda=300}^{\lambda=1100} \frac{\lambda}{hc} QE(\lambda) I_{AM1.5}(\lambda) d\lambda}{\int_{\lambda=300}^{\lambda=1100} \frac{\lambda}{hc} I_{AM1.5}(\lambda) d\lambda} \quad (5-3)$$

where h is Planck's constant, c is the speed of light in the free space, and $QE(\lambda)$ is optical quantum efficiency calculated by,

$$QE(\lambda) = \frac{P_{abs}(\lambda)}{P_{sun}(\lambda)} \quad (5-4)$$

where $P_{sun}(\lambda)$ is the power of incident light. Therefore, the absorption enhancement ratio, $\eta(\lambda)$, and the IQE enhancement ratio, E_{IQE}, are defined to evaluate the efficiency of metallic nanostructure,

$$\eta(\lambda) = \frac{QE_{plasmonic}(\lambda)}{QE_{bare}(\lambda)} \quad (5-5)$$

$$E_{IQE} = \frac{IQE_{plasmonic}}{IQE_{bare}} \quad (5-6)$$

The short circuit current density, J_{SC}, by assuming that all electron-hole pair contributes to photocurrent can be calculated by,

$$J_{SC} = e \int_{\lambda=300}^{\lambda=1100} \frac{\lambda}{hc} QE(\lambda) I_{AM1.5}(\lambda) d\lambda \quad (5-7)$$

where, e is the charge of electron.

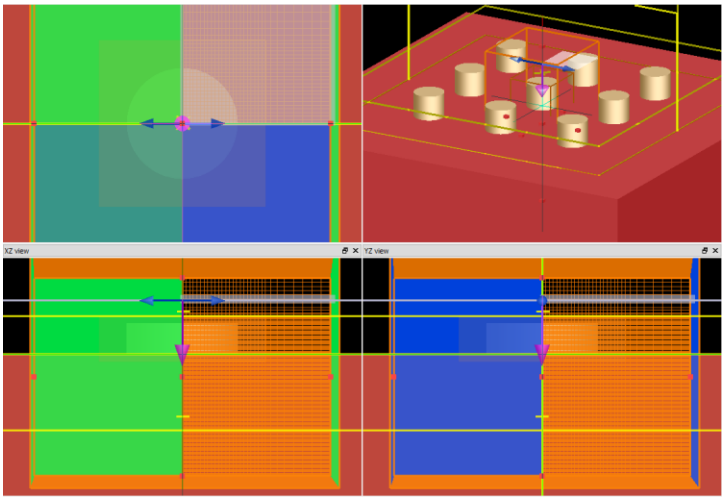

Figure 5-5. Screenshot of simulated structures in FDTD solutions.

5-3. Nanoplasmonic simulation results

Device parameterization and simulation through the baseline outline mentioned above is carried out in accordance with the flowchart given in the Figure 5-6 flowchart.

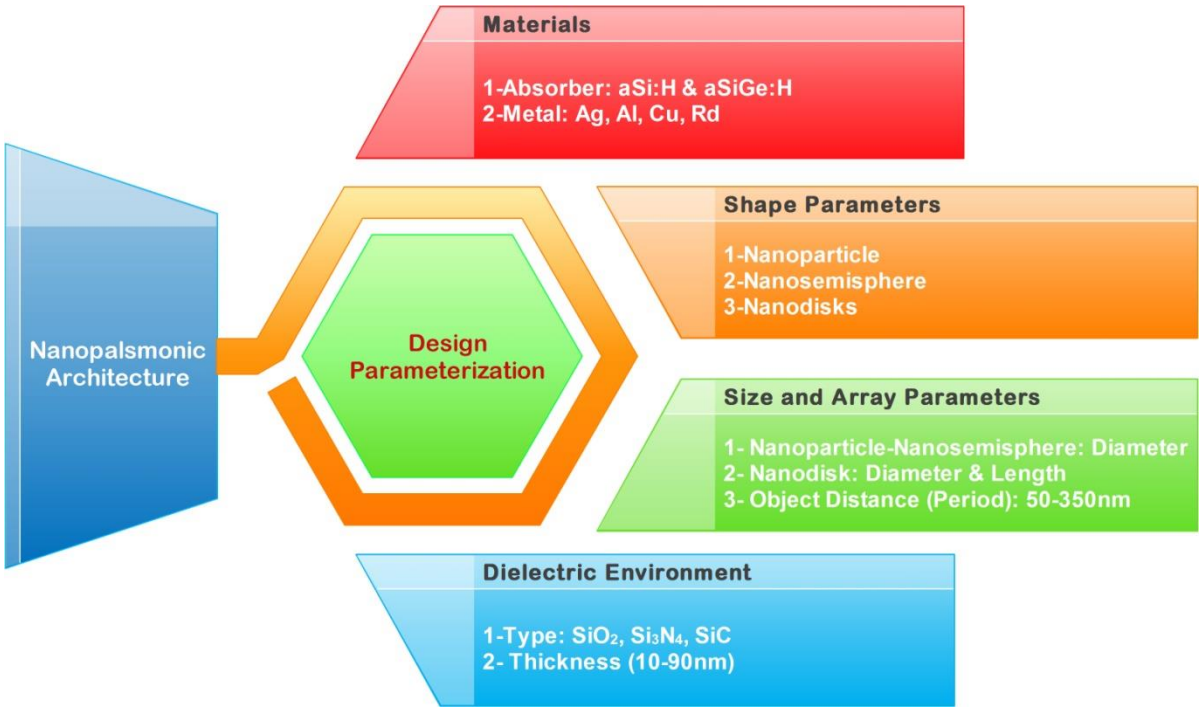

Figure 5-6. Flowchart of a nanoplasmonic design parameterization for proposed structures.

5-3-1. Nanoplasmonics in nanocrystalline silicon (ncSi:H)

Three hundred nanometer ncSi:H on a glass substrate with 10nm SiO_2 as a passivation layer and anti-reflection coating (as described in Figure 5-3), is defined in an FDTD model to evaluate the effect of nanoplasmonic in ncSi:H.

5-3-1-1. Metallic Nanoparticle Type

To begin, the best way to assess the effect of nanoparticles is to evaluate the variation of the IQE with particle distance from each other (d) and particle diameter (D). Figure 5-7 presents the IQE changes of 300nm ncSi:H as a function of d and D for silver and aluminium nanoparticles.

A peak enhancement of IQE is clearly seen at optimum d and D for each material. It may be noted that for silver, the maximum IQE, which equals to maximum optical absorption, is obtained for nanoparticle arrays with D=200nm and d=250nm with IQE=0.4285. By considering the IQE=0.3171 for a bare ncSi:H solar cell (a cell without nanoparticles), 35.13% becomes the amount of absorption enhancement for Ag nanoparticles. In addition, further analysis shows that enhancements are low for small nanoparticles (below 100nm) and large nanoparticles (above 300nm). This feature is due to light absorption by small nanoparticles and less effective forward scattering for large nanoparticles caused by the high-order plasmon excitation, respectively [100][101][102]. Data for Al nanoparticles shows that the maximum optical absorption is 31.91% for Al nanoparticle arrays with D=200nm and d=250nm with IQE=0.4183. Figure 5-8 shows E_{IQE} ratio variation for Ag and Al nanoparticle arrays. The dependency of enhanced absorption in particle size and distance for both Al and Ag is equally clear. Figure 5-8 (a) reveals that for any constant Ag nanoparticle size (D) incurred from an increase in inter-particle distance (d), there would be a maximum peak in absorption; whereby, through an increasing particle distance (d), that maximum would shift to a higher inter-particle distance. However, further increase of inter-particle distance at a specific point could decrease absorption enhancement. It is apparent from Figure 5-8 (b) that for specific inter-particle distance for Ag the same scenario exists. There is nanoparticle diameter in which absorption is maximized and by increasing particle size this maximum shifts to a higher inter-particle distance.

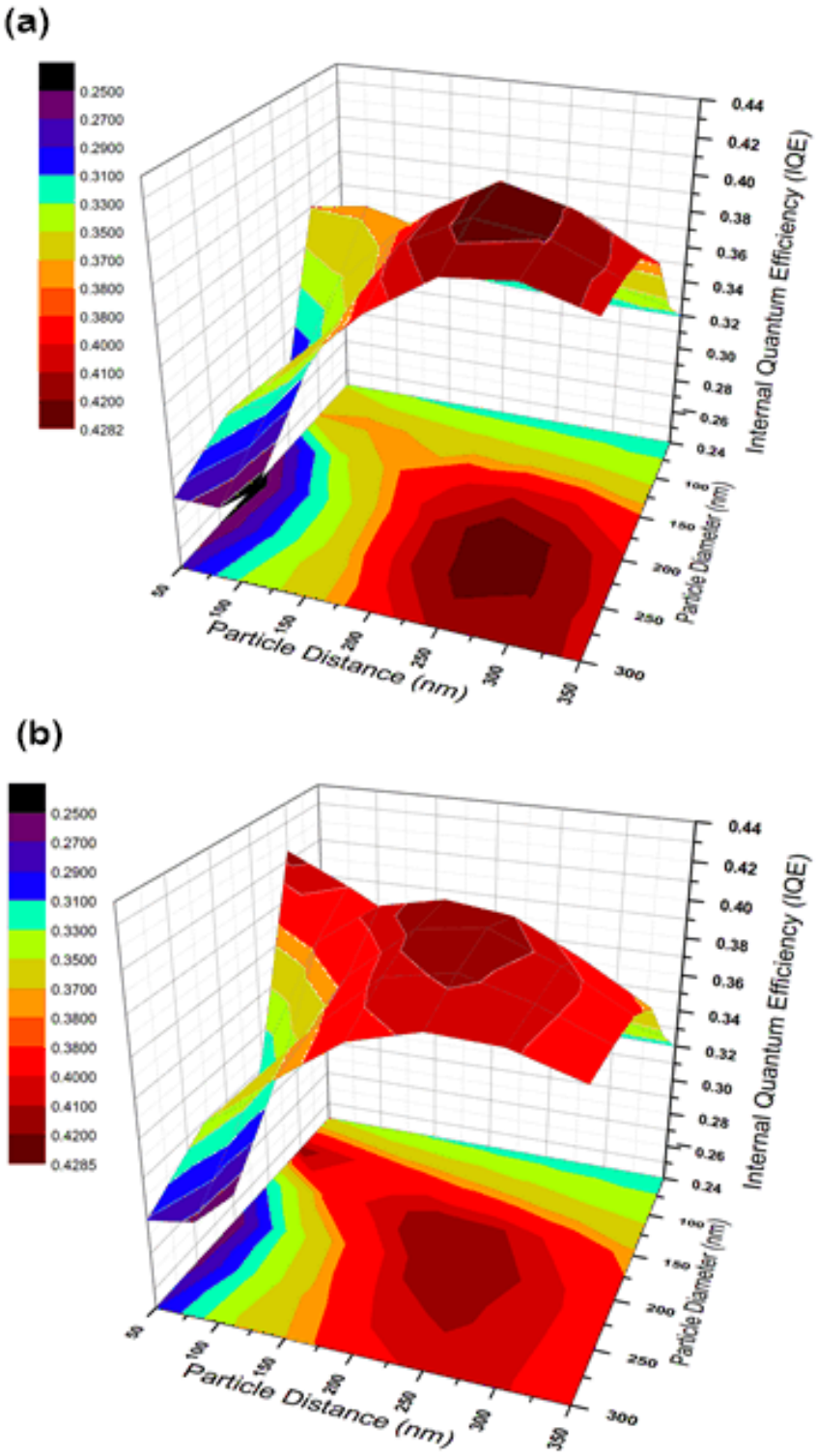

Figure 5-7. Internal Quantum Efficiency (IQE) of (a) Silver, and (b) Aluminium plasmonic nanoparticles on top of proposed ncSi:H solar cell as a function of the particle diameter (D) and the particle distance (d).

Figure 5-8 (c) and (d) reveal the same scenario for Al nanoparticles, that for any constant particle distance incurred from an increase in particle size, there would be a maximum peak in absorption; whereby, through an increase in particle distance (d), that maximum would shift to a higher particle diameter. However, further increase of particle size at a specific point could decrease absorption enhancement.

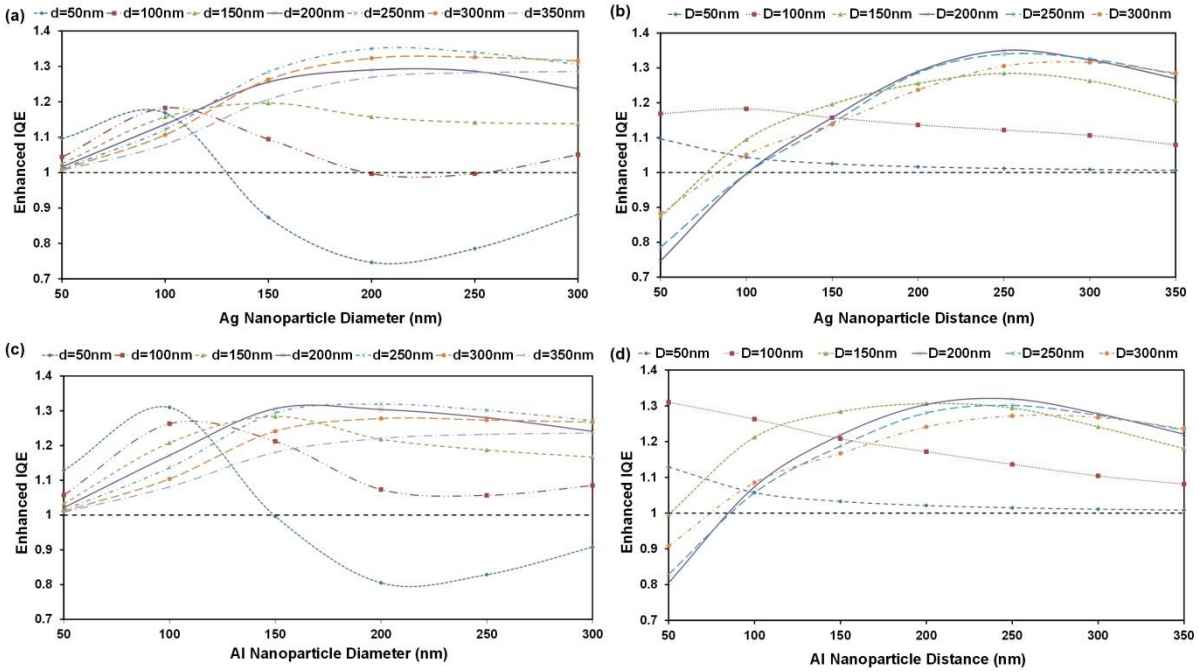

Figure 5-8. Enhanced internal quantum efficiency ratio changes of Al/Ag nanoparticle arrays on 300nm ncSi:H-10nmSiO_2 solar cell, (a, c) based on different inter-particle distance for 200nm nanoparticle, (b, d) based on different nanoparticles diameter for 250nm inter-particle distance. The black dashed line is the reference cell (bare solar cell without nanoplasmonic).

It is also notable that by increasing the nanoparticle distance the rate of variation for E_{IQE} changes decreases and becomes wider. This phenomena is also visible in Ag (Figure 5-8 (a)). The only differences between Ag and Al is its higher E_{IQE} at small nanoparticle diameter. Both metals almost show their maximum performance at the same nanoparticle array scheme of 250nm inter-particle distance and 200nm nanoparticle diameter.

The mechanistic view of surface plasmon resonance (SPR) in metal nanoparticles is the key to explaining these results [103][104][105][106]. For small metallic nanoparticles, scattering processes are usually negligible, and the particle absorbs energy through three major mechanisms:

i) Collective excitations of the "free" electrons, which give rise to surface modes or SPR determined by the particle shape, size, environment, and material composition;

ii) Electronic transitions of bound electrons from occupied to empty bulk bands of different indexes, also called inter-band transitions; and

iii) Surface dispersion or scattering of the "free" electrons, when their mean free path is comparable to the dimension of the nanoparticles. These mechanisms are the dominant reasons for decreasing enhanced internal quantum efficiency by increasing Ag nanoparticle size.

These mechanisms are the dominant reasons for decreasing enhanced internal quantum efficiency by increasing Ag nanoparticle size.

Figure 5-9 illustrates the variation of the absorption enhancement ratio $\eta(\lambda)$ with wavelength for a different Ag and Al nanoparticle array characteristics. It is clear from the Figure 5-9 (a) and (b) that as particle diameter increases from 100nm to 300nm, a number of absorption enhancement peaks increases. This increase contributes to the increase of local surface resonance (LSPR) modes in coupled metallic nanoparticle array [103][21]. The presence of these multipole modes in coupled nanoparticles can be attributed to a no-uniform, incident field driving the LSPR. These excite LSPRs, inducing polarization currents in individual particles that radiate into the underlying structure. If the thickness of a spacer layer is small, the radiating nanoparticles transfer a significant portion of their energy in to the waveguide modes of the absorber layer. The particle-waveguide coupling enhances absorption in the thin Si layer, because the coupled light is "trapped" by the guided modes, in contrast with light trapping in solar cells [104].

Furthernore, the wavelength at which enhanced absorption goes below one, indicating the absence of enhancement, accordingly shifts towards a higher wavelength by increasing nanoparticle size. This red-shift is scribed to the red-shift of resonance. As the particle radius becomes larger in fixed particle distance, two factors must be considered; first, the incident external driving field about the particle will become less uniform, and second, the gap between the surfaces of the particles becomes smaller resulting in stronger inter-particle coupling. Both factors increase dynamic depolarization, which ultimately gives rise to the multipole LSPR mode.

Figure 5-9 (b) and (c) describes the variation of the absorption enhancement ratio $\eta(\lambda)$ possessing a wavelength for different inter-particle array distances between 150-350nm, and a diameter of 200nm for Ag and Al nanoparticles. It is clear that as the inter-particle distance increases from 150nm to 350nm, a blue shift is observed in the wavelength at which maximum absorption enhancement occurs. Hence, as the arranged nanoparticles are brought closer, keeping their size, shape and other parameters constant, the change in overall absorption behavior, within ncSi:H, corresponds to the change in the inter-particle coupling between them.

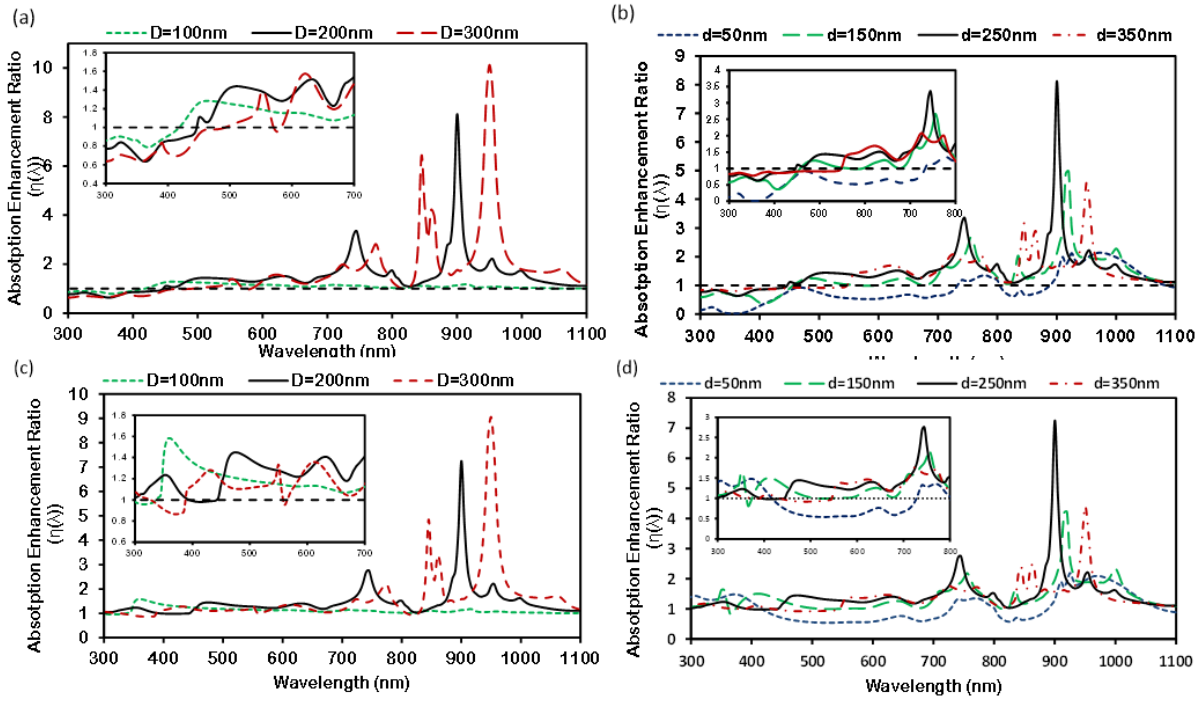

Figure 5-9. Absorption enhancement ratio for Ag (a) and (b) nanoparticles, and Al (c) and (d) nanoparticles. (a) and (c) Nanoparticle arrays with inter-particle distance of 250nm and different diameter, (b) and (c) Nanoparticle array with 200nm diameter and different inter-particle distances. The inset shows absorption enhancement at short wavelength (300-800nm).

If nanoparticles have a large inter-particle distance, d, the plasmon coupling strength is similar to that of the interaction energy between two classical dipoles, where the coupling potential decays as $(1/d^3)$ [105]. In this state, the radiative dampening of the induced dipole dominates over that of dynamic depolarization and a single dipole resonance results. Conversely, at very small distance, d, coupling of the near-by dipole fields intensifies and is expressed by the superposition of the external driving field and in accordance with near-field dipole fields.

Through this superposition, coupled nanoparticles greatly confine the net field between particles, causing a non-uniform external driving field across each particle. As d decreases, the dynamic depolarization strengthens, and the LSPR exhibits a red-shift in consequence to the heightened dephasing and mixing of higher-order multipole oscillations within each nanoparticle.

The red- or blue-shift in arrays of metal nanoparticles in comparison to single particle spectra has already been reported when polarized light is used to illuminate the structure depending upon the angle of illumination and polarization of incident light [106][107]. Here, it is shown, by illuminating the structure with unpolarized light, the effect of increasing inter-particle coupling between nanoparticles shifts the peak of absorption enhancement curve within ncSi:H. as explained before, this behavior is attributed to the decaying field distribution between consecutive particles as near-field inter-particle coupling decreases with increasing array period.

In Figure 5-10 the total power absorption in 300nm ncSi:H layer, the total reflection power, and total absorption in metallic nanoparticles due to incident light for Ag and Al. It is apparent from Figure 5-10 (a) that a broadband absorption enhancement in ncSi:H layer occurs for both Al and Ag, a change ascribable to the dramatically reduced light reflection shown in Figure 5-10 (b). However, absorption in the ncSi:H layer in the presence of Ag nanoparticles reduces in the short wavelength as compared to Al. This phenomenon is due to the strong parasitic light absorption near the surface plasmon resonance wavelength, as shown in Figure 5-10 (c). Al nanoparticles have smaller parasitic absorption in the shorter wavelength region, since the surface plasmon resonance of Al nanoparticles lies in the ultraviolet region where the intensity of solar irradiance is negligible. Figure 5-10 (b) compares broad band reflection and absorption spectra of Ag and Al nanoparticles array with bare ncSi:H solar cells. The reflection for base solar cells (black dot line) shows strong oscillation that becomes broader for increasing wavelength. These result from the Fabry-Perote effect in the different layers, which occurs when cells behave like a waveguide by cause of the active layer (ncSi:H), with the refractive index of around 3.9 being located between spacer (n~1.4) and glass substrate (n~1.5). Comparing the dot red and green line with black dot line indicates, first, that the particle array gives a broadband reduction in the reflectivity. The Fabry-Perot peaks in the reflection spectrum are reduced because the particles preferentially scatter the reflected light back into substrates.

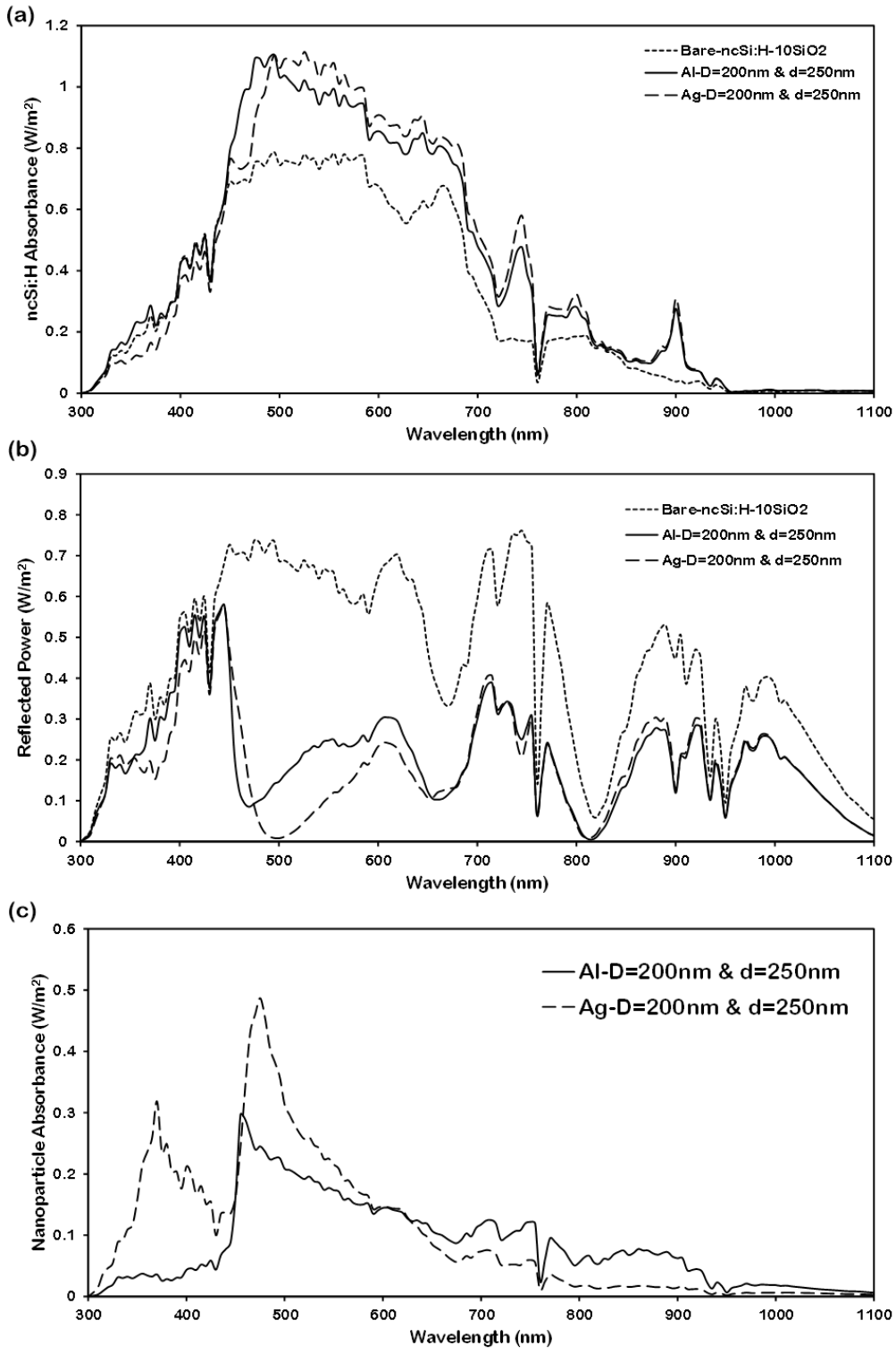

Figure 5-10. Spectral characteristics of (a) ncSi:H absorbance (b) reflection (c) nanoparticle absorbance of the 200nm diameter Al (red), Ag (green) nanoparticles with particle distance of 250nm placed on the front surface of 300nm-ncSi:H/10nm-SiO_2 solar cell.

Second, the occurrence of sharp dips at some wavelengths such as 745nm and 900nm which is in parallel with sharp increases in absorption spectrum reveals that the particle array generates enough in-plane momentum to couple light into waveguide modes of active layer.

To prove that the sharp dips in reflection are due to mode coupling, the fraction of incoming power that is absorbed in the 300nm ncSi:H active layer is calculated through the equation (5-2). To further explore the broadband absorption enhancement, the profile of optical absorption per unit volume (μm^3) in active layer at different wavelength for Ag and Al nanoparticles on top of 300nm-ncSi:H/10nm-SiO_2 solar cell are shown in Figure 5-11.

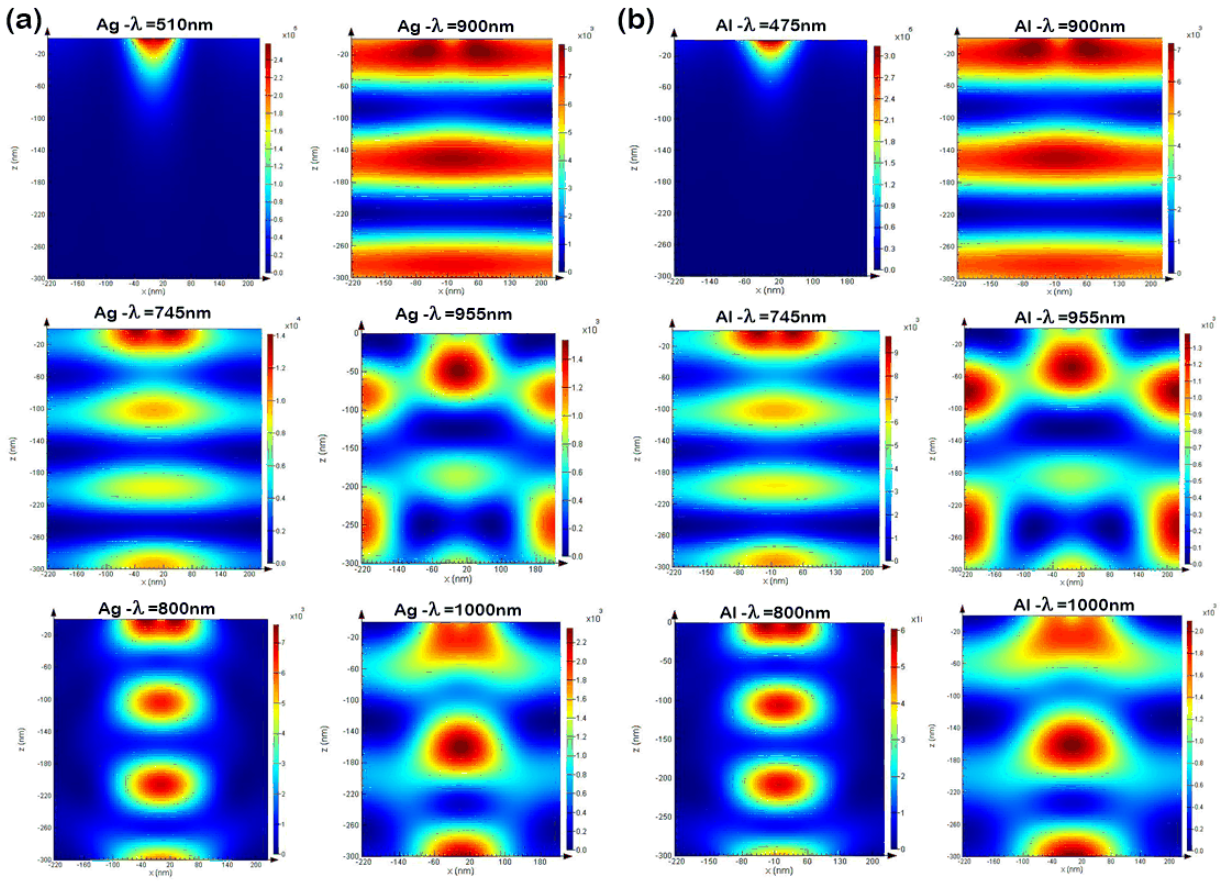

Figure 5-11. The optical absorption profile per unit volume for 300nm-ncSi:H active layer in the presence of (a) Ag and (b) Al nanoparticles array, with 200nm diameter and 250nm inter-particle distance at different wavelengths.

The occurrence of light forward scattering toward active layer at wavelength of 510nm and 475nm are clear for both Ag and Al respectively. In addition, in both Ag and Al the nanoparticles scatter incident light into the substrate, resulting into a local intensity

enhancement and thereby a local absorption enhancement at the location of particles (x=0). Additionally, the light coupling to the waveguide mode of ncSi:H layer propagates through the waveguide in the horizontal direction is also evident. This, in turn, causes an oscillating intensity profile as a function of x with a wavelength that depends on the inter-particle distance. This can be attributed to the evanescent tail of the waveguide mode interacting with particle array, thereby experiencing a periodically changing effective refractive index. This gives rise to the formation of Bloch-mode (Figure 5-11 (a)) as an example in wavelength 955nm. These two figures also suggest that light coupling to a waveguide mode propagates in the in-plane direction. At this point, it may be concluded that investigating the waveguide mode in active region, specifically for ultra-thin film structures is an essential and helpful tool to predicts and engineer the solar cell absorption.

5-3-1-2. Effect of spacer materials and thickness

In order to evaluate the effect of a spacer, SiC, Si3N_4, SiO_2 , and Al-ZnO (AZO) have been chosen for further investigation. In Figure 5-12, the IQE of the 300nm ncSi:H solar cell are calculated for these three spacers with different thickness, from 10nm-85nm. SiC and Si_3N_4 generally show higher IQE in comparison to SiO_2. The lower refractive index for SiC and Si_3N_4 is comparable to SiO_2, making them more efficient as an anti-reflection coating for nanocrystalline silicon and justifying their higher absorption enhancement.

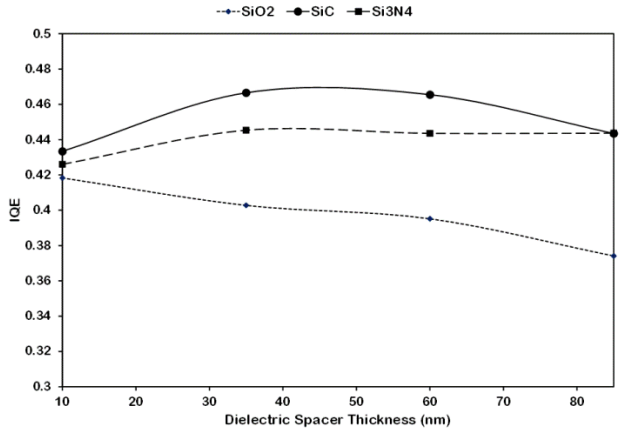

Figure 5-12. Internal Quantum Efficiency of 300nm ncSi:H solar cell Al nanoparticles with 200nm diameter and 250nm inter-particle array distance on top layer and different dielectric spacer thickness and materials.

Additionally, in the SiO_2 spacer, IQE is decreasing by increasing dielectric thickness. The reduction of near-field coupling, caused by an increase in distance between nanoparticles and active layer, has contributed to this reduction in IQE. However, this reduction is not so effective for SiC and Si_3N_4 at the thickness of 30nm-40nm, on account of their effective anti-reflection properties, although the overall IQE eventually decreases by further increase of thickness.

Figure 5-13 shows absorption enhancement ratio ($\eta(\lambda)$) vs. wavelength changes with different spacer thickness for SiC, SiO_2, and Si_3N_4. Figure 5-13(b) and (c) indicated the red-shift enhanced peak to longer wavelength by increasing thickness. Further ramification of simulation calculation reveals that the enhanced absorption peak can be tuned by variation of dielectric spacer as shown in Figure 5-13. It is clear that the rate of changes is higher for SiC, Si_3N_4, and SiO_2 respectively. These results show that the coupling of LSPs of metallic nanoparticle array is strongly related to the spacer layer thickness.

This dependency is attributed to the impact of spacer layer on the fraction of forward scattering and scattering cross section [35]. The absorption enhancement peak also shows the redshift to longer wavelength for different spacer material at constant thickness. In Figure 5-14, the $\eta(\lambda)$ variation with constant thickness for different spacer materials presented. It is evident that at constant thickness, by changing the spacer dielectric from SiC to Si_3N_4 and SiO_2, the $\eta(\lambda)$ enhanced peaks shifts to a longer wavelength. This effect provides a tool for optimal tuning of metallic nanoparticle architecture for thin film solar cells.

5-3-1-3. Effect of ncSi:H active layer thickness

For the final investigation, the effect of ncSi:H thickness as an active layer is studied. Specifically, to follow is on evaluative discussion on the effect of a Al nanoparticle array, with a 200nm diameter and an 250nm inter-particle distance, on the absorption enhancement of a ncSi:H absorber layer with a 100nm, 200nm, and 300nm thickness and 10nm SiO_2 dielectric spacer.

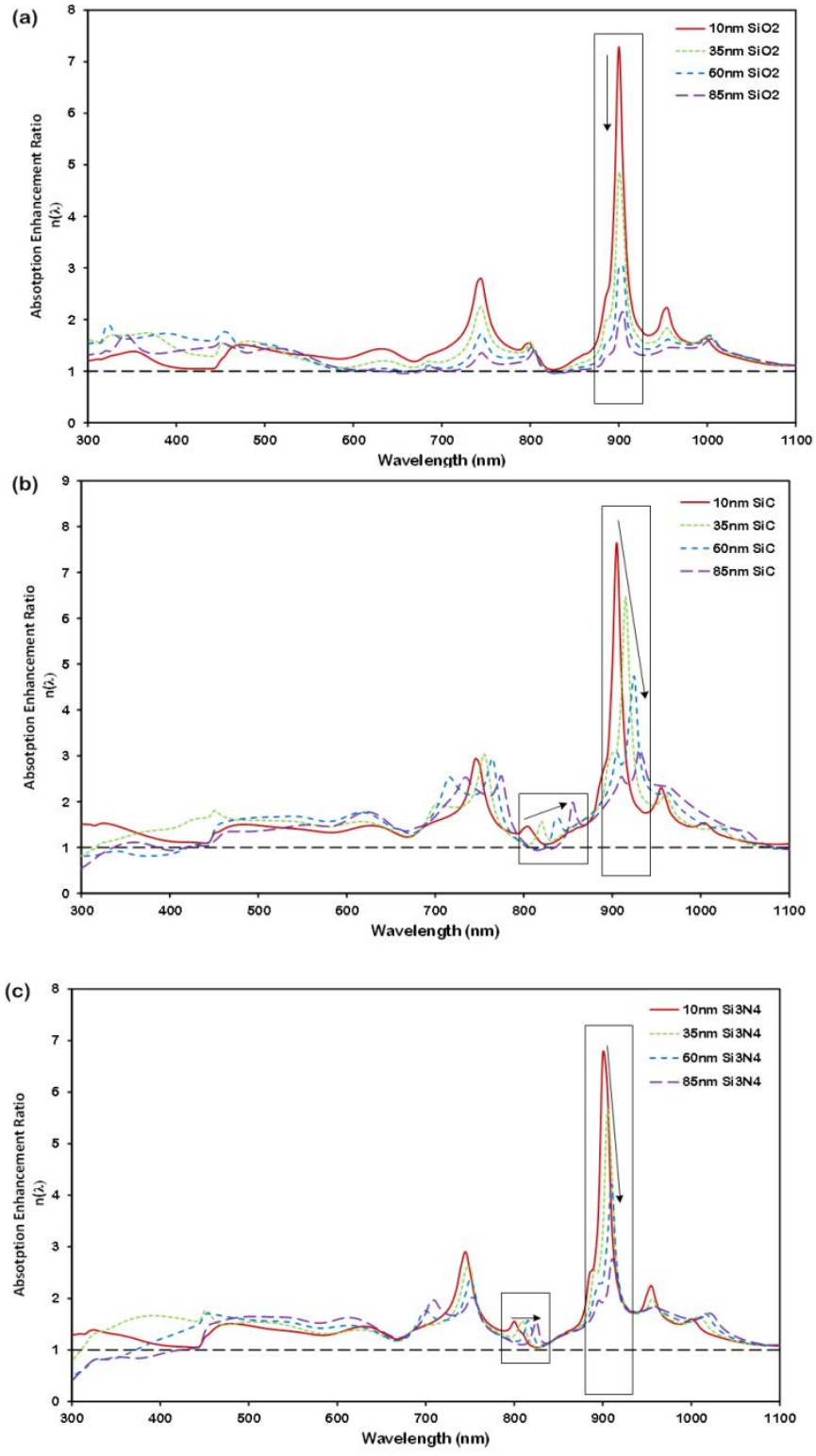

Figure 5-13. Calculated External Quantum Efficiency (EQE) for different spacer dielectric thickness and materials for 200nm diameter Al nanoparticles array with 250nm inter-particle distance on top of 300nm ncSi:H active layer.

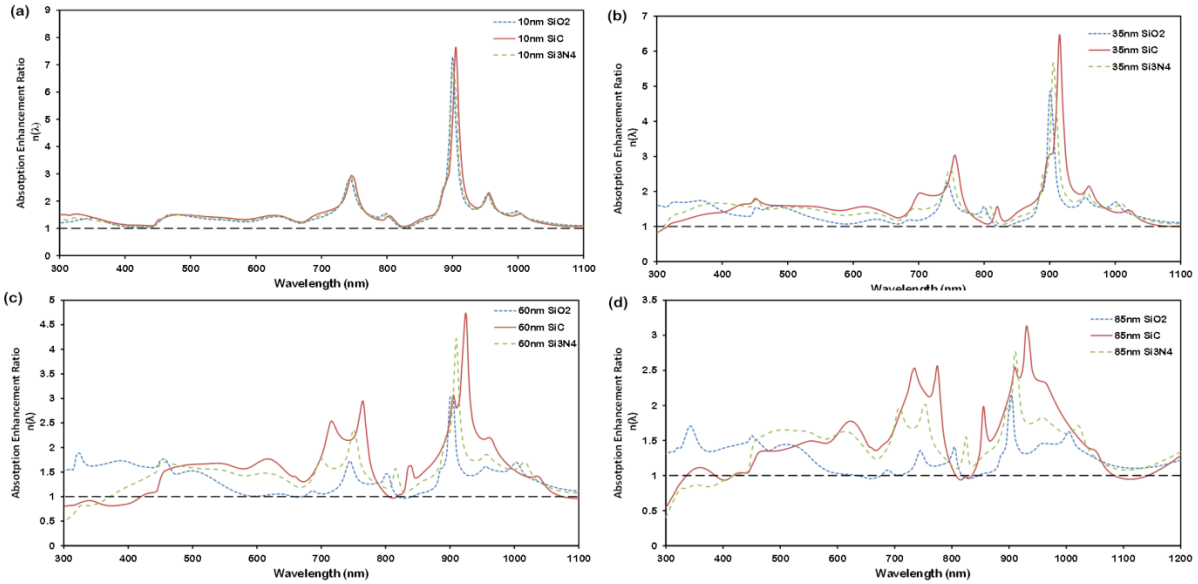

Figure 5-14. Calculated External Quantum Efficiency (EQE) for different spacer dielectric thickness and materials for 200nm diameter Al nanoparticles array with 250nm inter-particle distance on top of 300nm ncSi:H active layer.

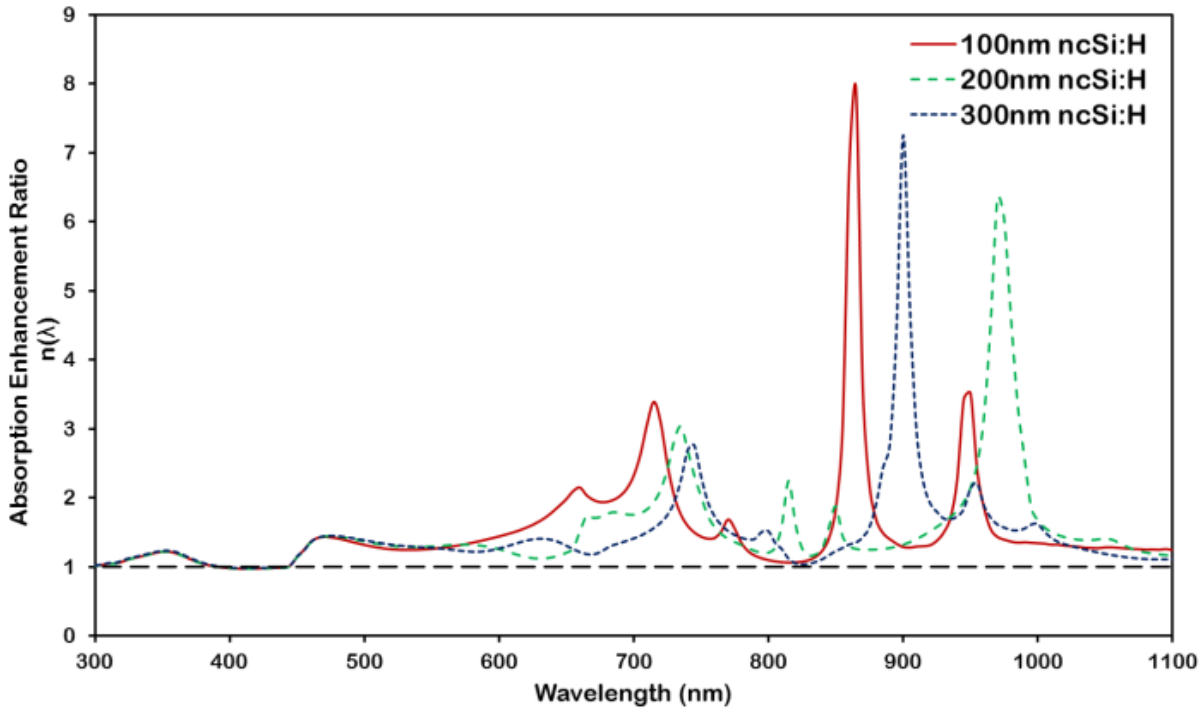

Figure 5-15. (a) Absorption Enhancement Ratio variation with wavelengths for Al nanoparticle arrays, which have a 200nm diameter and 250nm inter-particle distance on top of solar cell with 10nm SiO_2 as dielectric spacer and three distinct active ncSi:H thickness.

As shown in Figure 5-15, which depicts the area beneath the absorption spectrum curve, total absorption generally reduces by decreasing the active layer thickness. However, it reveals that absorption enhancement happens more intensely within the thinner ncSi:H layer. This code is related to the increasing density waveguide mode for specific wavelength, as thickness decreases. Additionally, absorption enhancement at a longer wavelength is more effective for a thinner absorber, as shown in Figure 5-15.

These conditions make absorption enhancement for thinner layers higher, in comparison to thicker layers. The calculation below shows that a nanoparticle array increases the absorption in 100nm ncSi:H by 44.5%, in 200nm ncSi:H by 35.9%, and in 300nm ncSi:H by 31.9%.

5-3-1-4. Effect of metallic object shape

To finalize parameterization realization, the effect of metallic object shape on absorption properties of 300nm-ncSiH/10nm-SiC solar cell is investigated. Figure 5-16 summarizes the total absorption ratio (P_{abs}) in 300nm-ncSi:H absorber layer (Figure 5-16 (a)), total reflection ratio from the surface (Figure 5-16 (b)), and total absorbed power inside of metallic array (Figure 5-16(c)). The absorption enhancement ratio in Figure 5-16(a) shows that nanoparticles have better overall performance. The strong absorption enhancement ratio at wavelength 750nm and 905nm with higher absorption over wavelength 450nm-700nm shows that nanoparticles comparing to nanosemispheres and nanodisks have stronger forward scattering and more efficient broadband absorption which caused better performance enhancement.

Investigating the total reflected power and total absorbed power in metallic architect reveals that most part of the incoming light will be reflected back by nanosemispheres versus in nanoparticles and nanodisks most part of the incoming light will be absorbed in metallic nanoparticles array. Surface modification of nanosemispheres for reducing power reflection would be a solution to increase the forward scattering of light for these structures to take advantage of their lower power absorption.

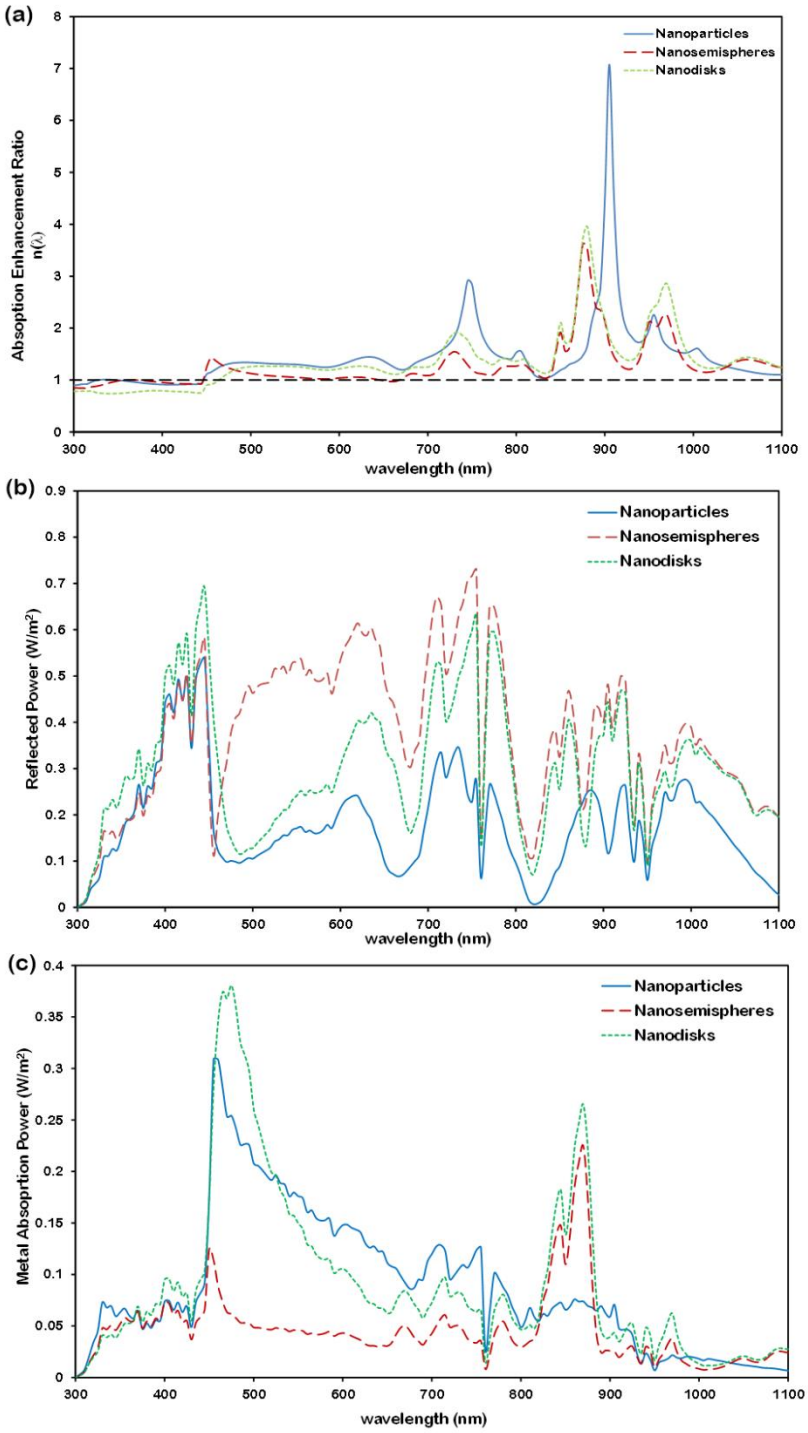

Figure 5-16. Effect of nanoparticle shape array on, (a) absorption ratio variation with wavelength, (b) reflection ratio spectrum, and (c) absorption ratio in metallic array. Array parameters are 200nm diameter Al nanoparticle with 250nm inter-particle distance (nanoparticles), 200nm diameter Al nanosemispheres with 250nm inter-particle distance (nanosemispheres), and 200nm diameter Al nanodisks with 100nm long and 250nm inter-disk distance.

5-4. Summary

The novel contribution of this research, nanoplasmonic architectures for ultra-thin film solar cells, is presented further more in this chapter by investigating the key design criteria and analyzing device optical performance accordingly. In addition, re-establishment of certain design parameters for nanoplasmonics in ultra-thin film solar cells is further discussed. The role of nanoplasmonics in solar cells introduced and treatment mechanism to incorporate them in photovoltaic devices discussed. The main focus is to evaluate design criteria for enhanced absorption in a-Si thin and ultra-thin film through designing a proper nanoplasmonic metallic structure. For this approach, the shape effect (size and type), type of dielectric, and type of metal are optimized to achieve maximum optical absorption.

New cell architectures have been designed incorporating nanoplasmonic structures with the purpose of further trapping the light in devices especially with thin absorber layers. Plasmonic nanostructures contribute to enhanced absorption in solar cells by (i) metallic nanoparticles as sub-λ scattering objects placed at the absorber surface scatter incident light into a distribution of angles through light-folding, increasing the optical path length within the absorber; (ii) creating propagating waveguide modes inside the thin absorber; and (iii) metallic nanostructures creating high near-field intensities associated with surface plasmon polaritons propagating at the metal/semiconductor interface. Numerical simulations carried out (using FDTD Solution software) underline the strong potential of nanoplasmonic metallic structures to further enhance the performance of ultra-thin solar cells for transparent and BIPV applications. The simulation results show the overall 30-35% percent increase in absorption efficiency for ultra-thin film silicon (150-100nm thickness) is possible by incorporating appropriate nanoplasmonic metallic array architecture.

Chapter

6

Nanoplasmonic Metallic Architect Development for Ultra-Thin Film Nanocrystalline Silicon Photovoltaics

Two light trapping techniques based on metallic nanoplasmonic structure are proposed for the performance enhancement in ultra-thin film nanocrystalline silicon solar cells. Different fabrication techniques for the development of nanoplasmonic metallic array will be investigated, based on the large area production and cost efficiency.

6-1. Nanoplasmonic fabrication: metallic nanoparticle array

Fabrication of nanoplasmonic architecture is the next step after developing design architectures and thin film device. As elaborate in the chapter 5, metallic nanoparticle arrays are the promising candidate for performance enhancement in ultra-thin film devices. In this chapter various fabrication techniques will be discussed and one method chosen, based on its application for large area production and cost effective parameters. By considering the shape target which is based on the patterned array of nanoparticles, nanodisks, and nanosemispheres, the following techniques exists:

1) **Electron Beam Lithography (EBL):**

   As a top-down nanofabrication technique, EBL is a well-known method for nanoplasmonic fabrication. It was among the first techniques used to develop nanoplasmonic architecture by Krenn and et al. [108]. The main advantage of this technique is its accuracy in creating of structures at nanoscale (`10nm). The primary reason for using this method is to observe and manipulate, by experiment, the simulation optimization results in fabrication.

   Metal nanoparticle arrays, hexagon and triangle patterned grid nanostructures, and nanodisks array structures are the main goal to use this technique for fabrication. The

control of array geometry plays an essential role in the light trapping mechanisms of these designs. While this method permits a large degree of control, it is impractical to use over a large scale [109]. To address these challenges in array fabrication, other methods—like the templating method—will be evaluated. Figure 6-1 shows the EBL fabrication steps.

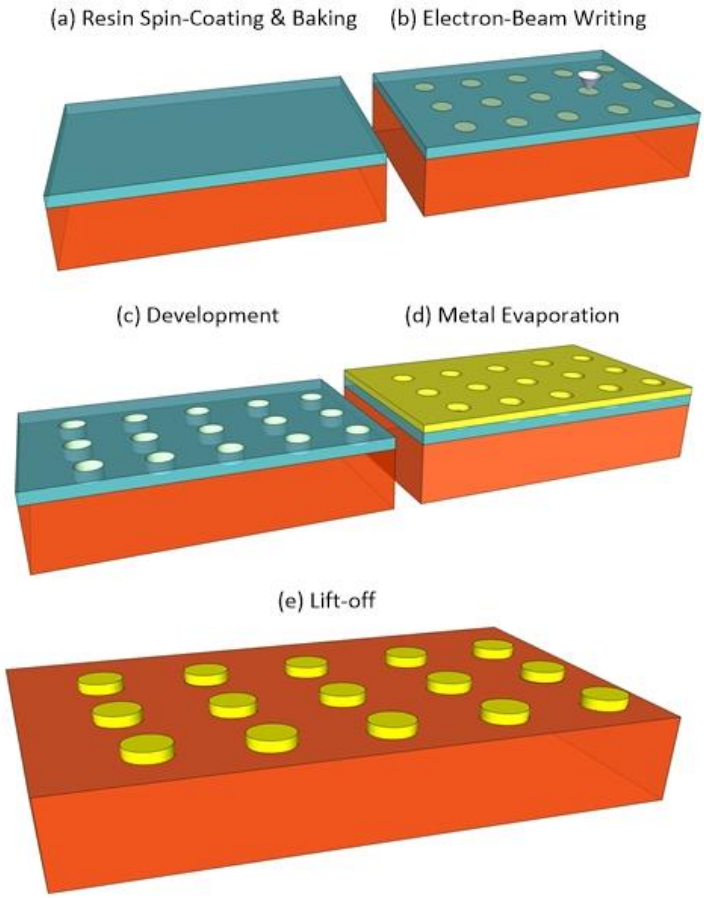

Figure 6-1. Main fabrication step for EBL. Some of the steps are similar to photolithography [110].

2) Nanosphere lithography (NSL) for fabrication of nano-hole patterned grid:

Nano-sphere lithography is one of the most advanced processes for nanostructures. It can easily make large-area periodic nano-sphere arrays with self-organized polystyrene (PS) or Silica nano-spheres. It is a low cost and simple technique for large-area periodic nanoparticle arrays as well. The effect of the spin-coated speed, substrate temperature, and clean method on the nano-sphere arrays is going to be investigated for the proposed application [109].

Figure 6-2 represents a schematic outline of this technique for two different array structures: nano-hole patterned grid and nano-disk/nanosemisphere metallic array. For a metallic object array, a monolayer of close-packed polystyrene (PS) nanospheres is formed on a metal-coated glass substrate. Successive O_2 RIE and Ar reactive iron etching (RIE) morphed the monolayer into an array of separated nanoellipses, and selectively etched a portion of the metal film that is not protected by the nano-ellipses. Ordered metal nanodisk arrays are produced on the substrates after removing the remaining PS. Further thermal annealing of the obtained structure will change it to the metallic nanosemispher/nanosemiellipse arrays, due to the surface tension between metal-substrate. For a nano-hole patterned grid, the process looks the same as above, the only difference is the substrate that is not coated with metal until after PS coating and etching. After PS removal through sonication, the remaining structure will be an array of a nano-hole patterned grid.

3) Templating method for metal nanoparticle fabrication:

The main idea in this technique is to use a template during normal thin film deposition through eBeam evaporation or sputtering metal deposition. One of the best templates for this purpose is the anodic aluminium oxide (AAO) template. Anodizing aluminum in an acidic solution, which forms a regular array of pores separated from the aluminum substrate by a thin oxide membrane at the bottom of these pores. This regular hexagonal array occurs as a result of repulsive forces between neighboring pores as the aluminum is oxidized, and the ensuing structure can be used as a template for fabricating regular arrays of nanoscale structure. The parameters of these arrays can be controlled by the pH of the solution and the voltage used during anodization [109].

In addition, templates with controllably varied pitch and diameter have been fabricated with this technique. Specifically, it is possible to fabricate the through-hole membrane with anodizing and subsequent etching, which can then be utilized as a template whereby metal is evaporated to produce regular arrays of nanoparticles. In Figure 6-3, a flow chart outlines the fabrication step for AAO templates.

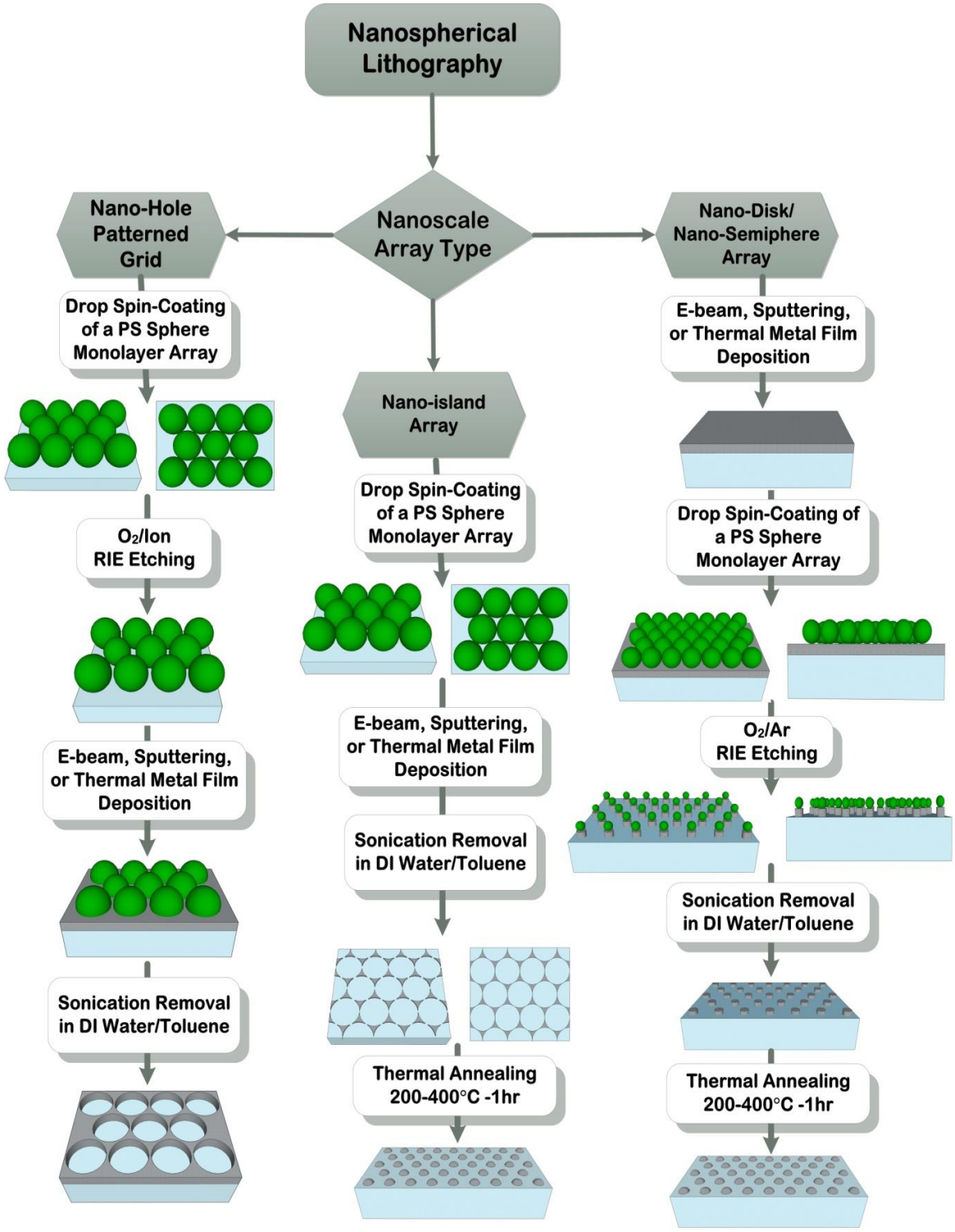

Figure 6-2. Fabrication of a nano-hole pattern array and nano-disk/nano-semisphere array on substrate by nano-spherical lithography.

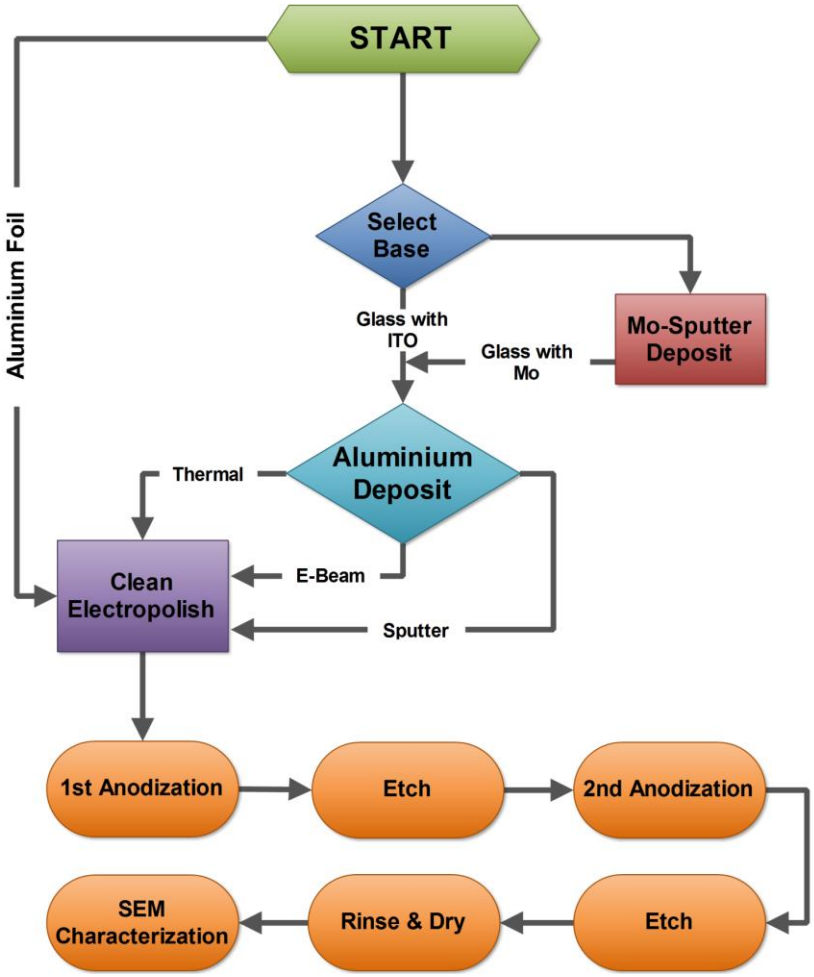

Figure 6-3. AAO fabrication steps flow chart.

4) Other methods:

There may be other methods to produce an array of nanoparticles. The topmost reason for exploring another method is that all three techniques, previously discussed, have one big disadvantage: infeasibility for large-scale production. One possible method entails the evaporation and subsequent annealing of a thin film metal deposited on substrate to create a metallic nanoisland. This technique, known as nano-sized stochastic textured surface (NSTS), has the advantage of ease with the moderately uniform distribution of metallic object at large scale. However, a notable disadvantage is its non-uniform shape and size of features. Figure 6-4 depicts a sample of Ag nanoisland formation on a 4-inch glass wafer through thin film eBeam evaporation and annealing at 200°C for 1 hour, as evidence for this proposed method.

A second possible method for metal nanoparticle array fabrication is the deposition of a colloidal suspension of metal nanoparticles in a monolayer on the substrate, which causes an array with uniform diameters with non-uniform pitch.

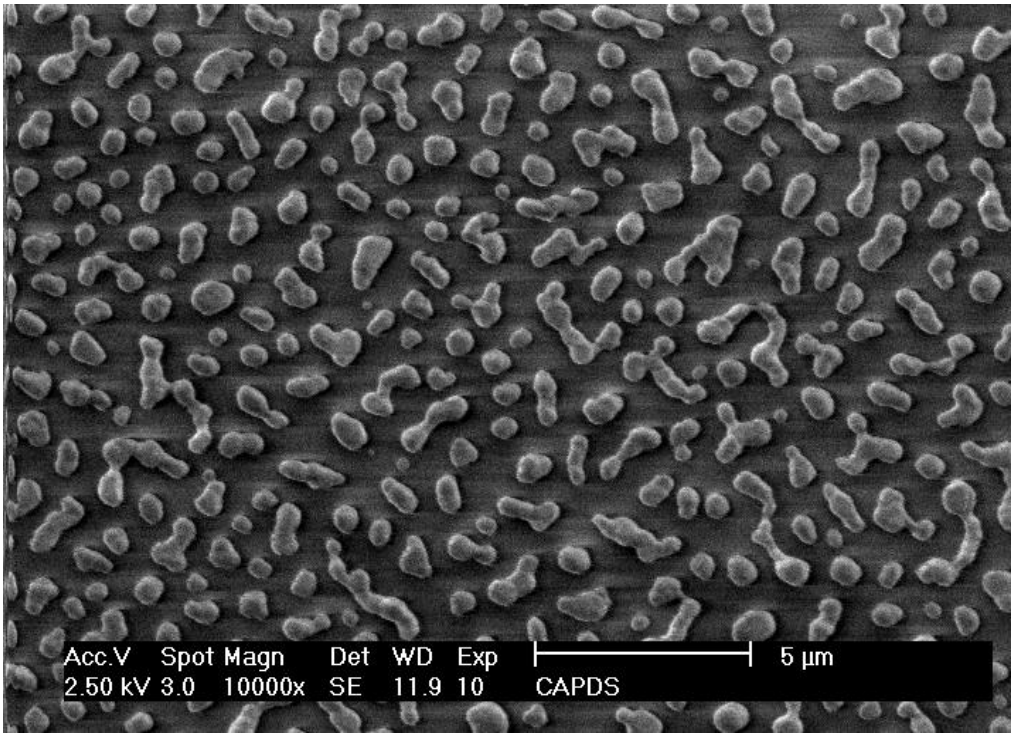

Figure 6-4. Ag nanoisland formation after thin film evaporation and annealing through NSTS technique.

6-2. Metallic Nanoparticle Array through Nano-sized Stochastic Textured Surface (NSTS) Fabrication

In this section, experimental work for the fabrication of metallic nanoparticle array through the NSTS technique is discussed. Figure 6-5 shows, in a simple sketch, the fabrication procedure for metallic nanoparticle array formation through NSTS. Chapter 5 addressed the viability of inserting these metallic nanoparticle array into AZO. Accordingly, the first step is the deposition of AZO through sputtering.

For this purpose, a 4-inch glass wafer was first thoroughly cleaned through RCA1 and rinsed with aceton, IPA, and DI Water. Afterward, 700nm AZO was deposited on glass using parameters achieved for best AZO performance, as demonstrated in section 3-2. Following AZO deposition,

sheet resistivity of the AZO film was measured using the four-probe technique, as discussed in section 3-2-1. Again, following AZO deposition, the AZO coated glass wafers were loaded into the eBeam evaporation chamber for metal thin film deposition. Once a base pressure within the 10^{-7} Torr range is reached, a thin Ag film was deposited at different thickness. Then, metallic thin film deposition samples were removed from the eBeam chamber and placed in a glass-cube chamber equipped with a gas ventilation system, and in a cube furnace to establish an inert gas annealing environment. Annealing was subsequently carried at 280°C for 1 hour, and the sample was left in the furnace with Ar gas ventilation to cool down for 3 hours.

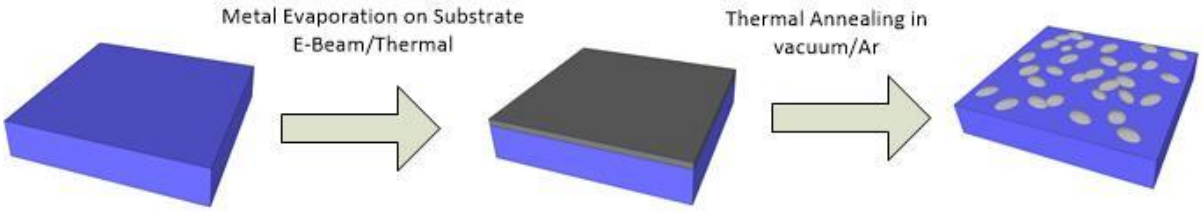

Figure 6-5. A schematic process used for NSTS fabrication. It mainly involves deposition of metallic film (E-Beam evaporation or thermal evaporation) accompanied by thermal annealing in controlled atmosphere.

6-2-1. Results and Discussion

Figure 6-6 shows the evolution of developed NSTS structures through e-Beam deposition of Ag thin film on 700nm AZO coated 4inch glass wafer at different thicknesses. The constant annealing temperature of 280°C was chosen based on the maximum deposition temperature of AZO and ncSi:H thin film solar cell. It was revealed that by annealing the AZO thin film in temperature higher than 300°C the sheet resistivity of AZO increased. This could be attributed to the oxygen existence in the annealing furnace and its partial pressure effect on the change of oxygen vacancy in the deposited AZO. Therefore, as a preventative measure, a constant annealing temperature of 280°C was used to avoid increasing AZO sheet resistivity.

Figure 6-6 reveals that by increasing the e-Beam deposited Ag thin film thickness, the formation of Ag nano-island dramatically changes in structure. First, at 8nm thickness, a distribution of very small (average below 10-20nm) Ag nanoparticles are observed. By increasing the Ag thickness, the size of the distributed Ag nanoparticles and their inter-particle distance is increased. Since the main purpose for the nano-island formation is to create a structure close to the simulation result, image analysis by

ImageJ software was carried out on the SEM results to characterize Ag nanoparticle size distribution and coverage.

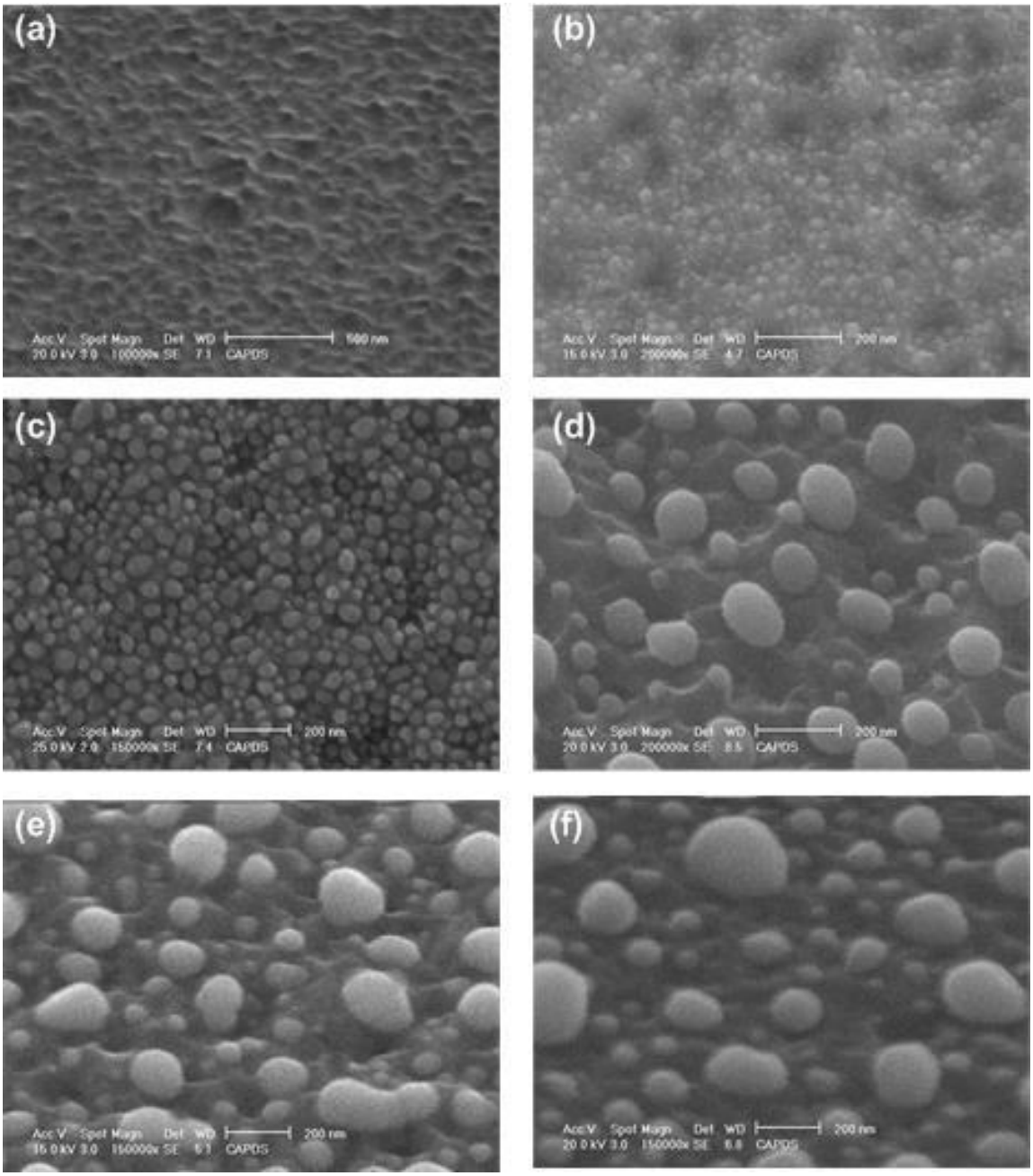

Figure 6-6. SEM images of a) bare 700nm AZO coated glass wafer and Ag thin film coated on 700nm AZO coated glass at 280°C for 1hr with different thickness, b)8nm, c)12nm, d)20nm, e)24nm, and f)28nm.

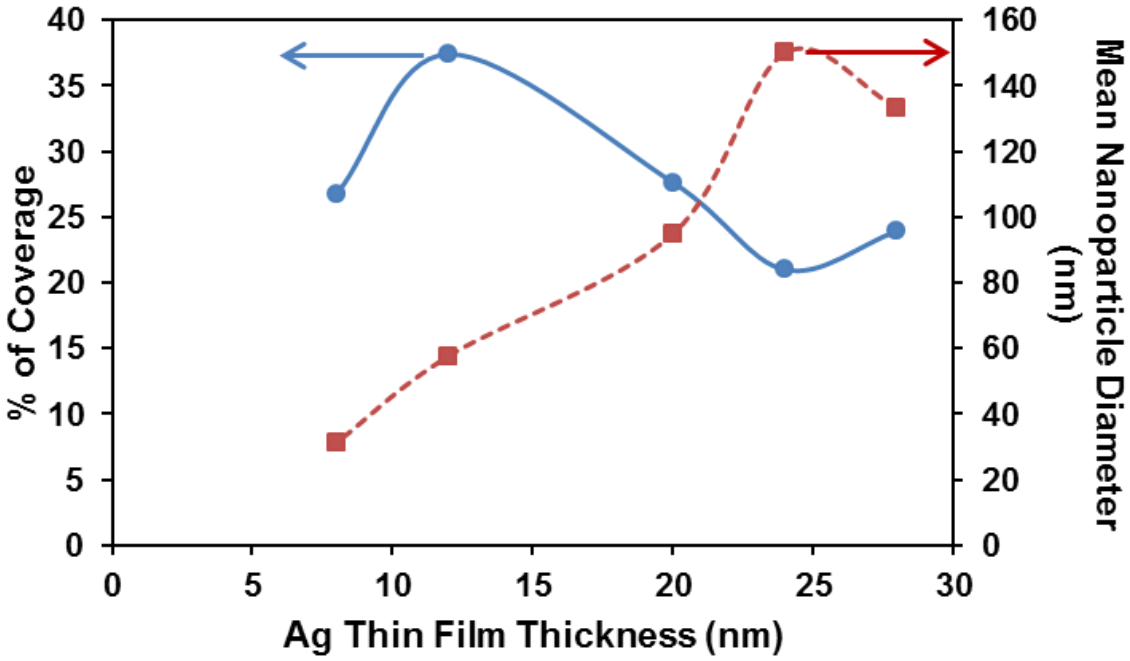

Figure 6-7. Mean Ag nanoparticle diameter and percentage of covered area at different Ag thin film thickness

As demonstrated in Figure 6-7, by increasing thin film thickness from 12nm to 24nm, the area coverage of nanoparticle decreased and, in parallel, the mean nanoparticle diameter of Ag nano-island increased. By further increasing the thickness of Ag thin film, the area coverage starts to increase and, at the same time, the mean diameter of Ag nano-island starts to increase. It is clear that to reach the maximum performance area of nano-island, which is approximately 200nm, and along with the mean coverage area, the best Ag thin film thickness should be around 24nm.

Figure 6-8 shows in more detail the histogram size distribution of Ag nano-island formation, which occurs due to the annealing of different Ag thin film thicknesses at 280°C for 1 hour. By increasing the thin film thickness from 12nm to 28nm, the average nano-island size increases. The sample principle applies to the increase of Ag thick film thickness above 24nm, although some large nanoparitcles above 200nm is observable bearing a dominant size distribution between 50-100nm.

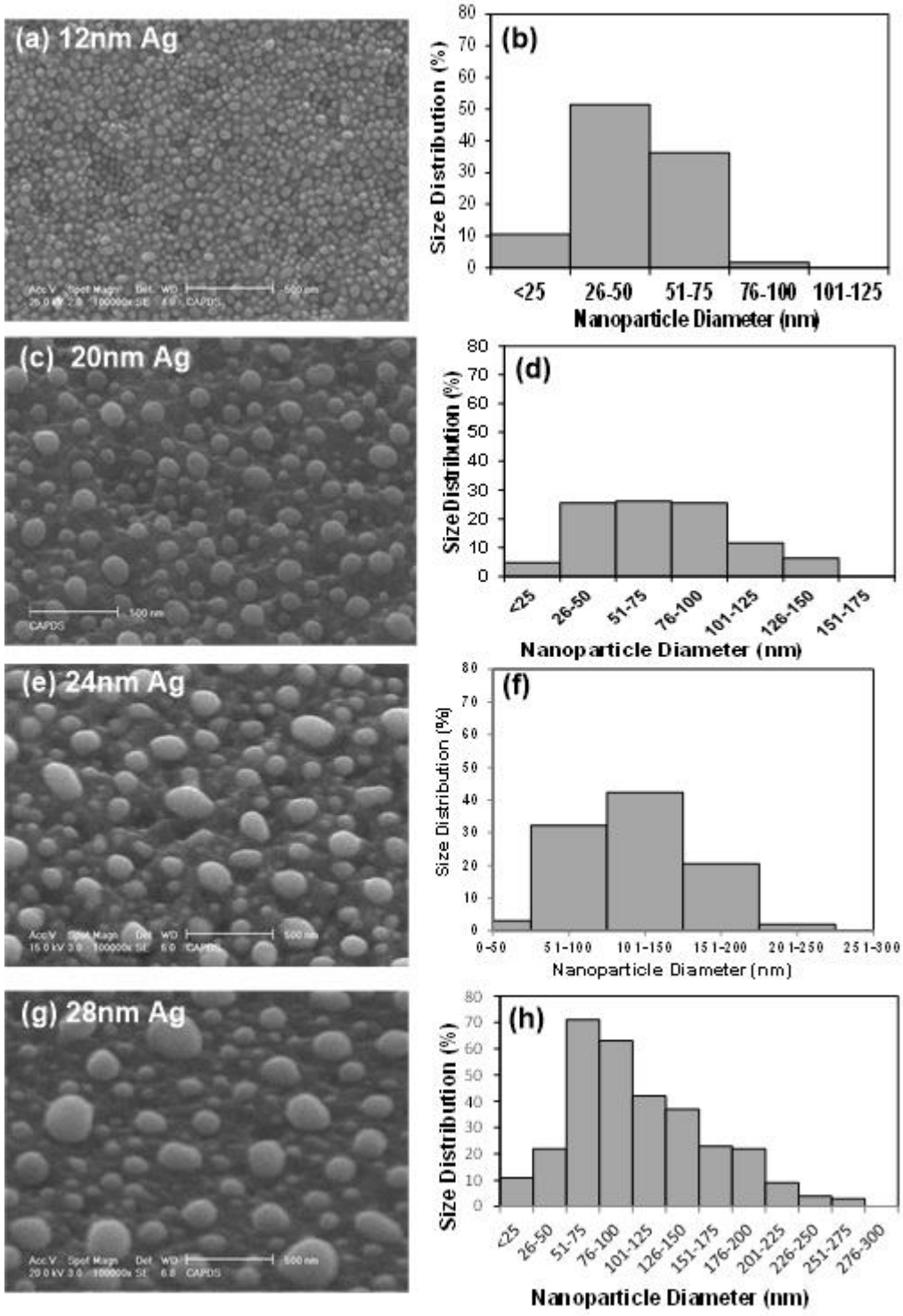

Figure 6-8. Nanoparticle size distribution of Ag thin after thermal annealing at 280°C for 1hr for different thin film thickness, a,b) 12nm, c,d)20nm, e,f)24nm, g,h)28nm.

Given that the existence of small (diameter below 100nm) and aggregated nanoparticles and relatively high surface coverage (>25%) lead to undesired parasitic absorption loss and weak scattering [111] [45] , it may be concluded that an efficient Ag thin film thickness of roughly 23-25nm will achieve maximal performance in nano-island distribution. By increasing the thin film thickness from 12nm to 28nm the average nano-island size increases. Additionally, by increasing the Ag thick film thickness above 24nm although some large nanoparticles above 200nm is observable but the dominant size distribution is between 50-100nm. To further investigate the effect of Ag nano-island on the AZO, the transmittance and reflectance measurement of pure glass, Glass/750nm AZO and glass/750nmAZO/22nmAg heat treated at 280°C for 1hr are provided in Figure 6-9.

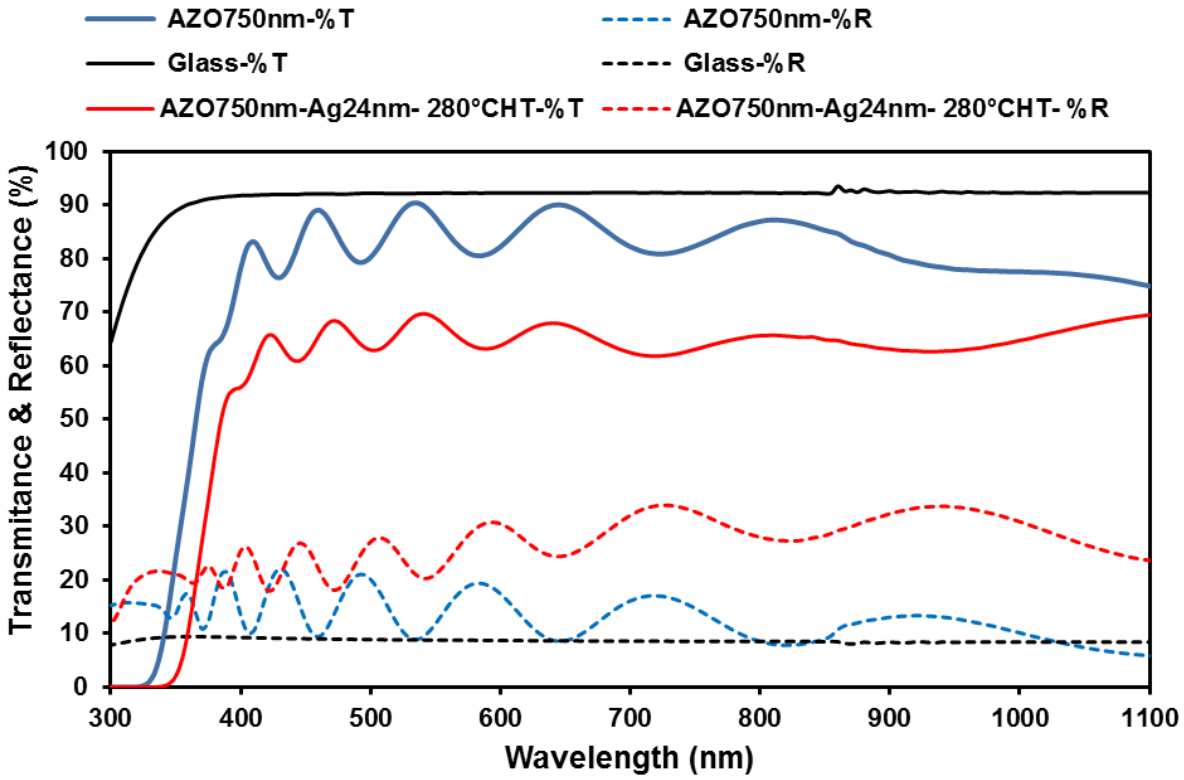

Figure 6-9. Transmittance and reflectance spectra of the Glass, Glass/750nmAZO, and Glass/750nmAZO/22nmAg HT at 280°C 1hr.

It shows that the presence of Ag nano-island reduces the transmittance of AZO film by 20-22% and also increases the reflectance by 10% at visible range and around 15% at IR wavelength. Considering that the existence of small (diameter below 100nm) and aggregated nanoparticles and relatively high

surface coverage (>25%) are lead to undesired parasitic absorption loss and weak scattering [112][113].The ramification of the results reveals that in order to get the best performance nano-island distribution, efficient Ag thin film thickness is round 23-25nm.

To further elaborate the effect of the nanoplasmonic architect, an AZO thin film with embedded Ag nano-island (referred as nanoplasmonic AZO) is prepared with different Ag thin film thickness. For these samples first 700nm AZO deposited on top of glass accompanied by deposition of Ag thin film and heat treatment at 280°C for 1hr followed by deposition of 30nm AZO on top, as shown in Figure 6-10.

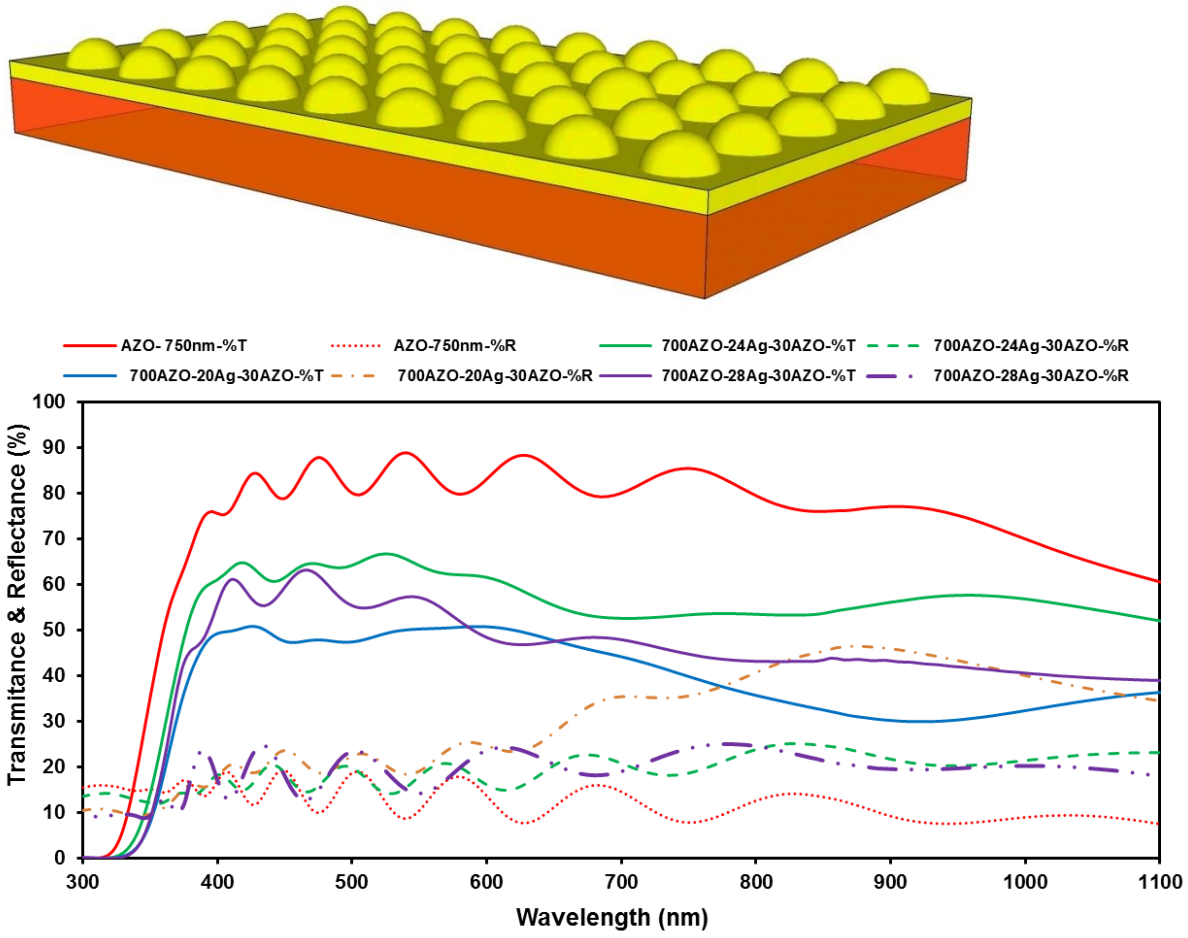

Figure 6-10. a) a schematic illustration of 700nmAZO-Ag nano-island-30nm AZO film. B) Trasnmittance and Reflectance spectra of nanoplasmonic AZO as (a) with different Ag thin film thickness.

These results are important in the evaluation of the possible application of the nanoplasmonic AZO for the performance enhancement of developed ultra-thin film nanocrystalline silicon solar cells. By

increasing the Ag thin film thickness from 20nm to 28nm, the overall transmission of nanoplasmonic AZO increased and shows its maximum value at 24nm. These results are in accordance with the simulation and size distribution results shown in Figure 6-8.

Also, the transmission results indicates that at 20nm thin Ag film, the formed nanoplasmonic Ag nano-island has higher reflection at IR region, makes it a suitable candidate for back reflector. For this reason, using nanoplasmonic structure as a back reflector (BR) is also investigated [114].

6-3. Nanoplasmonic ultra-thin film solar cell development

The last step in this research is the implementation and integration of all the obtained results for developed ultra-thin film nanocrystalline solar cell with the nanoplasmonic AZO layer. For the final device architect 2 structures were developed: 1) Nanoplsamonic AZO as front contact in superstrate device architect, and 2) Nanoplasmonic AZO as back contact in substrate device architect, as fabrication process is shown in Figure 6-11.

For the Ag nano-island NSTS process, 24nm Ag thin film was used as concluded in section 6-2. For the cell construction sample 45 was used as the reference cell. For the performance comparison, external quantum efficiency and current-voltage measurement were carried out.

The EQE results of the prepared samples s are summarized in Figure 6-12. In both nanoplasmonic cells the EQE increased. Although, different mechanisms involved in the external quantum efficiency enhancement. In the substrate structure, using nanoplasmonic structure in front contact, the main enhancement occurred at higher wavelength, above 600nm and at lower wavelength the EQE decreases. This could be attributed to the effective mechanism of forward scattering of the structure for longer wavelength, but at the same time parasitic absorption in metallic Ag is reduced the EQE.

On the other hand, in the superstrate structure, using nanoplasmonic structure in back contact, the main enhancement occurred at lower wavelength, below 600nm. However, still a minor performance improvement at higher wavelength still observed. This can be attributed to the enhancement due to increased reflectivity in general.

Top and bottom contact sputtering condition with the PECVD deposition condition for the ultra-thin film p-in solar cell for the nanoplasmonic structure is summarized in Table 6-1.

Table 6-1. Depositing condition for nanoplasmonic ultra-thin film samples

Samples			Nanoplasmonic superstrate	Nanoplasmonic substrate	AZO/p-i-n/AZO
AZO			700nmAZO/24nmAg /50nmAZO	AZO-750nm	AZO-750nm
AZO/p-layer			AP3-120s	AP3-120s	AP3-120s
p-ncSi:H	**Pressure**	**mT**	150	400	400
	Power	**W**	45	50	50
	Gas Ratio	**SiH_4:H_2:B_2H_6**	2:300:14	2:400:14	2:400:14
	Temperature	**°C**	260	260	260
	Thickness	**nm**	25	25	25
p/i buffer layer			PI2	PI2	PI2
i-ncSi:H	**Pressure**	**mT**	600	600	600
	Power	**W**	7	7	7
	Gas Ratio	**SiH_4:H_2**	4:20	4:20	4:20
	Temperature	**°C**	300	300	300
	Thickness	**nm**	150	150	150
n-ncSi:H	**Pressure**	**mT**	600	600	600
	Power	**W**	10	10	10
	Gas Ratio	**SiH_4:H_2:PH_3**	2:200:20	2:200:20	2:200:20
	Temperature	**°C**	300	300	300
	Thickness	**nm**	40	40	40
AZO			AZO-750nm	50nmAZO/20nmAg/ 700nmAZO	AZO-750nm

The external quantum efficiency of fabricated nanoplasmonic cells are summarized in Figure 6-12. It shows that both nanoplasmonic architects caused an enhancement in the EQE for long wavelength above 600nm. This increase in the EQE at ling wavelength is more dominant for superstrate structure, however a significant reduction in the EQE is also observed for wavelength below 600nm compare to normal sample. This reduction can be attributed to the increased of reflection in superstrate sample, since the nanoplasmonic structure is implemented on top of emitter layer (p-layer) and also due to the parasitic absorption of Metallic Ag at lower wavelength.

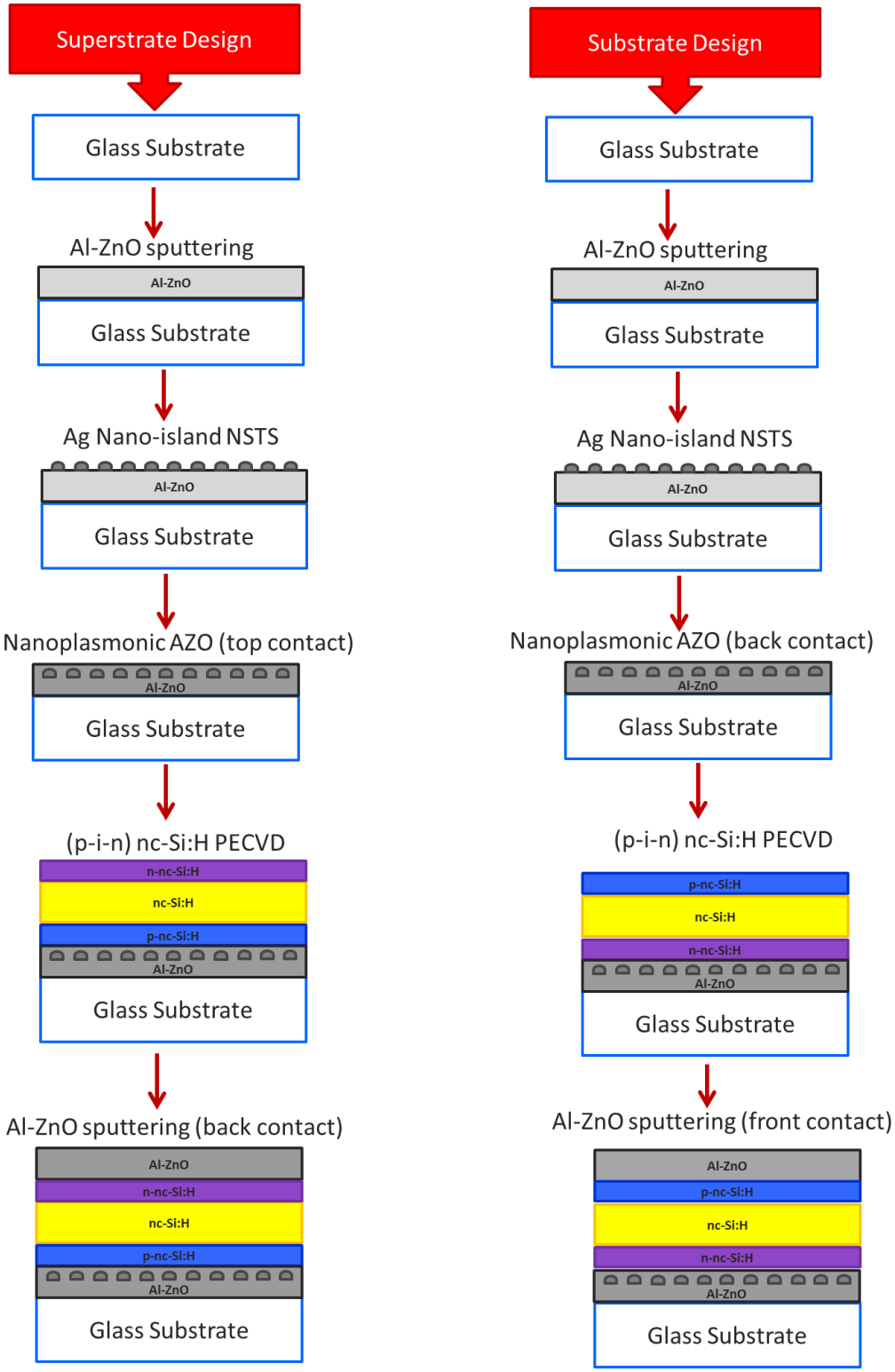

Figure 6-11. Schematic device architectures and fabrication process flow for the proposed nanoplasmonic ultra-thin film solar cells.

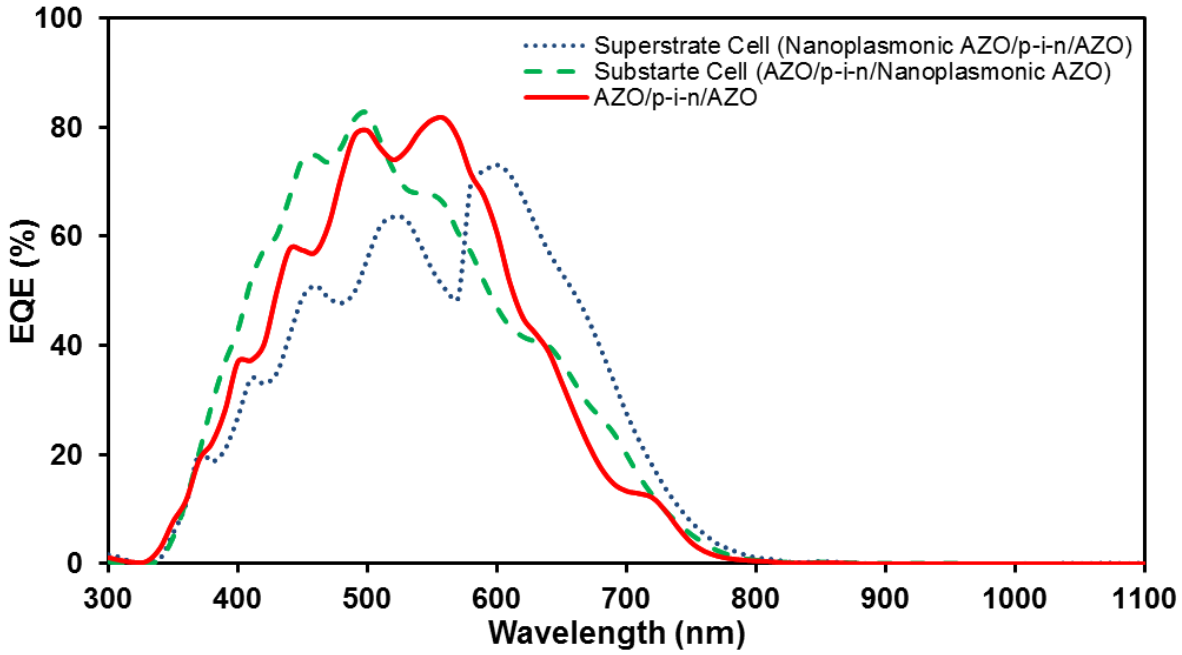

Figure 6-12. Effect of Nanoplasmonic AZO architect on front contact and back contact cell compare to normal AZO/p-i-n/AZO cell.

To further investigate the effect of nanoplasmonic substrate cell structure the EQE curves and the total device absorption percentage (defined as the hundred minus the total reflectance from the device, 100-R) of prepared samples are shown in Figure 6-13. Compared to the normal cell, nanoplasmonic substrate cell shows 2 distinct enhancements, for visible range from 380nm-520nm and for longer wavelength from 620nm-800nm respectively. Total absorption of incident light does not change for substrate nanoplasmonic cell compare to normal cell, as the calculated Jsc from EQE showed. The Jsc of normal cell and nanoplasmonic substrate cell are 16.22 mA/cm^2 and 16.06 mA/cm^2 respectively. This may be due to the lower absorption at the wavelength of 520nm-620nm for the nanoplasmonic structure, which can be attributed to the parasitic absorption of Ag nanoplasmonic structure.

The EQE results highlight that the proposed nanoplasmonic structure has better performance as a back reflector (BR) instead of using in front to enhance forward scattering and local intensity of light due to plasmonic structure.

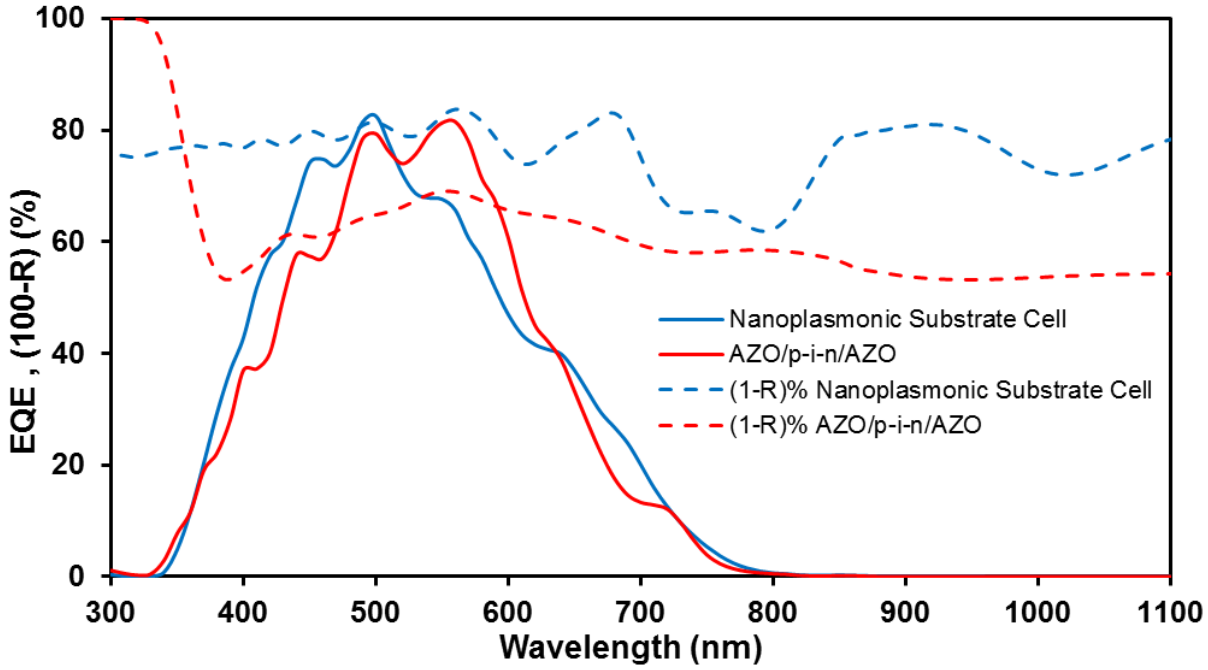

Figure 6-13. The EQE curves and total device absorption (1-R) of the normal (AZO/p-i-n/AZO) and nanoplasmonic substrate cell.

To evaluate the overall light trapping effects, the photocurrent characteristics of prepared samples are presented in Table 6-2.

Table 6-2. I-V characteristics of normal cell (AZO/p-i-n/AZO), superstrate nanoplasmonic cell, and substrate nanoplasmonic cell

Samples		Nanoplasmonic Superstrate cell	Nanoplasmonic Substrate cell	AZO/p-i-n/AZO
Voc	**mV**	776	801	705
Jsc	**mA/cm²**	13.55	16.1	16.22
Efficiency	**%**	5.3	5.82	5.3
FF	**%**	50.4	45.13	46.35
Rsh	**Ω**	2200	2800	940
Voc Slope	**-**	160	110	59

The nanoplasmonic substrate cell has a moderate surface roughness due to the presence of Ag metallic nano-island that might contribute to the light trapping as well. Thus one can argue that the performance boost in nanoplasmonic substrate cell may be due to the roughness induced light scattering and not mainly due to plasmonic effect. However due to the size distribution of

metallic nano-island which is at the range of 100-125 nm considering semi-sphere distribution, the light trapping is mainly attributed to the plasmonic light scattering as in other works reported as well [115].

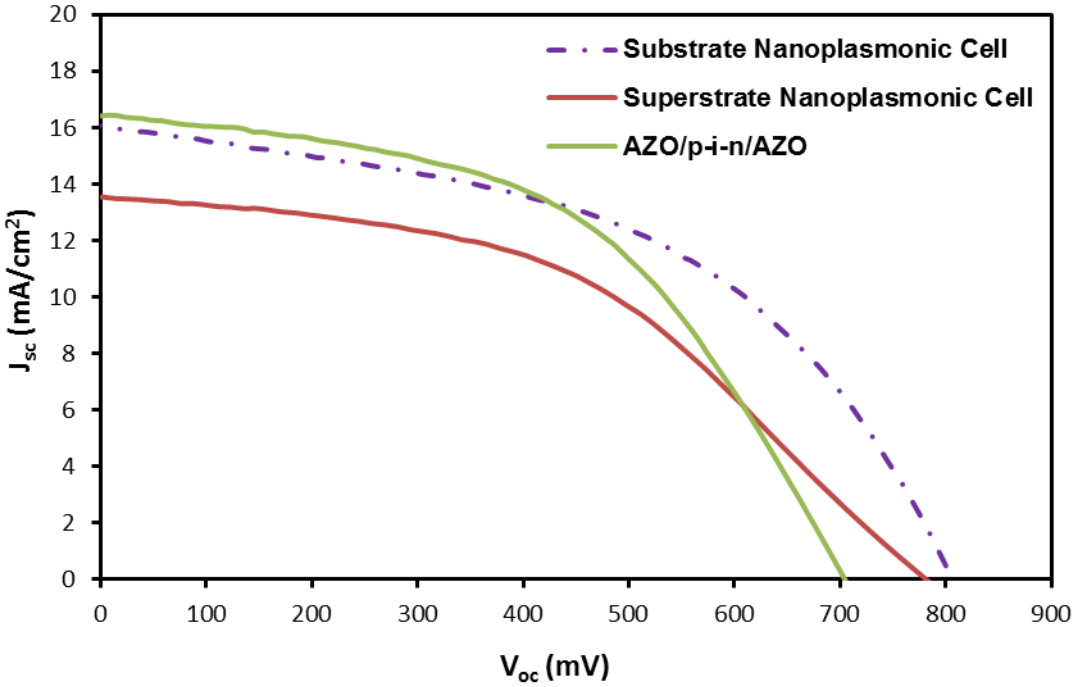

Figure 6-14. The I-V curves of the normal sample (AZO/p-i-n/AZO), substrate plasmonic cell, and superstrate plasmonic cell.

It also should be highlighted that by accommodating the metallic nanoplasmonic structure on the back of the solar cells, longer wavelengths are scattered and the radiation can be trapped more efficiently. The particle's geometry (or size) leads to a better/worse scattering efficiency (as shown in Figure 6-13). The more the amount of light scattered (it depends on the particle's geometry and size), the less the amount of light reflected (that is, light that follows the "straight path"). It can be concluded that the nanoplasmonic metallic array due to the broadband large scattering cross-section of Ag nano-island at the rear side can have a strong light scattering across the whole spectra for Ultra0thin film devices.

One other subject is to understand the differences between simulation results and the experiment. Different graphical configuration may be the reason of this difference. In a metallic nanoparticle array as simulated in chapter 5, there is a single contact point between the substrate and nanoplasmonic

structure, whereas in NSTA nanoplasmonic architect there would be a large contact area affecting the dipolar scattering pattern and would be in favor of backward scattering. Since different mechanism would be in effect in this scenario explanation of exact mechanism is not possible and the overall performance may be estimated through in-direct measurement of device performance as shown here.

Further investigation of the I-V curve reveals that the nanoplasmonic structure is also affecting the open-circuit as well. For both superstrate and substrate structure the Voc increased almost 10%. Additionally, the nanoplasmonic AZO increased the series resistance of the devices significantly, as the I-V curves data shows. In order to compare the series and shunt effect, dark I-V characteristic of prepared samples is measured as shown in Figure 6-15. It reveals that the nanoplasmonic structures increased the dark current and also for substrate configuration the shunt resistivity decreased.

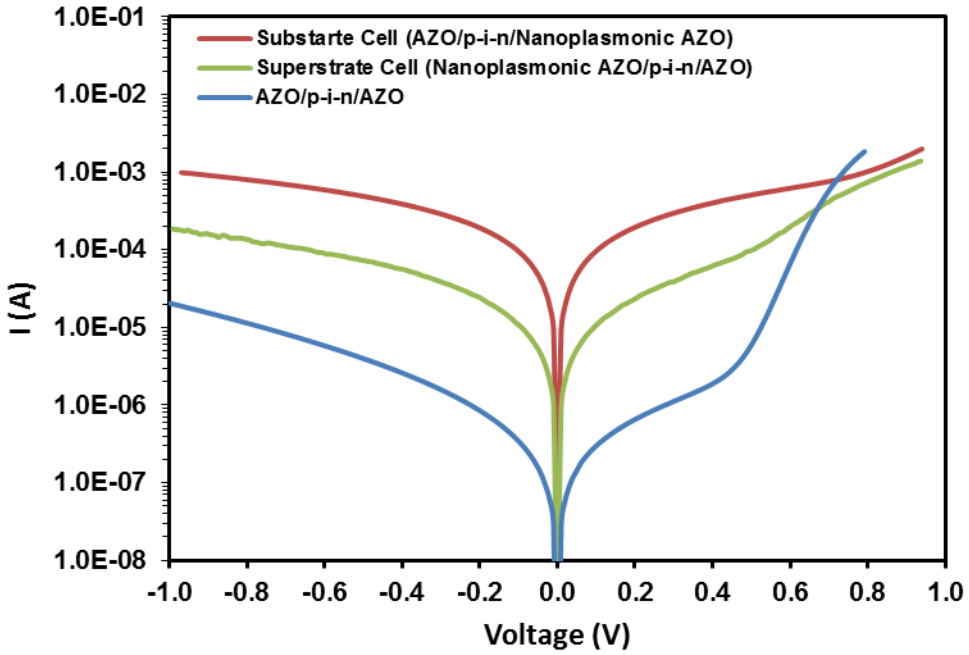

Figure 6-15. Effect of nanoplasmonic AZO on dark I-V characteristics.

This may be attributed to the effect of metallic structure and its interface with AZO think film in providing a recombination sites. Increase of dark saturation current after including the nanoplasmonic metallic structure in AZO is evident. To address series resistance, the sheet resistivity of AZO before and after including metallic Ag nanoplasmonic structure is measured by 4 probe technique. The sheet resistance increased almost 30% from 5.7 Ω/□ to 7.5 Ω/□.

Although the sheet resistance is still below 8 Ω/□, the acceptable range for transparent conductive layer, but this increase confirms the increase of series resistance in the I-V curve characteristic of final devices. In addition, considering that for effective near field enhancement, the nanoplasmonic structure positioned very close to the active device layers, which this also may provide a path for the recombination and increase of overall shunt current.

6-4. Summary

The ramification of device characteristics reveals that the overall effect of nanoplasmonic AZO on the device performance is a combination of effects which makes the performance enhancement complicate. By inserting nanoplasmonic structure on the final device the performance boost from near field enhancement and broadband scattering will be offset by introducing metallic recombination sites and also increasing the metallic backward scattering. To eliminate one of these setbacks the nanoplasmonic AZO may be used as a back reflector in this case, by utilizing the increase reflectivity we can see performance boost.

Chapter

7

Conclusions and Future Recommendations

7-1. Conclusions

In this PhD study a new effort for efficiency enhancement in thin film solar cells is investigated. To this advance, three main contributions area achieved:

1. *Development of optimized Al-ZnO as a transparent conductive oxide (TCO) application with enhanced conductivity and transparency*

   Electrical and optical properties of aluminum doped zinc oxide at different deposition power and pressure were studied. In order to systematically study the influence of deposition conditions on the film properties, modifications were made in-house on the commercial system: In order to enhance the heating capacity 3 sets of quartz-halogen lamp banks, 500W each, were installed in such a way they radiatively and uniformly heat the substrates.

   Al: ZnO with resistivity as low as $\rho=1.52\times 10^{-3}$ Ω.cm at deposition temperature of RT with stable electrical properties in air has been achieved. A steadily decreasing trend in resistivity was observed with increasing deposition temperature. At the deposition temperature of 250°C a resistivity of 2.94×10^{-4} Ω cm was achieved and this represents the lowest recorded resistivity for the AZO films. The carrier concentration significantly increased to a value of 1.07×10^{21} cm^{-3} for the deposition temperature of 250°C. The extracted mobility also showed an increasing trend with temperature. The ZnO:Al system undergoes a transition from metal-semiconductor to metal-like behaviour at increased deposition temperatures, and this transition is attributed to the competition between

thermally activated carriers and scattering effect of free carriers in a degenerate semiconductor. The light transmission in the visible range is above 85% for all the samples. However in the infrared region a systematic decrease in transmission was observed with increasing deposition temperature.

2. *Development of ultra-thin film nanocrystalline silicon solar cells*

In the second stage of this PhD work a p-i-n ultra-thin film nanocrystalline silicon solar cell is developed. For this purpose previously developed individual film (n-type nanocrystalline silicon film and p-type nanocrystalline silicon thin film) were used as the base. The device integration optimization is carried out to get the best performance individual semi-transparent ultra-thin film solar cells without using any metallic contact electrode finger to increase total sun access of the front side of the device.

New transparent nc-Si solar cell with p-i-n configuration is developed on glass substrates incorporating highly conductive aluminium doped zinc oxide (AZO) films as top and bottom electrodes. The main experimental processes involved, (i) development of a high deposition rate process in a modified PECVD system, (ii) optimization of doped and undoped micro and nanocrystalline Si layers at temperature 300°C, (iii) process development for AZO films by sputter deposition at low pressure and moderate power with enhanced conductivity and transparency, and (iv) process integration for single junction p-i-n device process on glass substrate. Additionally, highly conductive (17S/cm) n-type nc-Si:H (SiH_4, PH_3, 98% H_2 dilution) and p type nc-Si:H (SiH_4, B_2H_6 , 98.5% H_2 dilution) films have been developed at 300C.

To further improve the final device performance different buffer layers were developed for the AZO/p-ncSi:H and p-ncSi:H/i-ncSi:H interfaces. A slightly doped n-ncSi:H layer is used as the buffer layer for the AZO/p-ncSi:H interface to increase the working function of the interface and also to build up a barrier for boron diffusion and migration to the AZO due to the hydrogen plasma. In addition, an amorphous/nanocrystalline Si:H layer, with a lower hydrogen plasma rate is chosen for a buffer layer of p-ncSi:H/i-ncSi:H interface. Through lowering the band tails by creating a barrier for boron diffusion to i-layer during diffusion the shunt current reduces and the performance of the final devices improves. Table 7-1 shows the characteristic of the best performance fabricated device.

Table 7-1. I-V characteristic of the best performance ultra-thin film solar cells.

Area	Voc (mV)	Isc (mA)	FF (%)	η (%)
1 cm^2	704	16.42	50	5.79

3. *Nanoplasmonic architecture optimization for photovoltaics*

The concepts that have been achieved in this cutting edge research is to develop and investigate nanoplasmonic structures for light trapping enhancement in ultra-thin film devices. Design parameters for a novel plasmonic thin film nanostructured architecture for nc-Si:H solar cells was revealed. Major component of the developed structure is the design of a metallic nanoparticle array scatterer for the top of absorber, and investigate its utilization as a rear contact. Complete design details is investigated through comprehensive Finite-Difference-Time-Domain (FDTD) simulations. The know-how is established and developed for the use of nanoplasmonic nanostructures, and their heterostructures as the next generation solar cells.

It is shown that nanoplasmonic nanostructures contribute to enhanced absorption in solar cells by (i) metallic nanoparticles as sub-λ scattering objects placed at the absorber surface scatter incident light into a distribution of angles through light-folding, increasing the optical path length within the absorber; (ii) creating propagating waveguide modes inside the thin absorber; and (iii) metallic nanostructures creating high near-field intensities associated with surface plasmon polaritons propagating at the metal/semiconductor interface. Numerical simulations carried out (using FDTD Solution software) underline the strong potential of nanoplasmonic metallic structures to further enhance the performance of ultra-thin solar cells for transparent and BIPV applications. The simulation results show the overall 30% percent increase in absorption efficiency for ultra-thin film silicon (150-100nm thickness) by incorporating appropriate nanoplasmonic metallic array architecture. The effect of Al, and Ag as a plasmonic metals was compared and it was shown that Al and Ag has overall comparable performance for light-trapping over a broad range of the solar spectrum, especially for wavelengths which are favorable for transparent solar cell. However, the selection of type of metal is depending on the

application, since Ag shows parasitic absorption at lower wavelength near visible light which is affecting its application.

4. *Nanoplasmonic ultra-thin film device integration*

   Metallic nanoparticle array development through Nano-sized Stochastic Textured Surface (NSTS) fabrication technique is investigated for large area development. The main reason for choosing this method is its compatibility for low cost development at large scale. Optimized Ag nano-island is developed by controlling the thickness of e-Beam deposited Ag thin films on a four inch glass wafer. The developed layer was used as the nanoplasmonic structure and sandwiched in the Al-ZnO layer of previously developed thin film p-i-n devices as explained in chapter 4.

   Two different device architecture is used, nanoplasmonic AZO on back as superstrate, and nanoplasmonic AZO on top as substrate device configuration. Different device characterization is used to evaluate the performance. It is demonstrated that nanoplasmonic AZO has more effective performance when used in the back of ultra-thin film devices. The main advantage of nanoplasmonic AZO is a result of strong light scattering of Ag nano-island and near-field enhancement of incoming light. For the superstrate device configuration the performance enhancement is offset by introducing metallic recombination sites and also increasing the metallic backward scattering. In general, using nanoplasmonic architects has more effect when they are used in the back of the device to surpass the effect of reflection and parasitic absorption of final devices.

7-2. Recommendations for the future works

In this PhD thesis the first approach was to use FDTD simulation to investigate different incorporation of nanoplasmonic metallic structure for absorption enhancement in nanocrystalline silicon solar cells. In experimental effort, by using NSTS method for large area manufacturing, large area random Ag nano-island was developed. The effect of random nanoplasmonic structure on performance enhancement of developed ultra-thin film device is investigated and discussed.

In this research the effect of the ultra-thin film cells were developed on smooth sample. The effect of textured substrate and comparing of the effect of nanoplasmonic structure on performance will

give a better comparison on effectiveness of nanoplasmonic light trapping with textured substrate which would be good candidate for further study.

The final results from nanoplasmonic simulation in chapter 5 are also providing a good path for further research studies. The following experimental works can be ramified for these results: 1) Investigating experimentally the effect of spacer materials and thickness to show the presence of a maximum spacer thickness in ultra-thin film devices, 2) Showing the performance enhancement of incorporating nanoplasmonic structures are more dominant and has higher impact in thinner absorber layer by comparing the enhancement ratio for different thin film device thickness, and 3) Comparing the effect of spheres and semispheres metallic array on ultra-thin film devices to validate the mechanism involved in performance enhancement and experimentally shows spheres nanoparticles has higher effect in performance enhancement of ultra-thin film solar cells.

In addition, although AZO provided a good performance to incorporate nanoplasmonic metallic structure, but since high conductivity is an essential part of performance for the proposed device, carrier recombination in the TCO layer due to incorporation of metallic nanoplasmonic structures is present. To address this issue use of suitable dielectric layer to isolate the nanoplasmonic structure from conductive layer can be studied as well.

At the end, capability of nanospherical lithography to create cost effective large area array of nanoplasmonic metallic structure can also be investigated to understand the performance enhancement by this technique. One of the advantages of nanospherical method is its capability to use any metallic materials which enabled us create Al, Au, and other nanoplasmonic metallic materials as well.

Letters of Copyright Permission

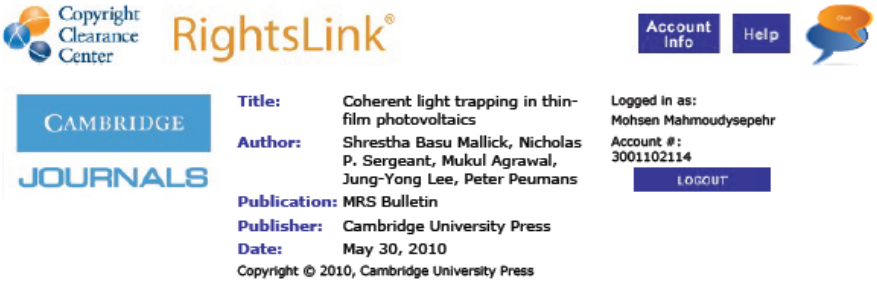

Copyright Clearance Center RightsLink®

Account Info | Help

CAMBRIDGE JOURNALS

Title:	Coherent light trapping in thin-film photovoltaics	Logged in as: Mohsen Mahmoudysepehr
Author:	Shrestha Basu Mallick, Nicholas P. Sergeant, Mukul Agrawal, Jung-Yong Lee, Peter Peumans	Account #: 3001102114
Publication:	MRS Bulletin	LOGOUT
Publisher:	Cambridge University Press	
Date:	May 30, 2010	

Copyright © 2010, Cambridge University Press

Order Completed

Thank you for your order.

This Agreement between Mohsen Mahmoudysepehr ("You") and Cambridge University Press ("Cambridge University Press") consists of your order details and the terms and conditions provided by Cambridge University Press and Copyright Clearance Center.

License number	Reference confirmation email for license number
License date	Jan 17, 2017
Licensed Content Publisher	Cambridge University Press
Licensed Content Publication	MRS Bulletin
Licensed Content Title	Coherent light trapping in thin-film photovoltaics
Licensed Content Author	Shrestha Basu Mallick, Nicholas P. Sergeant, Mukul Agrawal, Jung-Yong Lee, Peter Peumans
Licensed Content Date	May 30, 2010
Licensed Content Volume	36
Licensed Content Issue	6
Start page	453
End page	460
Type of Use	Dissertation/Thesis
Requestor type	Author
Portion	Full article
Author of this Cambridge University Press article	No
Author / editor of the new work	Yes
Order reference number	
Territory for reuse	North America Only
Title of your thesis / dissertation	Enhanced Ultrathin Film Nanocrystalline Silicon Photovoltaic Device Architectures
Expected completion date	Jan 2017
Estimated size(pages)	159
Requestor Location	Mohsen Mahmoudysepehr

	Attn: Mohsen Mahmoudysepehr
Publisher Tax ID	123258667RT0001
Billing Type	Invoice
Billing address	

Attn: Mohsen Mahmoudysepehr

Total 0.00 CAD

CLOSE WINDOW

NATURE PUBLISHING GROUP LICENSE TERMS AND CONDITIONS

Jan 21, 2017

This Agreement between Mohsen Mahmoudysepehr ("You") and Nature Publishing Group ("Nature Publishing Group") consists of your license details and the terms and conditions provided by Nature Publishing Group and Copyright Clearance Center.

License Number	4033661314720
License date	Jan 21, 2017
Licensed Content Publisher	Nature Publishing Group
Licensed Content Publication	Nature Materials
Licensed Content Title	Plasmonics for improved photovoltaic devices
Licensed Content Author	Harry A. Atwater, Albert Polman
Licensed Content Date	Feb 19, 2010
Licensed Content Volume Number	9
Licensed Content Issue Number	3
Type of Use	reuse in a dissertation / thesis
Requestor type	academic/educational
Format	print and electronic
Portion	Full article
Circulation/distribution	<501
Author of this NPG article	no
Your reference number	
Title of your thesis / dissertation	Enhanced Ultrathin Film Nanocrystalline Silicon Photovoltaic Device Architectures
Expected completion date	Jan 2017
Estimated size (number of pages)	159
Requestor Location	Mohsen Mahmoudysepehr 200 University Ave. West ECE Dept. University of Waterloo Waterloo, ON M2L3G1 Canada Attn: Mohsen Mahmoudysepehr
Billing Type	Invoice
Billing Address	Mohsen Mahmoudysepehr ECE Dept. 200 University Ave. West Waterloo, ON M2L3G1 Canada Attn: Mohsen Mahmoudysepehr
Total	0.00 CAD
Terms and Conditions	

Bibliography

[1] A. Goetzberger, and V. U. Hoffmann, Photovoltaic Solar Energy Generation, Springer, 2005.

[2] http://www.advanced-energy.com/en/PV_Sun_Times.html.

[3] K. L. Chopra, and S. R. Das, Thin Film Solar Cells, Plenum Press, New York, 1983.

[4] K. L. Chopra1, P. D. Paulson and V. Dutta, "Thin Film Solar Cells: An Overview", Prog. Photovolt: Res. Appl., Vol. 12, 2004, PP.69–92.

[5] S. Stronh, "Building Integrated Photovoltaics (BIPV)", wbdg.org, Whole Building design Guide, Retrived June 26, 2011.

[6] GBI Research's new report, "Thin - Film Photovoltaic (PV) Cells Market Analysis to 2020 - CIGS (Copper Indium Gallium Diselenide) to Emerge as the Major Technology by 2020", July 2010.

[7] "Opportunities for Canadian Energy Technologies in Global Markets", McKinsey & Co. on behalf of Natural Resource Canada, 2012.

[8] "Trends 2015 in Photovoltaic Applications", International Energy Agency (IEA), 20th edition, 2015.

[9] "Achieving Balance-Ontario's Long-Term Energy Plan", Minister of Energy, 2013, http://www.energy.gov.on.ca/en/ltep/.

[10] P. Luukonen, Y. puissant, and L. Dignard-Bailey, « Photovoltaic Technology Status and Reports-Canadian Annual report 2013", Canadian Solar Industries Association, 2013.

[11] N-Tech Research report, "BIPV Technologies and Markets 2015-2022", N-Tech Research, July 07, 2015.

[12] N-Tech Research report, "BIPV Glass Markets 2015-2022", N-Tech Research, November 24, 2015.

[13] SUNRISE report, "Building Integrated Photovoltaics: An Overview of the Existing Products and Their Fields of Applications", European PV Industry Association (EPIA): Sunrise Project, 2009.

[14] K. Sinapis, M. van den Donker, "BIPV Report 2013", Solar Energy Application Centre, 2013.

[15] C. A. Wolden, J. kurtin, J. B. Baxter, I. Repins, S. E. Shaeheen, J. T. Torvik, A. Rockett, V. M. Fthenakis, and E. S. Aydil, "Photovoltaic Manufacturing: Present Status, Future Propects, and Research Needs", J. Vac. Sci. Technol. A, Vol. 29, 2011, 030801.

[16] E.T. Yu and J. van de Lagemaat, "Photon Management for Photovoltaics", MRS Bulletin, Vol. 36, June 2011, pp. 424-428.

[17] E.Yablanovitch, " Statistical ray optics", J. Opt. Soc. Am., Vol. 72, No. 7, 1982, P.899.

[18] Sh. B. Mallick, N. P. Sergeant, M. Agrawal, J. Y. Lee, and P. Peumans, "Coherent Light Trapping in Thin-Film Photovoltaics", MRS Bulletin, Vol. 36, June 2011, pp. 453-460.

[19] M. I. Stockman, "Nanoplasmonics: Past, Present, and Glimps into Future", Optics Express, Vol. 19, No. 22, 2009, P. 22029-22106.

[20] D. sarid, and W. Challener, Modern Introduction to Surface Plasmons: Theory, Mathematics, and Applications, Cambridge University Press, 2010.

[21] H. A. Atwater, and A. Polman, "Plasmonics for Improved Photovoltaic Devices", Nature Materials, Vol. 9, March 2010, P. 205.

[22] S. Pillai, and M. A. Green, "Plasmonics for Photovoltaic Applications", Solar Energy Materials & Solar Cells, Vol. 94, 2010, pp. 1481-1486.

[23] M. Hiramoto, M. Suezaki, and M. Yokoyama, "Effect of Thin Gold Interstitial on the Photovoltaic Properties of Tandem Organic Cell", Chemistry Letters, 1990, pp. 327-330.

[24] O. Stenzel, A. Stendal, K. Voigtsberger, and C. von Borezyskowski, "Enhancement of the Photovoltaic Conversion Efficiency of Copper Phthalocyanine Thin Film Devices by Incorporation of Metal Clusters", Solar Energy Materials & Solar Cells, Vol. 37, 1995, pp. 337-348.

[25] O. Stenzel, S. Wilbrandt, A. Stendal, U. Beckers, K. Voigtsberger, and C. von Borezyskowski, "The incorporation of metal clusters into tin film organic dye layers as a mthod for producing strongly absorbing composite layers: an ascillator model approach to resonant metal cluster absorption", J. Phys. D: Appl. Phys., Vol. 28, 1995, pp. 2145-2162.

[26] H. R. Stuart, and D. G. Hall, "Enhanced Dipole-Dipole Interaction between Elementary Radiators Near a Surface", Phys. Rev. Lett., Vol. 80, No. 25, 1998, pp. 5663-5666.

[27] H. R. Stuart, and D. G. Hall, "Island Size Effcet in nanoparticle-Enhanced Photodetectors", Appl. Phys. Lett., Vol. 73, No. 26, 1998, pp. 3815-3817.

[28] M. Westphalen, U. Kreiberg J. Rostalski, H. Luth, and D. Meissner, "Metal Cluster Enhanced Organic Solar Cells", Solar Energy Materials & Solar Cells, Vol. 61, 200, pp. 97-105.

[29] B. P. Rand, P. Peumans, and S. R. Forrest, "Long-range absorption enhancement in organic tandem thin-film solar cells containing silver nanoclusters", J. Appl. Phys., Vol. 96, No. 12, 2004, pp. 7519-7526.

[30] D. M. Schaadt, B. Feng, and E. T. Yu, "Enhanced semiconductor optical absorption via surface excitation in metal nanoparticles", Appl. Phys. Lett., Vol. 86, 2005. P. 063106.

[31] D. Derkacs, S. H. Lim, P. Matheu, W. Mar, and E. T. Yu, "Improved performance of amorphous silicon solar cells via scattering from surface plasmon polaritons in nearby metallic nanoparticles", Appl. Phys. Lett., Vol. 89, 2006, P. 093103.

[32] S. Pillai, K. R. Catchpole, T. Trupke, and M. A. Green, "Surface plasmon enhanced silicon solar cells", Appl. Phys. Lett., Vol. 101, 2007, P. 093105.

[33] N. C. Linquist, W. A. Luhman, S. H. Oh, and R. J. Holmes, "Plasmonic nanocavity arrays for enhanced efficiency in organic photovoltaic cells", Appl. Phys. Lett., Vol. 93, 2008, P. 123308.

[34] K. Nakayama, K. Tanabe, and H. A. Atwater, "Plasmonic nanoparticle enhanced light absoption in GaAs solar cells", Appl. Phys. Lett., Vol. 93, P. 121904.

[35] V. E. Ferry, M. A. Verschuuren, H. B. T. Li, R. E. I. Schropp, H. A. Atwater, and A. Polman, "Improved red-response in thin film aSi:H solar cells with soft-imprinted plasmonic back reflectors", Appl. Phys. Lett., Vol. 95, 2009, P. 183503.

[36] S. V. Gaponenko, Introduction to nanophotonics, Cambridge University Press, 2010.

[37] K. R. Catchpole, and A. Polman, "Plasmonic Solar Cells", Optics Express, Vol. 16, No. 26, 2008, PP. 21793-21800.

[38] K. R. Catchpole, and A. Polman, "Design Principle for Particle Plasmon Enhanced Solar Cell", Appl. Phys. Lett., Vol. 93, 2008, P. 191113.

[39] V. E. ferry, J. N. Munday, and H. A. Atwater, "Design Considerations for Plasmonic Photovoltaic", Adv. Mater, Vol. 22, 2010, PP. 4794-4808.

[40] "plasmonic solar cell" Wikipedia: The Free Encyclopedia. Wikimedia Foundation, Inc. 22 July 2004. Web. 10 Dec. 2009.

[41] M. Quinten, Optical Properties of Nanoparticle Systems: Mie and Beyond, Wiley-VCH Verlag GmbH & Co. KGaA, 2011.

[42] C. F. Bohren, and D. R. Huffmann, Absoption and Scattering of Light by Small Particles, Wiley-VCH Verlag GmbH & Co. KGaA, 2007.

[43] K. Tanabe, "Field Enhacement around Metal nanoparticles and Nanoshells: A Systematic Investigation", J. Phys. Chem. C, Vol. 112, 2008, pp. 15721-15728.

[44] A. Taflove and S. C. Hagness, Computational Electrodynamics: The Finite –Difference Time-Domain Method, Artech House Inc., 2005.

[45] R. Santbergen, T. L. Temple, A. H. M. Smets, R. A. C. M. M van Swajj, and M. Zeman, "Application of Plasmonic Silver Island Films in Thin film Silicon Solar Cells", J. Opt., Vol. 14, 2012, P. 024010.

[46] B. Yan, J. Yang, and S. Guha, "Amorphous and Nanocrystalline Silicon thin Film Photovoltaic Technology on Flexible Substrates", J. Vac. Sci. Technol. A, Vol. 30, No. 4, 2012, P. 04D108.

[47] Song D, Aberle A G and Xia J 2002 Appl. Surf. Sci. 195 291.

[48] Müller J, Rech B, Springer J and Vanecek M, 2004 Sol. Energy 77 917.

[49] Singh A V, Mehra R M, Buthrath N, Wakahara A, and Yoshida A, 2001 J. Appl. Phys. 90 11 5661.

[50] Calnan S and Tiwari A N, 2010 Thin Solid Films 518 1839.

[51] Minami T 2005 Semicond. Sci. Technol. 20 S35 .

[52] Kim H, Osofsky M, Prokes S M, Glembocki O J, and Piqué A 2013 Appl. Phys. Lett. 102 17.

[53] Cornelius S, Vinnichenko M, Shevchenko N, Rogozin A, Kolitsch A and W. Möller W 2009 Appl. Phys. Lett. 94 4.

[54] Kumar M, Wen L, Sahu B B, and Han J G 2015 Appl. Phys. Lett. 106 24.

[55] Kuo C L, Wang R C, Huang J L, Liu C P, Wang C K, Chang S P, Chu W H, Wang C H and Tu C H 2009 Nanotechnology 20 365603.

[56] Agashe C, Kluth O, Hüpkes J, Zastrow U, Rech B, and Wuttig M 2004 J. Appl. Phys. 95 4.

[57] Birgin E G, Chambouleyron I and Martínez J M 1999 J. Comput. Phys. 151 2.

[58] Agashe C, Kluth O, Schöpe G, Siekmann H, Hüpkes J and Rech B 2003 Thin Solid Films 442 167.

[59] Maeng W J, Lee J W, Lee J H, Chung K B and Park J S 2011 J. Phys. D: Appl. Phys. 44 445305.

[60] Minami T, Miyata T, Ohtani Y and Mochizuki Y 2006 Jpn J Appl Phys Part 2 Letter 45 12.

[61] Fournier C, Bamiduro O, Mustafa H, Mundle R, Konda R B, Williams F, and Pardhan A K 2008, Semicond. Sci. Technol. 23 085019.

[62] Birgin E G, Chambouleyron I and Martínez J M 1999 *J. Comput. Phys.* **151** 862.

[63] Klug H P and Alexander L E 1974 X-Ray Diffraction Procedures for Polycrystalline and Amorphous Materials,2nd ed. (Wiley Interscience, New York) 992 .

[64] Morkoc H, Ozgur U, *Zinc Oxide: Fundamnetals, materials and device Technology* 2009 (John Wiley-VCH Verlag GmbH & Co., Weinheim, Germany) pp. 1-76.

[65] Minami T 2008 Thin Solid Films 516 17.

[66] Sieber I, Wanderka N, Urban I, Dörfel I, Schierhorn E, Fenske F and Fuhs W 2010 Thin Solid Films 330 2.

[67] Ong H C and Du G T 2004 *J. Cryst. Growth* **265** 471.

[68] Choi Y S, Kang J W, Hwang D K, and Park S J 2010 IEEE Trans. Electron Devices 57 26.

[69] Ahn C H, Kim Y Y, Kim D C, Mohanta S K, and Cho H K 2009 J. Appl. Phys. 105 1.

[70] Djurisic A B, Leung Y H, Tam K H, Hsu Y F, Ding L, Ge W K, Zhong Y C, Wong K S, Chan W K, Tam H L, Cheah K W, Kwok W M and Phillips D L 2007 *Nanotechnology* **18** 095702.

[71] Alvi N H, Hasan K, Nur O and Willander M 2011 Nanoscale Res. Lett. 6 1

[72] Liu W R, Li Y H, Hsieh W F, Hsu C H, Lee W C, Hong M and Kwo J 2008 *J. Phys. D: Appl. Phys.* **41** 065105.

[73] Rahman M M, Khan M K R, Islam M R, M. Halim M A, Shahjahan M, Hakim M A, Saha D K and Khan J U 2012 Journal of Materials Science & Technology 28 329.

[74] E. Fathi, "Thin Film Solar Cells on Transparent Plastic Foils," PhD thesis, University of Waterloo, 2011.

[75] L. Tian, "Development of Advanced Thin Films by PECVD for Photovoltaic Applications", MSc thesis, University of Waterloo, 2013.

[76] R. S. Tarighat, "A Novel Buried-Emitter Photovoltaic Cell for High Efficiency Energy Conversion", PhD thesis, University of Waterloo, 2013.

[77] X. Deng, W. Wang, S. Shan, H. Povolny, W. Du, X. Liao, and X. Xiang, "Impact of wide band-gap p-type nc-Si on the performance of a-Si solar cells", Int. J. Mod. Phys. B, Vol. 16, 2002, pp. 57-63.

[78] W. Du, X.Liao, X. Yang, H. Povolny, X. Xiang, X. Deng, K.a.i.Sun , "Hydrogenated nanocrystalline silicon p-layer in amorphous silicon n-i-p solar cells", Sol. Energy Mater. Sol. Cells, Vol. 90, 2006, pp. 1098–1104.

[79] J. M. Pearce, N. Podraza, R. W. Collins, M. M. Al-Jassim, K. M. Jones, J. Deng, and C. R. Wronski, "Optimization of open circuit voltage in amorphous silicon solar cells with

mixed-phase (amorphous+nanocrystalline) p-type contacts of low nanocrystalline content", J. Appl. Phys., Vol. 101, 2007, PP. 1143011-1143015.

[80] A. Shah, Thin-Film Silicon Solar Cells, EPFL Press, Switzerland, 2010.

[81] S. Klein, T. Repmann, and T. Brammer, "Microcrystalline silicon films and solar cells by PECVD and HWCVD", Solar Energy, Volume 77, Issue 6, 2004, pp. 893-908.

[82] J. Poortmans, V. Arkhipov, Thin Film Solar Cells: Fabrication, Characterization and Applications, John Wiley and Sons Ltd, 2006.

[83] U. K. Das, E. Centurioni, S. Morrison, and A. Madan, "A critical role of p/i interface in nanocrystalline single junction p-i-n solar cells", 3rd World Conference on Photovoltaic Energy Conversion, May 11-18 2003, Osaka, Japan.

[84] J. K. Rath and R. E I. Schropp, "Incorporation of p-type microcrystalline silicon films in amorphous silicon based solar cells in superstrate structure", Solar Energy Materials and Solar Cells, Vol. 53, 1998, pp. 189-2023.

[85] H. Stiebig, F. Siebke, W. Beyer, C. Beneking, B. Rench, and H. Wagner, "Interfaces in aSi:H solar cell structures", Solar Energy Materials and Solar Cells, Vol. 48, 1997, pp. 351-363.

[86] S. Baek, J. C. Lee, Y.J. Lee, S. M. Iftiquar, Y. Kim, J. Park, and J. Yi, "Interface modofocation effect between p-type aSiC:H and ZnO:Al in p-i-n amorphous silicon solar cells, Nanoscale research Letters, 781, 2012.

[87] S. Dongaonkar, J. D. Servaites, G. M. Ford, S. Loser, J. Moore, R. M. Gelfand, H. Mohseni, H. W. Hillhouse, R> Agrawi, M. A. Ratnet, T. J. Marks, M. S. Lundstrom, and M. A. Alam, "Universality of non-ohmic shunt leakage in thin-film solar cells", J. Appl. Phys., Vol. 108, 2010, p. 124509.

[88] Z. Qiao, X. Xie, Q. Hao, D. Wen, J. Xue, and C. Liu, "Investigation of p-type nanocrystalline silicon emitters for silicon heterojunction solar cells", Applied Surface Science, Vol. 324, 2015, pp. 152-159.

[89] H. Stiebig, F. Siebke, W. Beyer, C. Beneking, B. Rench, and H. Wagner, "Interfaces in aSi:H solar cell structures", Solar Energy Materials and Solar Cells, Vol. 48, 1997, pp. 351-363.

[90] M. Kubon, E. Boehmer, F. Siebke, B. Rech, C. Beneking, H. Wagner, "Solution of the ZnO/p contact problem in aSi:H solar cells", Solar Energy Materials and Solar Cells, Vol. 41/42, 1996, pp. 485-492.

[91] V. Vlahos, J. Deng, J. M. Pearce, R. J. Koval, R. W. Collins, and C. R. Wronski, Mater. Res. Soc. Symp. Proc. 762, A7.2 2003.

[92] M. kubon, E. Boehmer, M. Gastel, W. Beyer, C. Beneking, and H. Wagner, "Solution of the ZnO/p contact problem in aSi:H solar cells", IEEE First WCPEC, Dec. 5-6 1994. Hawaii.

[93] T. Soderstrom, F. J. Haug, V. terrazoni-Daudrix, X. Niquille, M. Python, and C. Ballif, « N/i buffer layer for substrate microcrystalline thin film silicon solar cell », J. Appl. Phys., Vol. 104, 2008, p. 104505.

[94] A. Mossad Ali and H. Kobayashi, "Hydrogen effect on nanostructural features of nanocrystalline silicon thin film deposited at 200°C by PECVD", J. Non-Cryst. Solids, ol. 385, 2014, pp. 17-23.

[95] M. Isomura, M. Kondo, and A. Matsuda, "Effects of hydrogen diluted silane plasma on amorphous silicon solar cells", Jpn. J. Appl. Phys., Vol. 39, 2000, pp. 4721-4726.

[96] https://www.lumerical.com/tcad-products/fdtd/

[97] E. D. Palik, Handbook of Optical Constants of Solids I-III, Elsevier, Amsterdam, 1998, p.187.

[98] https://www.lumerical.com/support/whitepaper/fdtd_multicoefficient_material_modeling.html.

[99] http://rredc.nrel.gov/solar/spectra/am1.5/ASTMG173/ASTMG173.html.

[100] Gwamuri, J., Güney, D. Ö. and Pearce, J. M., Advances in Plasmonic Light Trapping in Thin-Film Solar Photovoltaic Devices, in Solar Cell Nanotechnology (eds A. Tiwari, R. Boukherroub and M. Sharon), John Wiley & Sons, Inc., 2013, Hoboken, NJ, USA.

[101] M. Gu, Z. Quyang, B. Jia, N. Stokes, X. Chen, N. Fahim, X. Li, M. J. Ventura, and Z. Shi, "Nanoplasmonics: a frontier of photovoltaic solar cells", Nanophotonics, Vol. 1, issues 3-4, 2012, pp. 235-248.

[102] Y. A. Akimov, W. S. Koh, and K, Ostrikov, " Enhancement of optical absorption in thin-film solar cells through the excitation of higher-order nanoparticle plasmon modes", optics Express, Vol. 17, No. 12, 2009, pp. 10195-10205.

[103] J. R. Krenn, G. Schider, W. Rechberger, B. Lamprecht, A. Leitner, F. R. Aussenegg, J. C. Weeber, "Design of multipolar plasmon excitations in silver nanoparticles", Appl. Phys. Lett., Vol. 77, 2000, p. 3379.

[104] H. R. Stuart and D. G. hall, "Enhanced Dipole-Dipole Interaction between Elementary Radiatord Near a Surface", Phys. Rev. Lett., Vol. 80, No. 25, 1998, pp. 5663-5666.

[105] S. A. Maier, M. L. Brongersma, P. G. Kik, H. A. Atwater, "Observation of near-field coupling in metal nanoparticle chains using far-field polarization spectroscopy", Phys. rev. B. Vol. 65, 2002, pp. 193408.

[106] S. Malynych and G. Chumanov, "Light-Induced Coherent Interaction between Silver Nanoparticles in Two-Dimentional Arrays", J. Am. Chem. Soc., Vol. 125, No. 10, 2003, pp. 2896-2898.

[107] S. Malynych and G. Chumanov, "Narrow Plasmon Mode in 2D Arrays of Silver Nanoparticles Self-Assembled on Thin Silver Film", Journal of Microscopy, Vol. 229, No. 3, 2008, pp. 567-574.

[108] Krenn J R, Gotschy W, Somitsch D, Leitner A and Aussenegg F R 1995 Investigation of localized surface plasmons with the photon scanning tunneling microscope Appl. Phys. A **61** 541–5

[109] M. R. Goncalves, "Plasmonic nanoparticles: fabrication, simulation and experiments », J. Phys. D : Appl. Phys., Vol. 47, 2014, p. 213001.

[110] N. Guillot and M. L. Chapelle, "Lithographied Nanostructures as Nanosensors", J. Nanophoton, Vo. 61, 2012, 064506

[111] W. Y. Park, Y. Kwon, C. Lee, and K. Whang, "Light outcoupling enhancement from top-emitting organic light-emitting diodes made on a nano-sized stochastic texture surface," Opt. Express **22**, 2014, pp. A1687-A1694.

[112] C. F. Guo, T. Sun, F. Cao, Q. Liu, and Z. Ren, "Metallic nanostructures for light trapping in energy-harvesting devices", Light: Science & Applications, Vol. 3, e161, 2014.

[113] S. Morawiec , J. Holovský,M. J. Mendes, et al., "Experimental quantification of useful and parasitic absorption of light in plasmon-enhanced thin silicon films for solar cells application", Scientific Reports, Vol. 6, 2016, p. 22481.

[114] S. K. Cushing, and N. Wu, "Progress and perspectives of plasmon-enhanced solar energy conversion", J. Phys. Chem. Lett., Vol. 7, 2016, pp. 666-675.

[115] Y. Zhang, and M. Gu, "Plasmonic light trapping for wavelength-scale silicon solar absorbers", Front. Optoelectron., Vol. 9, 2016, pp. 277-282.